ABSTRACT

GROSSMANN, CHRIS ALLEN. Complete Spectroscopy of ^{30}P. (Under the direction of Dr. Gary E. Mitchell and Dr. John F. Shriner, Jr.)

Angular distribution measurements of the ^{29}Si(p,γ)^{30}P reaction were used to assign quantum numbers of levels in ^{30}P. This research was performed at the High Resolution Laboratory (HRL) at Triangle Universities Nuclear Laboratory (TUNL). Resonances were measured at five different angles using a High-Purity Germanium detector. The measured angular distributions were compared to calculated angular distribution expressions for different quantum number possibilities. The angular momentum quantum numbers J and parity π were determined by the relative goodness of these fits. By comparing the reduced matrix elements to the empirically recommended upper limits on transition strengths, the isospin quantum number T was also determined for many states.

Remaining ambiguities were removed by comparison of the experimental levels with theoretical shell model calculations and experimental ^{30}Si levels. The work presented here improved the assignments for approximately 65 states.

With a nearly pure and complete level scheme for ^{30}P between the ground state and $E_x = 8015$ keV, the fluctuation properties of the ^{30}P spectrum were examined. The fluctuations were consistent with a result intermediate between the GOE and Poisson distributions. Within one standard deviation, quantitative measurements of the statistical fluctuations were independent of isospin and consistent with previous ^{26}Al results.

COMPLETE SPECTROSCOPY OF ^{30}P

by

CHRIS ALLEN GROSSMANN

A dissertation submitted to the Graduate Faculty of

North Carolina State University

in partial fulfillment of the

the requirements for the Degree of

Doctor of Philosophy

PHYSICS

Raleigh

1999

APPROVED BY:

D. Ronald Tilley

Mohamed Bourham

Gary E. Mitchell,

Co-chair of Advisory Committee

John F. Shriner, Jr.,

Co-chair of Advisory Committee

Biography

Chris Allen Grossmann

Personal

Born November 27, 1970

Waterville, ME

Education

B.S. Physics, Ball State University, 1994

Academic Positions

Teaching Assistant, North Carolina State University, 1994–1996

Research Assistant, North Carolina State University, 1996–1999

Memberships

Sigma Pi Sigma

American Physical Society

Phi Kappa Phi

Golden Key National Honor Society

Contents

List of Tables

List of Figures

Chapter 1

Introduction

The past fifteen years have shown a rebirth of the field of statistical nuclear physics due to an interest in the behavior of chaotic quantum systems. Statistical properties of eigenvalue spectra also provide excellent tests of symmetry breaking. Random Matrix Theory (RMT) is the theory which is used extensively to describe these statistical properties.

Bohigas [Boh84] studied the fluctuations of the quantized energy levels of Sinai's billiard, a classically chaotic system. The fluctuations were consistent with the predictions of the Gaussian Orthogonal Ensemble (GOE) of RMT. Bohigas conjectured that all quantum analogs of time-reversal-invariant classically chaotic systems would have fluctuation properties that obey the GOE statistics of RMT [Boh84]. Other calculations have supported a similar conjecture that quantum analogs of regular systems obey Poisson statistics [Boh88].

Energy levels in the compound nucleus provide an excellent experimental test of the GOE of RMT. Using 1407 neutron and proton resonances in 27 nuclei, statistical analyses of thirty sequences were found to be consistent with the predictions of the GOE [Haq82, Lom94]. Shriner [Shr91] studied the fluctuation properties of low-lying energy levels in sixty nuclei, spanning $A = 25 - 240$. This study found that the lightest nuclei obeyed GOE statistics, while the heaviest nuclei obeyed Poisson statistics. The intermediate masses displayed results between GOE and Poisson. Detailed statistical analyses were desired for a single nucleus including both simple levels near the ground state and complex levels in

the resonance region.

The nuclide ^{26}Al was chosen because its spectroscopy was the most pure and complete available [End86, End88]. Statistical analysis on ~ 100 positive parity states in this nucleus concluded that the fluctuations were intermediate between GOE and Poisson statistics [Shr90]. This analysis is consistent with the conclusion that the fluctuation properties are independent of isospin. Another nucleus in this mass range, ^{30}P, was then chosen for study.

The work presented in this dissertation is part of several experimental studies performed by the High Resolution Laboratory (HRL) group at Triangle Universities Nuclear Laboratory (TUNL) to establish pure and complete spectroscopy for ^{30}P from the ground state through the resonance region. High-resolution elastic scattering measurements were performed in the energy range $E_p = 0.94 - 3.3$ MeV to locate energy levels and to assign J and π values above threshold [Nel83, Fra91]. High-resolution (p,γ) excitation functions were measured in the energy range $E_p = 1.0 - 2.0$ MeV [Vav96] and $E_p = 2.0 - 3.0$ MeV [Fra91], to augment the elastic scattering measurements and the previous capture reaction excitation function and γ-ray decay data [Rei85]. High-resolution γ-ray decay data for ^{29}Si(p,γ) resonances from $E_p = 1.04 - 1.74$ MeV [Vav96] and $E_p = 1.74 - 2.50$ MeV [Wal96] were used to assign quantum numbers for some states and to reduce the range of possible quantum number (J,π,T) assignments.

Angular distribution measurements of transitions to or from levels with remaining ambiguities can assist in further assignments. The required angular distribution calculations were performed, and their effectiveness was demonstrated for two sample resonances [LaB95]. Approximately thirty resonances were selected, measured, and analyzed for this dissertation.

This work reports on angular distribution measurements for more than thirty resonances in the ^{29}Si(p,γ) reaction. Comparisons were also made to shell model calculations and to states in ^{30}Si. Chapter 2 discusses aspects of random matrix theory (RMT), specifically the statistical analyses that are used to examine fluctuation properties of spectra.

Chapter 3 discusses the angular distribution formalism. Emphasis is placed on the ^{29}Si(p,γ) reaction and on the details of extracting the a_2, a_4, and a_6 coefficients. A sample calculation is also presented. Chapter 4 discusses the experimental setup for this measurement. Details concerning the accelerator, detectors, data acquisition electronics, and targetry are presented.

Chapter 5 discusses the methods used to acquire and analyze the data. An outline of all correction factors and analysis codes is included. Mixing ratios and recommended upper limits (RULs) are defined, and an explanation is given of how these upper limits are used to assign quantum numbers. Chapter 6 gives a detailed description of all resonances and bound states for which quantum numbers were assigned in this work. Finally, Chapter 7 discusses the details of the statistical analyses applied to these data.

Several appendices are included to supplement this dissertation. Appendix A lists the expressions for a_2 and a_4 for many different transition types, expressed in terms of mixing ratios. Appendix B lists all of the a_2 and a_4 coefficients measured in this work. Appendix C lists all of the mixing ratios measured in this work. Appendix D compares the experimentally measured levels in ^{30}P to shell model calculations for ^{30}P and to ^{30}Si parent states.

Chapter 2

Statistical Analyses

The goal of this work is to obtain a pure and complete ^{30}P level scheme and to perform statistical analyses on this spectrum. The appropriate theory for these analyses is random matrix theory. Relevant concepts of random matrix theory are briefly summarized here: detailed discussions on the historical background and the formalism of random matrix theory is given in a comprehensive review by Guhr *et al.* [Guh98] and by Mehta [Meh91].

Random matrix theory introduces an ensemble of random Hamiltonian matrices $\mathcal{H}$. The matrices are real symmetric, based on the physical contraints of time reversal and rotational symmetry inherent in nuclei. These conditions describe the Gaussian Orthogonal Ensemble (GOE). Each matrix $\mathcal{H}$ is assumed to describe equally probable interactions between particles. Statistical properties of nuclear spectra are obtained by examining fluctuations about averages of certain quantities. It should be noted that the GOE does not take into account dynamical properties of the nuclear Hamiltonian. Thus, the GOE makes parameter-free predictions of the fluctuation properties of a nuclear system but says nothing about average properties.

2.1 Eigenvalues

2.1.1 Nearest Neighbor Spacing Distribution

One statistic used in the investigation of fluctuation properties of a nuclear system is the nearest neighbor spacing distribution (NNSD) for a sequence of levels. A sequence is defined as a set of levels all having the same quantum numbers (in this work, J, π, and T). The NNSD reveals the short range order of a system. The function $P(x)$ is defined as the probability density for two adjacent levels having the spacing s [Guh98]. Fluctuations are usually expressed in terms of the dimensionless variable x, the ratio of the spacing between adjacent levels (s) and the average spacing between levels (D):

$$x = \frac{s}{D}. \tag{2.1}$$

A random set of uncorrelated energy levels with no special symmetries is described by a $P(x)$ which obeys Poisson statistics. Such a distribution depends on x as

$$P_p(x) = e^{-x}. \tag{2.2}$$

These systems allow degeneracies. This is shown in the $x = 0$ behavior of the Poisson distribution: as x approaches zero, $P_p(x)$ reaches a maximum value. The most probable x-value is zero, and thus the most probable spacing between adjacent energy levels is also zero.

A system that follows GOE statistics has an $P(x)$ which is essentially a Wigner Distribution [Guh98]

$$P_g(x) = \frac{\pi}{2} x e^{\frac{-\pi x^2}{4}}. \tag{2.3}$$

This distribution manifests a key prediction of the GOE: levels within a sequence repel each other. This "level repulsion" can be seen in the $x = 0$ behavior of this distribution: $P_g(x)$ approaches zero as x approaches zero. Therefore, a system that follows GOE statistics forbids degeneracies within a sequence.

In practice, experimental data are often more easily compared to one of these distributions by examining the integral of $P(x)$ instead of $P(x)$. The integral of $P(x)$, $F(x)$, is the definite integral over some intermediate variable x' from zero to x,

$$F(x) = \int_0^x P(x')dx' \tag{2.4}$$

Applying this integral to Equations 2.2 and 2.3 gives $F_p(x)$ and $F_g(x)$,

$$F_p(x) = 1 - e^{-x} \tag{2.5}$$

$$F_g(x) = 1 - e^{\frac{-\pi x^2}{4}} \tag{2.6}$$

Figure 2.1 shows the two different types (Poisson and Wigner) of each of these distributions ($P(x)$ and $F(x)$).

2.1.2 Dyson-Mehta Δ_3 Statistic

While the NNSD provides information on the short-range order in spectra, the Dyson-Mehta Δ_3 statistic gives information about the long-range order. The Dyson-Mehta statistic Δ_3 [Dys63] for a sequence of levels between E_{min} and E_{max} is

$$\Delta_3 = \min_{A,B} \left(\frac{1}{E_{max} - E_{min}} \int_{E_{min}}^{E_{max}} d\mathcal{E} \left[N(\mathcal{E}) - A\mathcal{E} - B \right]^2 \right), \tag{2.7}$$

where the linear parameters A and B are varied to minimize the value of the integral. The number of levels with energies less than or equal to $\mathcal{E}$, $N(\mathcal{E})$, is the integral of the level density ρ.

$$N(\mathcal{E}) = \int_0^{\mathcal{E}} \rho(E)dE. \tag{2.8}$$

For Poisson statistics, the expected value of Δ_3 depends on L, the number of average spacings in the interval $[E_{min}, E_{max}]$:

$$\Delta_{3_p}(L) = \frac{L}{15}. \tag{2.9}$$

For GOE statistics, the expected value of $\Delta_3(L)$ must be evaluated numerically. For large values of L it approaches the value

$$\Delta_{3_g}(L) \approx \frac{1}{\pi^2} \left(\ln L - 0.0687 \right). \tag{2.10}$$

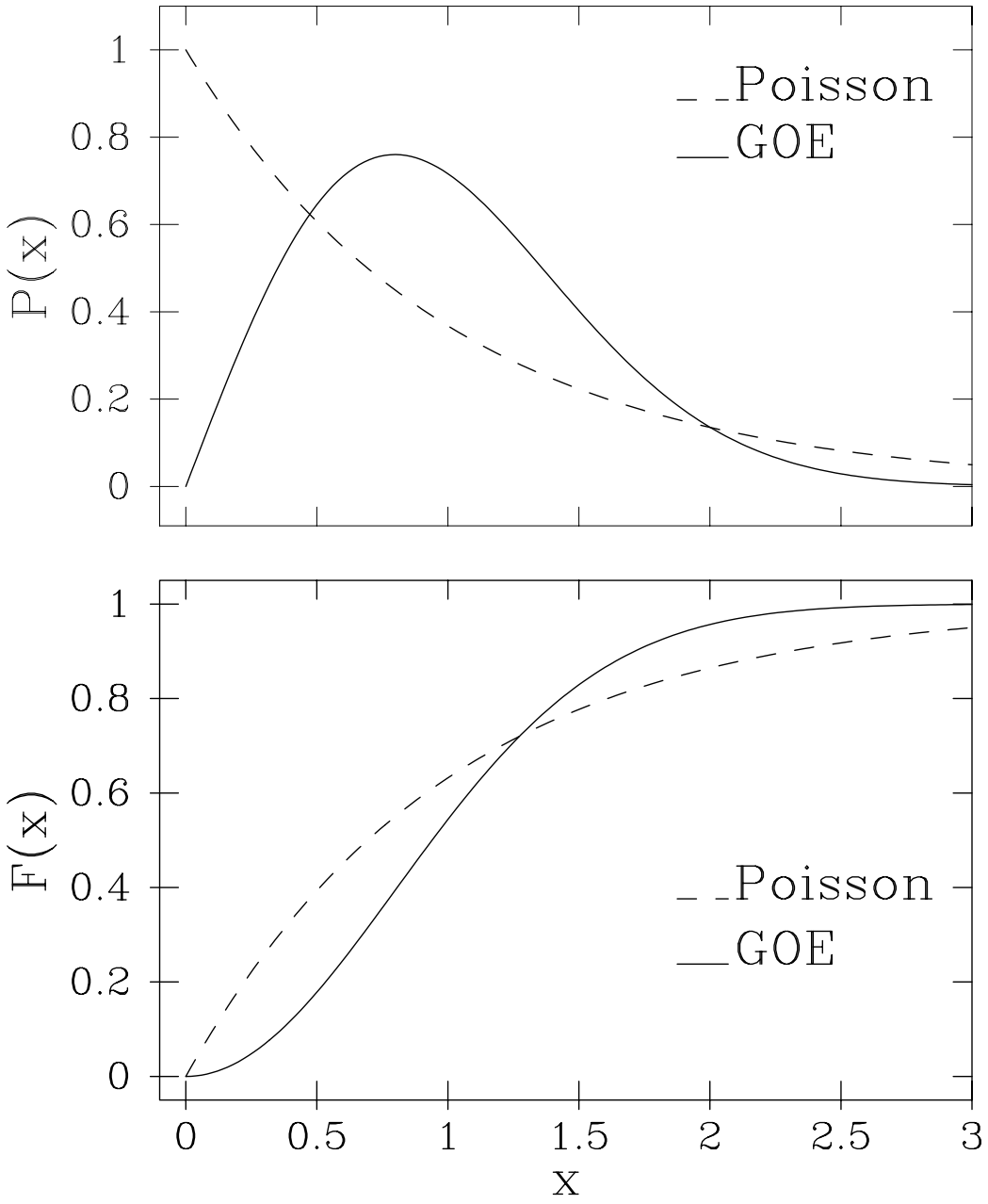

Figure 2.1: Nearest Neighbor Spacing Distributions. In the top figure, the probability density function $P(x)$ is plotted as a function of the dimensionless parameter x, the ratio of a given spacing to the average spacing. In the bottom figure $F(x)$, the integral of $P(x)$, is plotted as a function of x. Each plot shows the theoretical prediction for systems obeying Poisson and GOE statistics.

The expected values of the Dyson-Mehta statistic $\Delta_3(L)$ are shown in Figure 2.2 for both types of statistics.

2.1.3 Comparison to Experiment

To compare experimental data to any of these distributions, the energy levels must first be divided into sequences. Within each sequence, the average level spacing $D(E)$ is not constant but instead decreases with increasing energy. The sequences must therefore be "unfolded" by mapping the set of levels onto a new set of levels which has a constant average spacing D'. This method [Shr91] is summarized below.

Knowing the average level spacing D is equivalent to knowing the level density:

$$\rho(E) = \frac{1}{D(E)}. \tag{2.11}$$

To correct the sequence, a level density of

$$\rho(E) = \frac{1}{T} e^{\frac{E-E_0}{T}} \tag{2.12}$$

is assumed. For fitting purposes, it is more convenient to use $N(E)$, the integral of $\rho(E)$, than $\rho(E)$ directly. The energy levels E of the sequence are fit to

$$N(E) = \int_0^E \rho(\mathcal{E})\, \mathrm{d}\mathcal{E} = e^{\frac{E-E_0}{T}} - e^{\frac{-E_0}{T}} + N_0, \tag{2.13}$$

where E_0, T, and N_0 are constants. A best fit to Equation 2.12 (the best-fit function is denoted by $F(E)$) allows a "corrected" set of energies E_i' to be generated

$$E_i' = E_{min} + \frac{F(E_i) - F(E_{min})}{F(E_{max}) - F(E_{min})} (E_{max} - E_{min}). \tag{2.14}$$

The corrected spacings s' are now given by the difference between two consecutive energy levels

$$s_i' = E_{i+1}' - E_i', \tag{2.15}$$

and the average spacing D' is the average of the s' values. The dimensionless variable x is expressed as the ratio of the spacing between adjacent energy levels s' and the average

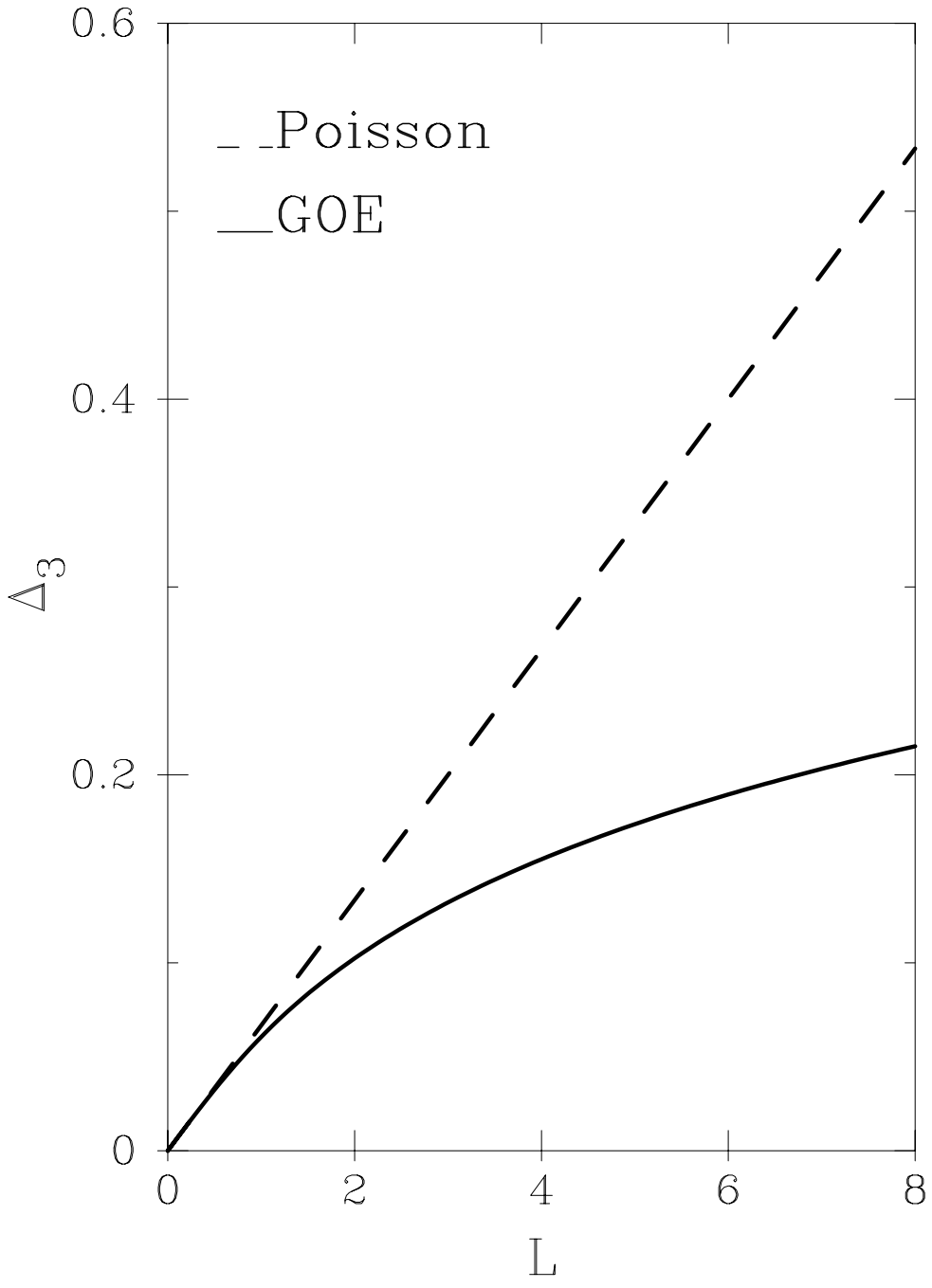

Figure 2.2: The Dyson-Mehta Δ_3 Statistic. Δ_3 is plotted as a function of L, the number of average spacings. Theoretical predictions for this statistic are given for systems with Poisson and GOE statistics.

spacing D':

$$x_i = \frac{s_i'}{D'}. \tag{2.16}$$

Histograms are created from the set of x's to compare to $P(x)$: the set of ordered x's can be compared to $F(x)$.

In practice, single sequences in nuclei usually have too few members to draw reliable conclusions about the nature of the spacing distribution. It is therefore necessary to analyze multiple sequences. For the NNSD, spacings are combined after analyzing sequences seperately. For the Dyson-Mehta statistic Δ_3, the Δ_3 value is the weighted average of the Δ_3 value for each of the individual sequences [Shr91].

Experimental results may not agree with either Poisson or GOE predictions. It is useful to define a parameter which interpolates between the two distributions. For the NNSD, an empirical interpolation formula has been proposed [Bro81] for $P(x)$:

$$P(x,\omega) = \alpha\,(\omega+1)\,x^{\omega} e^{-\alpha x^{\omega+1}}, \tag{2.17}$$

where

$$\alpha = \left[\Gamma\left(\frac{\omega+2}{\omega+1}\right)\right]^{\omega+1}. \tag{2.18}$$

When $\omega = 0$, Equation 2.17 is exactly Equation 2.2, and when $\omega = 1$, Equation 2.17 is exactly Equation 2.3. This same parameter can be used for $F(x)$, by integrating Equation 2.17. It should be noted that this interpolation is purely empirical.

For the Dyson-Mehta Δ_3 statistic, the interpolation formula [Sel85] analogous to the interpolation formula given in Equation 2.17 is given by

$$\Delta_3\,(L;\mu) = \Delta_{3_g}\,(\mu L) + \Delta_{3_p}\,([1-\mu]\,L)\,. \tag{2.19}$$

The parameter μ is analogous to the parameter ω, with $\mu = 1$ corresponding to GOE behavior and $\mu = 0$ corresponding to Poisson behavior.

2.2 Transitions

The behavior of transitions between eigenstates is also important to study. The GOE predicts that quantum analogs of classically chaotic systems have reduced transition probability distributions which follow the chi-squared distribution function with $\nu = 1$. However, numerical studies show analogs of regular systems follow the chi-squared distribution function with $\nu < 1$ [Alh92, Mer93].

In the GOE, the transition amplitudes T_{if} are assumed to be independent gaussian-distributed variables. Defined in terms of the reduced transition probabilities B, the transition amplitudes are

$$T_{if} = \left\langle \psi_f \left| \left| \hat{T} \right| \right| \psi_i \right\rangle \propto \sqrt{B}, \tag{2.20}$$

where $\hat{T}$ is a transition operator and ψ_i and ψ_f are eigenfunctions of the Hamiltonian $\hat{H}$ [Bro81]. The reduced transition probabilities are normalized to a local average over energy, defining the dimensionless parameter y:

$$y = \frac{B}{\langle B \rangle}. \tag{2.21}$$

These normalized transition probabilities y are distributed according to the Porter-Thomas function [Por56]:

$$P(y) = \frac{1}{\Gamma\left(\frac{1}{2}\right)\sqrt{2y}} e^{-\frac{y}{2}}. \tag{2.22}$$

Numerical studies suggest that many systems which do not follow the GOE have reduced transition probability distributions which deviate from the Porter-Thomas function to the χ-squared distribution function with ν degrees of freedom [Alh92, Mer93]:

$$P(y,\nu) = \chi^2(y,\nu) = \frac{1}{\Gamma\left(\frac{\nu}{2}\right)} \left(\frac{\nu}{2}\right)^{\frac{\nu}{2}} y^{\frac{\nu}{2}-1} e^{-\frac{\nu y}{2}}, \tag{2.23}$$

which reduces to the Porter-Thomas function (Equation 2.22) when $\nu = 1$. Since transition strengths span many orders of magnitude, it is convenient to express this function in terms of z, defined as

$$z = \log_{10}(y). \tag{2.24}$$

After this transformation, Equation 2.23 is renormalized. Figure 2.3 shows a plot of the χ-squared distribution function (Equation 2.23) for different values of ν.

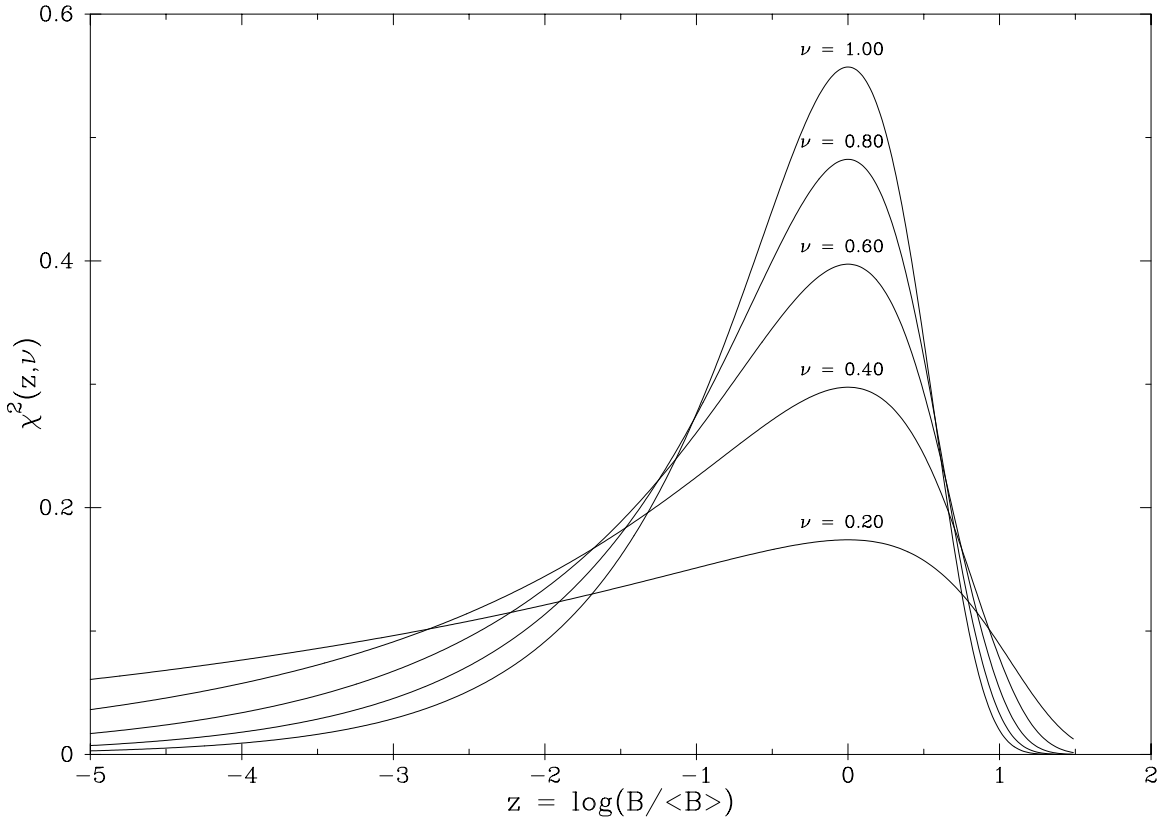

Figure 2.3: χ-Squared Distribution Function. The function is plotted for different ν degrees of freedom.

Chapter 3

Angular Distribution Formalism

Theoretical angular distributions are required to extract information from the measurements performed in this work. Expressions are obtained which express the angular distribution as functions of "mixing ratios" of transition amplitudes. This approach is demonstrated in general in Section 3.1, applied to the ^{29}Si(p,γ) reaction in Section 3.2, and applied to a specific transition in Section 3.3.

3.1 General Treatment

Ferguson [Fer65] describes a technique which utilizes a mixed state expressed as a weighted mixture of pure states. Previously, the mathematically complex techniques of pure initial and final states [Fan53] led to tedious summations over unknown quantum numbers. The newer method is mathematically simpler and is used in this work. This method is described below.

The density matrix, ρ, is defined and written in terms of pure states and their probabilities. An efficiency matrix, ϵ, includes detection information for the exit channel, so that the probability of detecting an event is given by

$$W = \langle \epsilon \rangle = \mathrm{Tr}\,(\rho\epsilon)\,. \tag{3.1}$$

Deriving an angular correlation formula is therefore reduced to determining the appropriate

matrices ρ and ϵ. Shriner [Shr83] gives an extensive description of this method: only the results will be given here.

The angular distribution of the cross section depends on the type of reaction. Reactions of the form X(p, γ)Y are studied in this work. When treated as a compound nuclear reaction, proton capture reactions can be divided into an entrance and an exit channel which are independent of each other, except for conserving certain symmetries. In the entrance channel, a projectile strikes a target, forming a compound state. The target spin A and projectile spin i couple to the channel spin s. The channel spin is coupled with the relative orbital angular momentum ℓ of the target and projectile to form the compound state total angular momentum J. These spin couplings are given by

$$\vec{A} + \vec{i} = \vec{s} \tag{3.2}$$

and

$$\vec{s} + \vec{\ell} = \vec{J}. \tag{3.3}$$

Parity conservation in the entrance channel requires that

$$\pi_J = \pi_A \pi_i \left(-1\right)^{\ell}. \tag{3.4}$$

A primary transition is defined to be a γ-ray transition which decays from the compound state (excited by the capture of a proton) to a residual state. In the exit channel, the residual state angular momentum C and the γ-ray multipolarity L couple to the compound state angular momentum J, given by

$$\vec{C} + \vec{L} = \vec{J}. \tag{3.5}$$

The general expression for the angular distribution is given by Ferguson [Fer65] and is rewritten as

$$\frac{d\sigma}{d\Omega} \propto \left(\frac{\lambda}{i\vec{A}}\right)^2 \sum \left(-1\right)^{(s-\ell_1+\ell_2-2J_2+C-L_1+L_2)} \bar{Z}\left(\ell_1 J_1 \ell_2 J_2; sk\right) \bar{Z}_1\left(L_1 J_1 L_2 J_2; Ck\right) \tag{3.6}$$

$$\langle J_1||\ell_1|s\rangle \langle J_2||\ell_2|s\rangle^* \langle C|QL_1||J_1\rangle \langle C|QL_2||J_2\rangle^*$$
$$Q_k P_k (\cos\theta),$$

with the summation over ℓ_1, ℓ_2, L_1, L_2, J_1, J_2, s, and k. A quantity $\sqrt{2s+1}$ is denoted by $\hat{s}$. The $\bar{Z}$-coefficient is given by Huby [Hub54] as a modification to the Z-coefficient given by Blatt and Biedenharn [Bla52]. The $\bar{Z}_1$-coefficient is discussed by Biedenharn [Bie60]. Q_k is the detector correction factor [Fer65] present because of the finite size of the detector, θ is the angle between the beam and the detector, and P_k is the Legendre polynomial of order k, with k required to satisfy the relations:

$$\vec{k} = \vec{\ell_1} + \vec{\ell_2}, \tag{3.7}$$

$$\vec{k} = \vec{L}_1 + \vec{L}_2, \tag{3.8}$$

and

$$\vec{k} = \vec{J_1} + \vec{J_2}. \tag{3.9}$$

The notation used for the reduced matrix elements [Gol60] distinguishes between emission and absorption matrix elements. The final spins are written on the left hand side of the matrix element and the initial spins on the right. The initial and final spins are separated by a double vertical bar.

Biedenharn [Bie60] has shown that if only a single level contributes to the cross section at a given energy, then the scattering matrix element can be expressed as

$$\langle J||\ell|s\rangle \langle C||L|J\rangle \approx \frac{e^{i\xi_\ell} g_{s\ell} g_L}{E_r - E - \frac{i\Gamma}{2}}. \tag{3.10}$$

Here g is the square root of the partial width of the resonance in the indicated channel, E_r is the resonance energy, Γ is the total width of the resonance, and ξ_ℓ is an energy dependent phase shift. The phase shift includes both Coulomb scattering and hard sphere scattering and depends on kinematic parameters. In this work, the phase shift was calculated numerically for each resonance. This general expression (Equation 3.6) is applicable for all primary transitions resulting from proton capture reactions.

3.2 Application to the ^{29}Si(p,γ) Reaction

For the reaction studied in this work, the projectile is a proton ($i = \frac{1}{2}$) and the target is a ^{29}Si nucleus ($A = \frac{1}{2}$). The compound and residual states (J and C) are states of ^{30}P. The coupling for this reaction is shown in Figure 3.1.

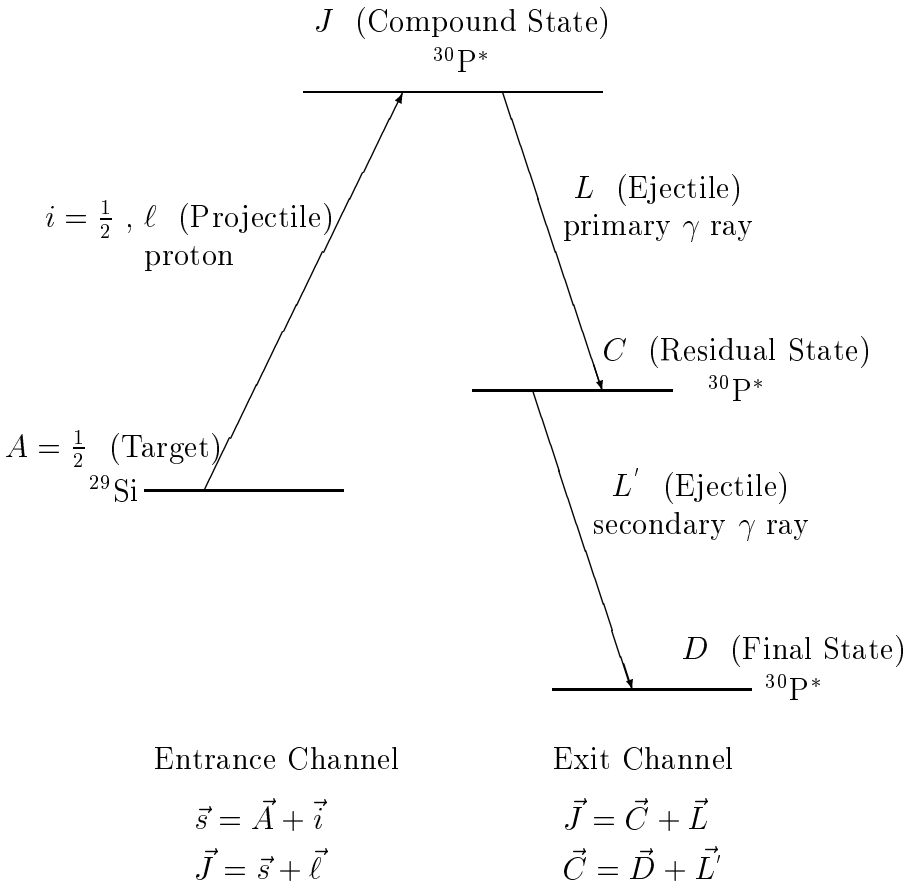

Figure 3.1: Angular Momentum Coupling Scheme. The coupling scheme is shown for the ^{29}Si(p,γ) reaction in the channel spin representation. A proton (projectile) with intrinsic spin i and orbital angular momentum ℓ couples with a ^{29}Si nucleus (target) of spin A to form an excited state of ^{30}P (compound state) with spin J in the entrance channel. In the exit channel, the excited state of ^{30}P (compound state) with spin J decays to another (possibly) excited state of ^{30}P (residual state) with spin C by γ-ray emission, carrying L units of angular momentum. This residual state decays to another (possibly) excited state of ^{30}P (final state) with spin D by a γ-ray, carrying $L^{'}$ units of angular momentum.

The resonances studied in this work are generally well-isolated, and therefore

$$J_1 = J_2 \equiv J. \tag{3.11}$$

The combination of A and i ($\frac{1}{2}$ for both) allows possible values of 0 and 1 for s (Equation 3.2). With only integral values allowed for both s and ℓ, J must also be an integer (Equation 3.3).

The parities of the proton and the target are the same, leading to the further requirement that ℓ has the same parity as the compound state (in the sense that $(-1)^{\ell} = \pi_J$). If there is any ℓ mixing, the two values of ℓ must have the same parity. This ensures that the difference between ℓ_1 and ℓ_2 in Equation 3.6 must be zero or an even integer.

In the exit channel, J and C may have the same or different parities. When the parities are the same, the parity of the radiation must be even. Likewise, when the parities are different, the parity of the radiation must be odd. The parity of the radiation is

$$\pi(ML) = (-1)^{L+1} \tag{3.12}$$

or

$$\pi(EL) = (-1)^{L}. \tag{3.13}$$

For this work, only the E1, E2, E3, M1, and M2 multipoles are considered. Higher multipoles are omitted due to their low emission probabilities. Additionally, mixing of at most two multipoles will be considered.

It is safe to assume that at these energies incident protons will not carry more than four units of angular momentum, since their penetrabilities are then too small to interact with the target nucleus. This limits J values to no more than five units of angular momentum. For any specific transition, choosing J and C will limit further ℓ and L. Additionally, because of the Clebsch-Gordon coefficient (contained in the $\bar{Z}(\ell_1 J \ell_2 J; sk)$ term), and the fact that parity is conserved, k will always be even. The Q_k terms are calculated using Monte Carlo methods. The EGS4 (Electron Gamma Shower version 4) package is used to model the reaction [Nel85]. The use of this package allows inclusion of

the detector material, detector geometry, and γ-ray energy. Equation 3.6 can be rewritten as four terms with three factors each by grouping together common constants:

$$\frac{d\sigma}{d\Omega} = \sum_{k=0,2,4,6} A_k Q_k P_k \left(\cos\theta\right). \tag{3.14}$$

By defining a_k as the ratio of A_k and A_0 the normalization factor A_0 can be factored from this expression. By definition, Q_0 and P_0 are 1. With these substitutions the expression is simpler still:

$$\frac{d\sigma}{d\Omega} = A_0 \left[1 + \sum_{k=2,4,6} a_k Q_k P_k \left(\cos\theta\right)\right]. \tag{3.15}$$

The $P_k\left(\cos\theta\right)$ are well known functions with the angle θ as their argument. The finite geometry correction factors Q_k are determined for each transition. A_0 is an overall normalization factor.

The only remaining variables (which can not be determined from kinematics) from the scattering matrix elements (Equation 3.10) are the g, the square root of the partial width of the resonance in the given channel. Forming the a_k's creates ratios of different g's. Mixing ratios are defined as the square root of the ratio of resonance partial widths in two channels. In this work, the proton mixing ratio only mixes entrance channels s or ℓ, but not both simultaneously, and is usually defined such that the lower value of s or ℓ is in the denominator of the mixing ratio. For example, mixing of $\{s = 1, \ell = 3\}$ and $\{s = 1, \ell = 1\}$ widths is defined as

$$\delta_p \equiv \frac{g_{13}}{g_{11}}. \tag{3.16}$$

Similarly, γ-ray mixing ratios mix multipolarities and are defined such that the lower value of L is in the denominator, consistent with the phase convention of Rose and Brink [Ros67]. In this work, γ-ray mixing will only occur between two γ-ray channels which differ in values of L by one and which have different electromagnetic character. Therefore, mixing will always be between the terms M(L) and E($L+1$). The γ-ray mixing ratio is therefore defined as

$$\delta_\gamma \equiv \frac{g_{E(L+1)}}{g_{M(L)}}. \tag{3.17}$$

Multipolarities higher than E3 will not be considered: this means L will always be ≤ 3, and therefore k will always be ≤ 6. By selecting a specific case (specific J and C values), expressions for a_2, a_4, and a_6 can be evaluated in terms of mixing ratios.

3.3 Example: Resonance with $J^\pi = 2^+$ Decaying to a $J^\pi = 1^+$ State

For clarity and completeness, this calculation will be carried through once in detail for a specific example. The example chosen represents the transition from a compound state of $J = 2$ and $\pi_J = +$ to a residual state of $C = 1$ and $\pi_C = +$. It was shown previously that J and ℓ must have the same parity. Therefore, since J has even parity, ℓ must be even. Substitution of the values of s and J into Equation 3.3 yields

$$\left(\vec{0}, \vec{1}\right) + \vec{\ell} = \vec{2}. \tag{3.18}$$

Both s values allow only an ℓ value of 2. Substitution of the values of C and J into Equation 3.5 yields

$$\vec{1} + \vec{L} = \vec{2}. \tag{3.19}$$

The L value is now restrained to range from 1 to 3. The parity of J and C are the same: this means that QL can be $M1$ or $E2$ (recall Equations 3.12 and 3.13, and that only the two lowest multipolarities are retained). The relationship in Equation 3.8 determines a maximum k value of 4 when there is a maximum L value of 2.

To simplify the expression, the matrix elements appearing in Equation 3.6 will be rewritten as:

$$\langle QL|S|sl\rangle = \langle J||\ell|s\rangle \langle C||QL|J\rangle \tag{3.20}$$

The summation in Equation 3.6 is now over $\ell_1 = 2$, $\ell_2 = 2$, $L_1 = (1, 2)$, $L_2 = (1, 2)$, $s = (0, 1)$, and $k = (0, 2, 4)$. By calculating $\bar{Z}$ and $\bar{Z}_1$ coefficients and performing the sum, the following expression is obtained:

$$\frac{d\sigma}{d\Omega} = Q_0 P_0 (\cos\theta) \left[|\langle M1|S|02\rangle|^2 + |\langle E2|S|02\rangle|^2 \right. \tag{3.21}$$

$$
\begin{aligned}
& + |\langle M1|S|12\rangle|^2 + |\langle E2|S|12\rangle|^2\Big] \\
+Q_2P_2(\cos\theta) \quad & \Big[-\frac{1}{2}|\langle M1|S|02\rangle|^2 + \frac{5}{14}|\langle E2|S|02\rangle|^2 \\
& -\frac{1}{2}\langle M1|S|02\rangle\langle E2|S|02\rangle^* - \frac{1}{2}\langle E2|S|02\rangle\langle M1|S|02\rangle^* \\
& -\frac{1}{4}|\langle M1|S|12\rangle|^2 + \frac{5}{28}|\langle E2|S|12\rangle|^2 \\
& -\frac{1}{4}\langle M1|S|12\rangle\langle E2|S|12\rangle^* - \frac{1}{4}\langle E2|S|12\rangle\langle M1|S|12\rangle^*\Big] \\
+Q_4P_4(\cos\theta) \quad & \Big[+\frac{8}{7}|\langle E2|S|02\rangle|^2 - \frac{16}{21}|\langle E2|S|12\rangle|^2\Big].
\end{aligned}
$$

For these (s,ℓ) and QL combinations, the relevant mixing ratios are defined by

$$\delta_p \equiv \frac{g_{12}}{g_{02}} \tag{3.22}$$

and

$$\delta_\gamma \equiv \frac{g_{E2}}{g_{M1}}. \tag{3.23}$$

Equation 3.21 is simplified by evaluating the matrix elements, extracting the a_2 and a_4 coefficients (as described in Equation 3.15), and formulating the expressions in terms of the mixing ratios. In this case, the phase shifts ξ_ℓ cancel each other when a_2 and a_4 are formed. These coefficients for this transition are

$$a_2 = -\frac{1}{28}\frac{\left(2+\delta_p^2\right)\left(7+14\sqrt{5}\delta_\gamma - 5\delta_\gamma^2\right)}{\left(1+\delta_\gamma^2\right)\left(1+\delta_p^2\right)} \tag{3.24}$$

and

$$a_4 = -\frac{8}{21}\frac{\left(-3+2\delta_p^2\right)\delta_\gamma^2}{\left(1+\delta_\gamma^2\right)\left(1+\delta_p^2\right)}. \tag{3.25}$$

These expressions depend only on the mixing ratios.

3.4 Secondary Transitions

Secondary transitions (γ-ray transitions originating from a state populated by a primary transition and decaying to a final state) are treated in a similar way to primary

transitions. The method will be summarized here. For secondary transitions the residual state C emits a secondary γ-ray of multipolarity $L^{'}$ leaving a final state D. In the exit channel, these are coupled together as:

$$\vec{C} = \vec{D} + \vec{L}^{'}. \tag{3.26}$$

Similar to Equation 3.6, the general expression for the angular distribution of the secondary transitions is given in [Fer65]. For an isolated resonance and for definite values of J, C, and D,

$$\begin{aligned} \frac{d\sigma}{d\Omega} \propto \quad & \sum \lambda\!\!\!^{-2} \frac{\hat{J}^2}{\hat{A}^2 \hat{i}^2} (-1)^{\left(s-\ell_1+\ell_2-2J-2C+D-L_1^{'}+L_2^{'}+L+k\right)} \\ & \bar{Z}\left(\ell_1 J \ell_2 J; sk\right) \bar{Z}_1 \left(L_1^{'} C L_2^{'} C; Dk\right) W\left(JCJC; Lk\right) \\ & \langle J_1 || \ell_1 | s \rangle \langle J_2 || \ell_2 | s \rangle^* \langle C || Q L_1 | J_1 \rangle \langle C || Q L_2 | J_2 \rangle^* \\ & \langle C || Q L_1^{'} | D \rangle \langle C || Q L_2^{'} | D \rangle^* Q_k P_k \left(\cos\theta\right), \end{aligned} \tag{3.27}$$

$$\tag{3.28}$$

where the matrix elements are evaluated using Equation 3.10 and

$$\langle C || Q L^{'} | D \rangle^* \propto g_{L^{'}}. \tag{3.29}$$

The Racah coefficients $W(abcd;ef)$ are well known and are calculated easily [Fer65]. Evaluating the matrix elements gives an expression similar to Equation 3.14. The coefficients a_k are extracted as functions of the mixing ratios. In addition to the proton mixing ratio δ_p and primary γ-ray mixing ratio δ_γ, these a_k depend on the secondary γ-ray mixing ratio $\delta_{\gamma^{'}}$ (defined in a convention consistent with Equation 3.17).

An example will be given, for the transition from a compound state of $J = 2$ and $\pi_J = +$ to a residual state of $C = 2$ and $\pi_C = +$, to a final state of $D = 1$ and $\pi_D = +$. Since J has even parity, ℓ must be even. According to Equation 3.3, both s values (0,1) allow only an even ℓ value of 2. These C and J values allow possible L values between 1 and 4 (Equation 3.5), and with $\pi_C = \pi_J$, only QL values of $M1$ or $E2$ are retained (Equations 3.12 and 3.13). These C and D values allow $L^{'}$ values between 1 and 3 (Equation 3.26), and

with $\pi_D = \pi_C$, only QL' values of $M1$ or $E2$ are retained. For these (s,ℓ), QL, and QL' combinations, the relevant mixing ratios are defined by

$$\delta_p \equiv \frac{g_{12}}{g_{02}}, \tag{3.30}$$

$$\delta_\gamma \equiv \frac{g_{E2}}{g_{M1}}, \tag{3.31}$$

and

$$\delta_{\gamma'} \equiv \frac{g_{E2}}{g_{M1}}. \tag{3.32}$$

The extracted a_k written in terms of the mixing ratios for this transition are

$$a_2 = -\frac{1}{392}\frac{\left(2+\delta_p^2\right)\left(7-3\delta_\gamma^2\right)\left(7+14\sqrt{5}\delta_{\gamma'}-5\delta_{\gamma'}^2\right)}{\left(1+\delta_p^2\right)\left(1+\delta_\gamma^2\right)\left(1+\delta_{\gamma'}^2\right)} \tag{3.33}$$

and

$$a_4 = -\frac{16}{441}\frac{\left(3-2\delta_p^2\right)\left(7-3\delta_\gamma^2\right)\delta_{\gamma'}^2}{\left(1+\delta_p^2\right)\left(1+\delta_\gamma^2\right)\left(1+\delta_{\gamma'}^2\right)}. \tag{3.34}$$

Chapter 4

Experimental Setup

Experimental systems with excellent beam energy resolution are used at the High Resolution Laboratory (HRL) at TUNL in order to perform very precise nuclear structure measurements. Two movable high-purity germanium detectors record the reaction γ-rays. The high resolution system and its relation to this experiment will be discussed in Section 4.1. This system is illustrated schematically in Figure 4.1.

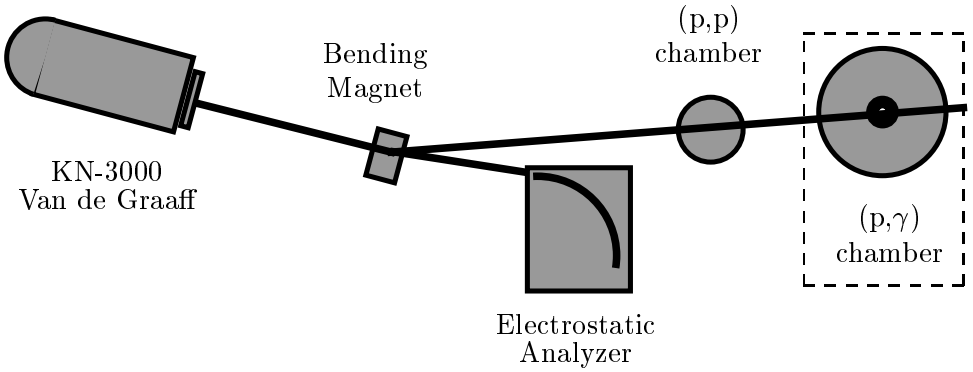

Figure 4.1: The High-Resolution Laboratory at TUNL. The KN-3000 produces and accelerates two beams: protons and singly ionized molecular hydrogen. They are separated at the bending magnet. Protons are bent more to the left and are used for experiments in one of two chambers. The molecular hydrogen is bent less to the left and passes through an electrostatic analyzer.

Section 4.2 describes the detectors and the data acquisition system used in this experiment. Section 4.3 describes the targets used in this experiment and their fabrication.

4.1 Accelerator

In its standard mode of operation, the 4-MV modified KN Van de Graaff accelerator produces two beams: protons (H^+) and molecular Hydrogen (H_2^+). Westerfeldt *et al.* [Wes88, Wes95] give a detailed description of the accelerator and the associated feedback system used to maintain a uniform beam energy. A brief overview is given below. Figure 4.2 shows a schematic of the accelerator and feedback system.

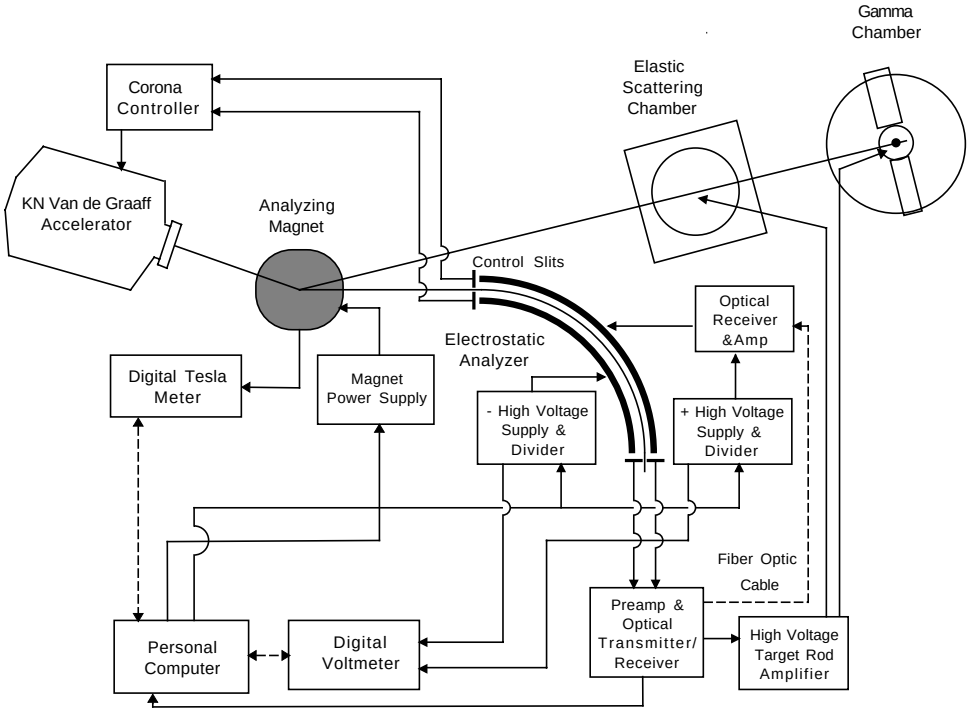

Figure 4.2: High Resolution Laboratory Control Loops. A current difference signal from the corona control slits is used to regulate voltage on the terminal. A current difference signal from the image slits is used to regulate the magnetic field, the potential on the outer plate, and to adjust the target rod voltage.

Inside the accelerator, a vulcanized rubber belt carries positive charge to the dome, raising the terminal to potentials as high as four million volts. A set of corona needles are

located between the dome and the wall of the accelerator. By adjusting the current flowing into these corona needles, the amount of positive charge on the dome can be increased or decreased in small amounts. The capacitive pickoff plate (CPO), an electrically isolated metal plate located inside the accelerator vessel, generates a signal which is representative of the AC components of the dome voltage. When the CPO signal is used as a feedback signal for the corona controller, AC fluctuations on the dome are reduced. However, because of the finite drift time of the ions between the dome and corona needles, only oscillations with frequencies less than 20 Hz are reduced.

An RF ion source, contained in the terminal of the accelerator, disassociates hydrogen ions in a Pyrex bottle. The ions are drawn into the accelerator tube where they are accelerated. The analyzing magnet separates the two ionic species by deflecting them by different amounts: the atomic H^+ (proton) beam is deflected 25° and then focused and steered onto a target several meters away, while the molecular HH^+ beam is deflected 17° into the electrostatic analyzer (ESA).

As the nearly mono-energetic molecular beam enters the ESA, the beam passes through the first of two lateral slits which are a part of the analyzer system. These slits, called the corona slits, feed back to the corona controller to help regulate the beam energy. With a constant magnetic field, changes in beam energy result in corresponding changes in the beam path through the analyzing magnet and therefore a difference in the amount of current on the two corona slits. The corona slit difference is fed back to the corona controller, reducing slow fluctuations of the beam energy by reducing their source: fluctuations of the terminal voltage. When this system is combined with the CPO feedback, the amplitude of terminal voltage fluctuations is reduced by almost an order of magnitude to $\approx 1\ \mathrm{kV}_{p-p}$. After passing through the corona slits, the molecular beam enters a gap between two curved, parallel plates. The gap is 4.57 mm wide, and the plates traverse a 90° arc. The plates are biased to equal and opposite voltages, with the total difference equal in magnitude to the desired beam energy divided by 111.37.

At the end of the arc is the second set of lateral slits, called the image slits. The

image slit difference signal, the amplified difference in the currents of the image slits, gives a real time measure of the terminal fluctuations up to a maximum of ± 1.7 keV at 1 kHz. The image slit difference signal is applied to the outer plate of the analyzer to increase stability. A DC component of the image slit difference corresponds to an incorrect magnet setting for the desired energy. The analyzing magnet can be placed in computer control so that the magnetic field is always correct for the desired energy.

If an energy step is desired, the voltage on the plates is changed. The voltage change on the plates causes the position of the beam on the image slits to be off-center, producing an image slit difference signal. The magnet setting changes to try to reduce the image slit difference signal, causing the position of the beam on the corona slits to be off-center. A difference signal from the corona slits causes the terminal voltage to change. In this way, the terminal voltage is changed to correspond to the desired energy and the correct magnetic field is automatically set.

The image slit difference signal is amplified by 111.37 and applied to the target rod, reducing energy fluctuations of the incoming proton beam before the protons hit the target. The combination of these two systems allows an overall beam energy resolution of 220 eV [Fra91], with an energy drift of 6 eV/hr [Wes88].

4.2 Detectors and Data Acquisition

The target chamber and detector system used in this experiment were described by Drake [Dra94] and are shown in Figure 4.3. The proton beam, separated from the molecular beam at the analyzing magnet, has been steered and focused to this chamber using quadrupole and dipole magnets. The protons interact with the ^{29}Si targets mounted on a target rod (which can hold up to five targets and a tuning ring) in the center of the chamber. Most of the beam passes through the target without interacting and is collected one meter away in a Faraday cup at the end of the beam line. Typical beam currents measured in the Faraday cup were $\sim$ 6-8 μA, with $\sim$ 30 nA on the tuning ring.

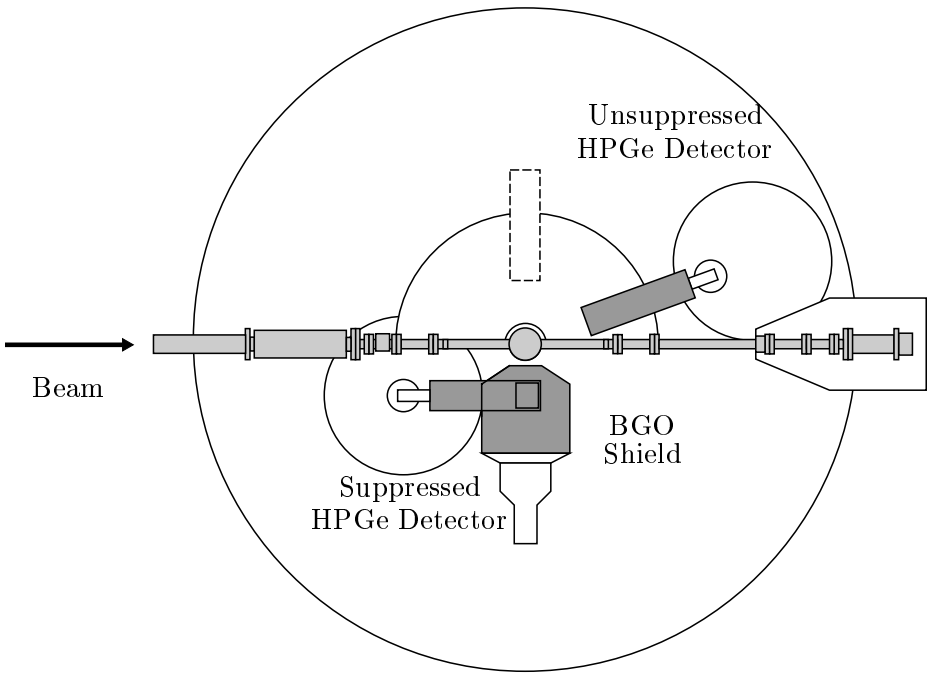

Figure 4.3: Compton-Suppressed Spectrometer. A high purity germanium detector (HPGe) and a Bismuth Germanate (BGO) suppression shield make up the Compton-suppressed germanium detector (CSGe). The other HPGe is unsuppressed (USGe) and is moved to five different angles: 25°, 38°, 50°, 63°, and 90°.

Surrounding the chamber at various angles, five detectors were present to observe the reaction: two high-purity Germanium (HPGe) detectors, one anti-Compton Bismuth Germanate (BGO) suppression shield, one Sodium Iodide (NaI) scintillator, and one Silicon surface barrier (SSB) charged particle detector.

The NaI and SSB detectors, not pictured in Fig. 4.3, were used to help locate the resonance of interest. The SSB detector was also used to monitor target deterioration. The two HPGe detectors and the BGO shield, together called the Compton-Suppressed Spectrometer (CSS), were used to measure the data of primary interest for this experiment. The suppressed HPGe detector (CSGe) remained fixed at 90° and was used as a monitor. Angular distribution data were taken with the unsuppressed HPGe (USGe) detector by moving this detector to different angles. These two HPGe detectors have a 60% efficiency compared to a 3 in. by 3 in. NaI(Tl) detector. The energy resolution is ≈ 2.0 keV for the 1332-keV transition in ^{60}Co.

The electronics configuration used for data collection with the CSS system is shown in Figure 4.4. Proper operation of the CSS system relies on coincidence between signals from the BGO suppression shield and the CSGe detector. For this reason, required information includes timing and energy of the photon interactions with the detector. Inside each detector, a charge pulse is collected and is input into a preamplifier. This preamplifier produces two pulses based on this charge pulse, an energy signal and a timing signal.

For each of the HPGe detectors, the energy signal is sent to a spectroscopy amplifier which integrates and shapes the pulse. Pile-up and ballistic deficit are two potential problems that arise with the energy signals. Pile-up occurs when two or more events occur nearly simultaneously in the detector and are shaped into a single pulse. Because the pulse is actually made up of two or more pulses, the amplitude of the pulse is not proportional to the photon energy of any of the events. Ballistic deficit occurs when the detector does not properly collect the charge within the shaping time of the amplifier. Both amplifiers (Tennelec TC245) used in these experiments are equipped with pulse pile-up rejection (PUR) and ballistic deficit correction (BDC) and both of these modes were always used during these

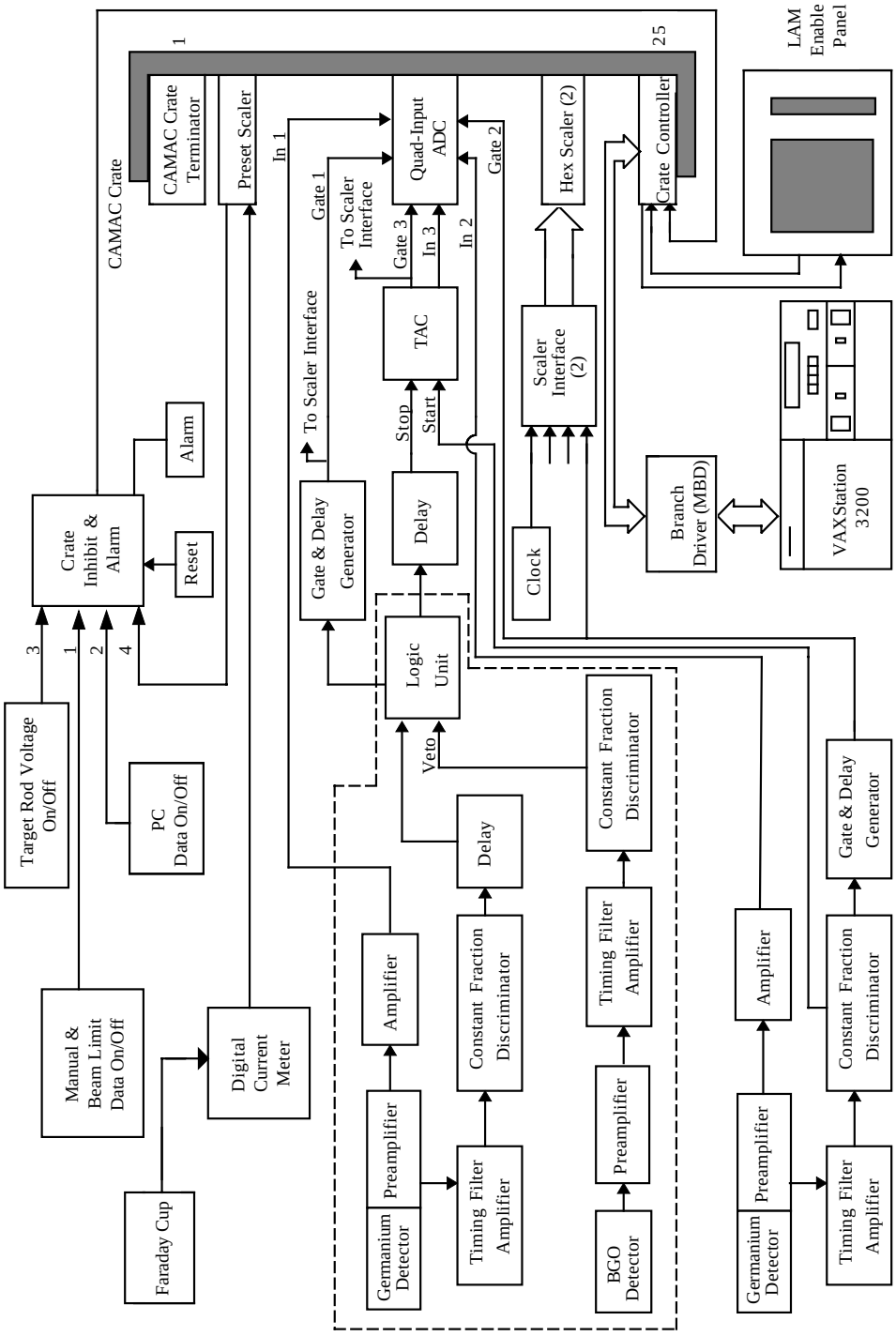

Figure 4.4: Data Acquisition Electronics for the HPGe and BGO Detectors.

experiments. The energy signals from each of the amplifiers go to different channels of a quad-input ADC. The energy signal from the BGO is not used.

The timing signals from the BGO and CSGe are used to suppress events for which all of the energy of the event is not deposited in the detector, including Compton scattering and pair production. These events result in simultaneous timing signals in both the BGO and the CSGe. Each of the timing outputs from these two detectors is sent to a Timing Filter Amplifier (TFA), which amplifies and shapes the signal. Each of the signals is then sent to a Constant Fraction Discriminator (CFD) module which produces a pulse a specified time after the leading edge of the input signal reaches a specified fraction of its amplitude. This allows determination of the exact time of the photon-detector interaction. The output for the BGO from the CFD is used as an input to a logic unit. The output for the CSGe from the CFD is delayed and also used as an input to the logic unit. Only CSGe signals which do not have a corresponding BGO signal are allowed to pass though the logic unit: only CSGe signals which correspond to γ-rays depositing their entire energy in the CSGe detector are kept.

The "good" events from the CSGe are sent to a Gate and Delay (G&D) module which shapes the signal appropriately for use as a gate in the CAMAC quad ADC. The USGe timing signals are sent through a similar, but simpler, path. The output from the USGe CFD is sent directly into its G&D module. The outputs from both G&D modules are also each sent to a CAMAC scaler. With an energy signal and a gate signal, the ADC digitizes the input signals and passes them directly to the Microprogrammable Branch Driver (MBD). From there, the signals are sent to the appropriate XSYS data area within the VAX memory and are stored as 8192 channel spectra.

Figure 4.5 shows a sample USGe spectra and Figure 4.6 shows a sample CSGe spectra. Both of these examples are at a proton bombarding energy of 1.7450 MeV, and have the same vertical scale.

The NaI and SSB detectors were also used in this experiment. Vavrina [Vav96] gives an excellent description of the specific data acquisition system used. The data acquisition

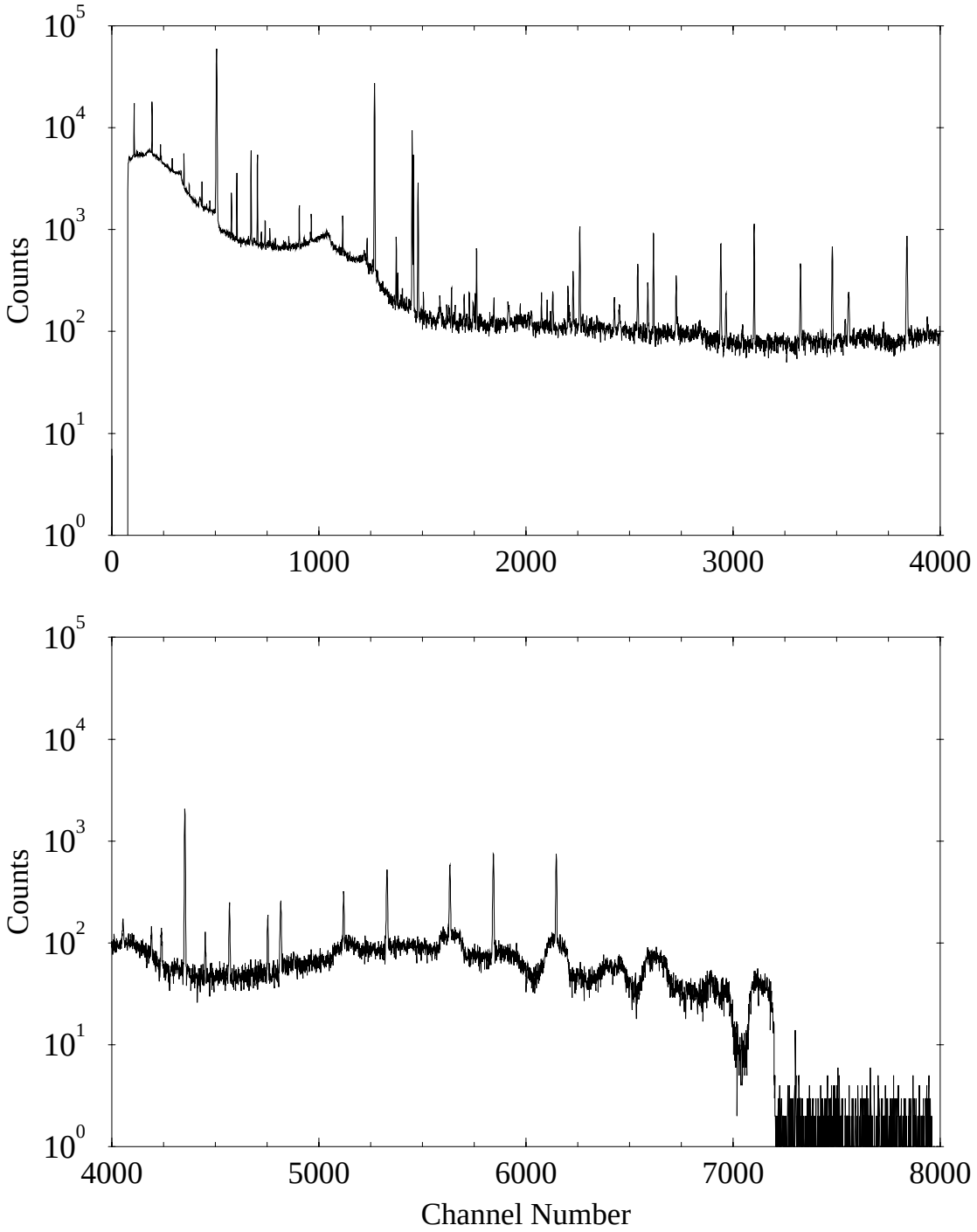

Figure 4.5: Unsuppressed Detector Spectrum. This data is measured with $E_p = 1.7450$ MeV. Counts are plotted on a log scale as a function of channel number. The top spectrum spans channel number 0 to channel number 4000, the bottom spectrum spans channel number 4000 to channel number 8000.

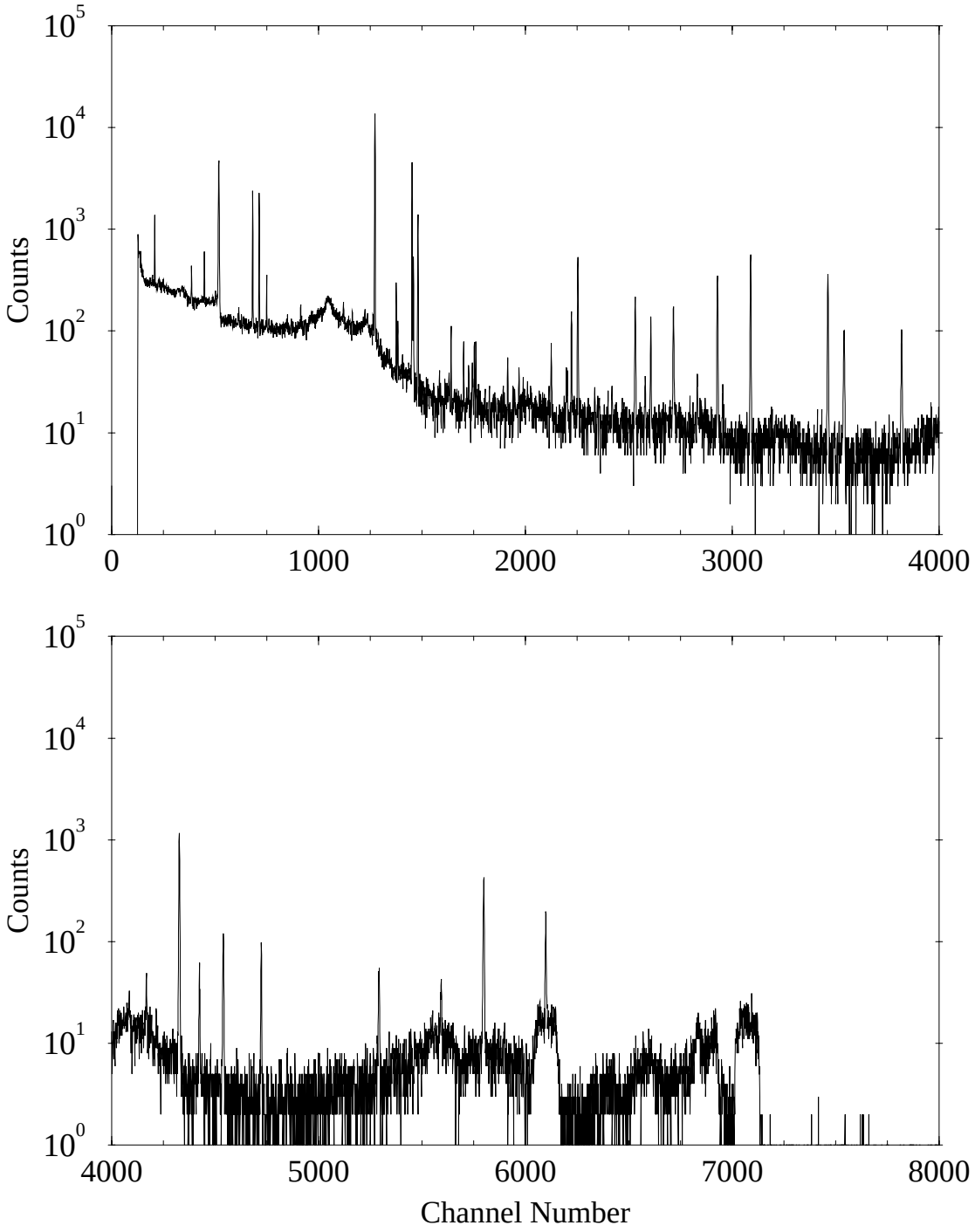

Figure 4.6: Compton-Suppressed Detector Spectrum. This data is measured with E_p = 1.7450 MeV. Counts are plotted on a log scale as a function of channel number. The top spectrum spans channel number 0 to channel number 4000, the bottom spectrum spans channel number 4000 to channel number 8000.

system for both detectors is identical, so it will only be explained once. The electronics configuration used for data collection with the NaI and SBB detectors is shown in Figure 4.7.

The output signal from the detector is sent to a preamplifier and then an amplifier. The unipolar energy pulse from the amplifier is sent to a multiplexer. The bipolar timing pulse from the amplifier is routed to a gated Single Channel Analyzer (SCA) and to a Timing Single Channel Analyzer (TSCA). The output from the TSCA is sent to the multiplexer and to a G&D. The G&D output is sent to a scaler module.

The multiplexer outputs to an ADC and to a buffer and also to a router/encoder, ensuring that the identity of each signal is maintained. The buffer interacts with the CAMAC crate and the MBD, which in turn sends the data to an appropriate XSYS data area. The signals from these detectors are usually stored as 512 channel spectra.

4.3 Targets

The ^{29}Si(p,γ) reaction was studied using thin ($\leq 3.0 \mu g/cm^2$) films of ^{29}Si evaporated onto 5.0 $\mu g/cm^2$ carbon foils. Since resonances with narrow widths (potentially less than 10 eV) and resonances with small spacings to adjacent resonances (spacings less than 1 keV) needed to be studied, the targets should generally have energy losses of $\approx$ 200 eV. Silicon targets were prepared as described below with a thickness of 1.5 $\mu g/cm^2$, corresponding to an energy loss of $\sim$ 170 eV, and with a thickness of 3.0 $\mu g/cm^2$, corresponding to an energy loss of $\sim$ 340 eV. For narrow resonances or for resonances with close neighbors, the thin (1.5 $\mu g/cm^2$) targets were used to take advantage of the good resolution. For resonances without such restrictions, the thick (3.0 $\mu g/cm^2$) targets were used to increase the count rate, thus reducing the amount of beam time needed for comparable statistics. The process for making both types of targets was essentially the same: Wallace [Wal96] gives an excellent description of the process, which will only be outlined here.

The 5.0 $\mu g/cm^2$ carbon foils were floated off slides and onto stainless steel target rings using distilled H_2O. These rings are then placed on a rack $\sim$15 cm away from a 0.005"

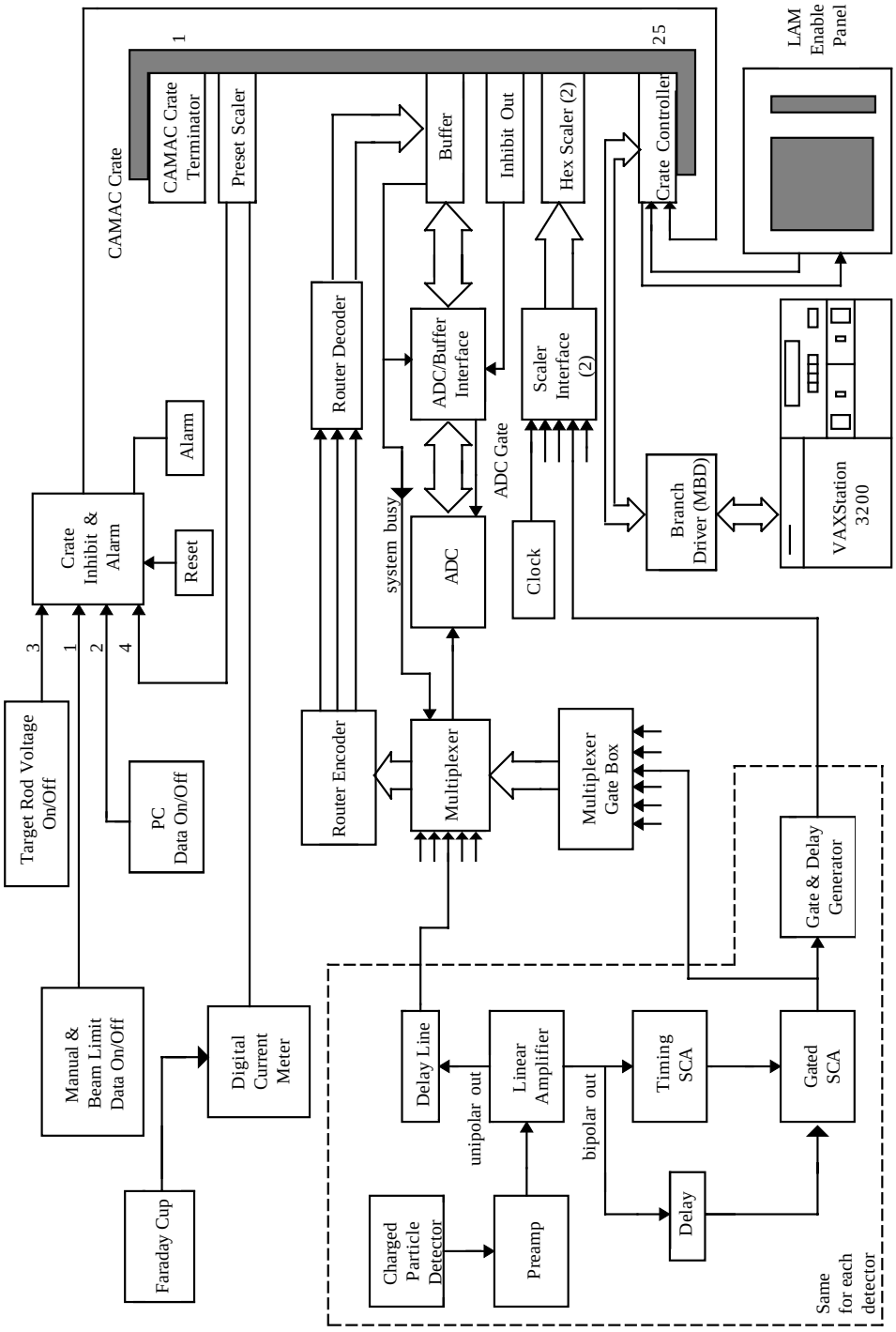

Figure 4.7: Data Acquisition Electronics for the NaI and SSB Detectors.

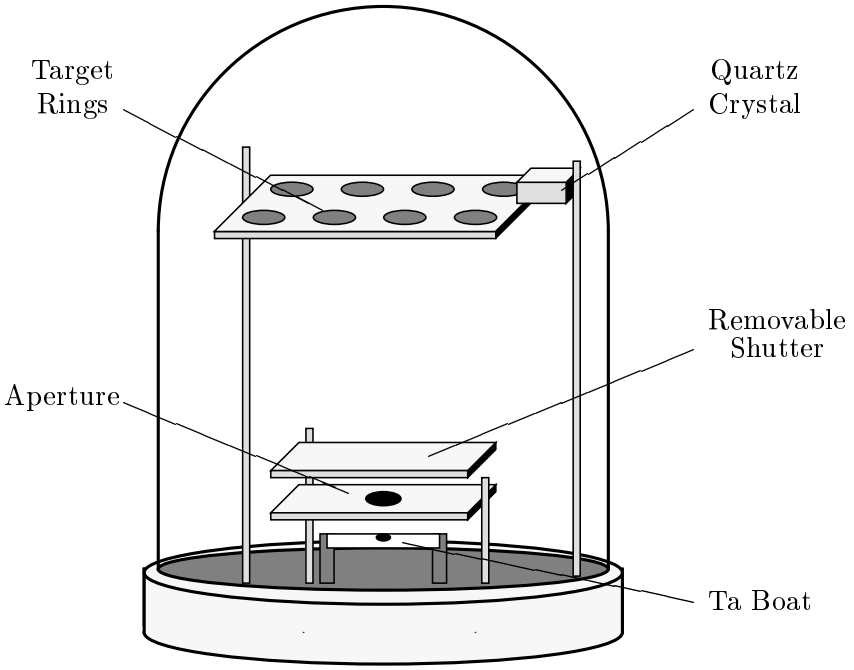

Figure 4.8: Target Preparation System. ^{29}Si is placed in the Ta Boat and heated by high-current electrodes. The material passes through the aperture and is evaporated on the target rings. A quartz crystal serves as a thickness monitor.

Ta closed boat inside a bell jar evacuated to < 1 μTorr. A schematic of the bell jar and its contents is shown in Figure 4.8. Tantalum (Ta) powder and silicon isotope ($^{29}SiO_2$), in a mass ratio of about 7:1, were placed inside the boat. The Ta powder is used as a reducing agent for the SiO_2. The isotope was in the form of SiO_2 and was enriched to $\sim 95\%$ ^{29}Si. A circular aperture of diameter 1.9 cm, positioned between the boat and the rings, hinders evaporated material from spreading too wide and depositing on the wrong side of the foils. A shutter was also positioned between the boat and the foils. After the boat was mounted on electrodes, high current was passed through the boat to increase the temperature of the boat and therefore the Ta and SiO_2 powder. After out-gassing the Ta boat at $\sim 1000^\circ$ C, the evaporation was performed at $\sim$ 1450 $^\circ$C with the shutter open. A quartz crystal was used to monitor target thickness. The thickness monitor was calibrated by comparing readings on the thickness monitor to target thicknesses determined by Coulomb scattering measurements.

Chapter 5

Data Collection and Analysis

5.1 Data Collection

Two HPGe detectors (described in Section 4.2) were used in this experiment. The Compton-suppressed high-purity germanium detector (CSGe) was located at 90° to minimize Doppler-shift effects. This detector monitored beam fluctuations and changes in target thickness as described in Section 5.2. The unsuppressed high-purity germanium detector (USGe) measured the angular distributions. Parity conservation guarantees that for an isolated resonance the γ-ray distributions will be symmetric about $\theta_{cm} = 90°$ (within the mass and energy ranges of this experiment, θ_{cm} and θ_{lab} are nearly equivalent). This requires that data need only to be measured between 0° and 90° to map the angular distribution. The CSS design does not allow the USGe to move to an angle less than 22.5°; therefore, 25° is the smallest angle that was used for these measurements. The largest angle that was used for these measurements was 90°. To space the data approximately evenly in $\cos^2\theta$, three other angles were chosen between these two endpoints: 38°, 50°, and 63°.

The resonances in ^{30}P that were selected had unknown or ambiguous J^π values or decay to states which have unknown or ambiguous J^π values. In addition, when a γ-ray mixing ratio value might assist in making a T assignment for either a resonance or an intermediate state, the resonance was also selected for study.

All resonances studied in this work were previously known. Excitation functions were measured by taking small energy steps and accumulating data at each energy in each of the detectors. Between steps, counts were summed in certain areas of the spectra. In this way, variations in the cross section could be plotted and examined. Known (p,γ) excitation functions [Wal96, Vav96] or known (p,p) excitation functions [Fra91, Nel83] were compared to our experimentally measured excitation functions. "Finding" a resonance in this way allowed the beam energy to be set to the exact resonance energy in a precise way. The resonance was also "re-found" after each stage of data acquisition, to allow for possible small drifts in the beam energy. Although the beam energy drift is only about $\sim$6 eV/hr under favorable conditions [Wes88], some resonances were studied for as long as three days.

For all of the data collected, the target was oriented such that there was a 30° angle between its normal and the beam direction. This ensured that the γ-rays would be unobstructed by the target rod or target ring in both of the detectors. All data were collected with the HPGe detector at 90°. Spectra were recorded for each resonance with the USGE at each of the five angles. Typically, 50 mC of charge was accumulated at each angle before moving the USGe detector to the next angle. After data were measured at each of the five angles, the process was repeated for as many as five times. In this way, data were accumulated for a total of 50 to 300 mC per resonance. The amount of charge accumulated for any one resonance was determined by the γ-ray strength and the statistics required.

5.2 Mixing Ratio Determination

The decay schemes for the resonances studied had been previously established [Vav96, Wal96], allowing the γ-rays of interest to be identified prior to the beginning of data collection. The HPGe detectors were calibrated using γ-rays from both a ^{152}Eu source and a well-studied ^{27}Al(p,γ) resonance (see description by Vavrina [Vav96]). With this calibration, the γ-rays of interest were easily recognized in the spectra. All γ-ray peaks in this work were fit using the GELIFT package. The yields and errors extracted from GELIFT

fits needed correction factors to account for dead time, nonuniform targets, beam profile changes, and non-ideal geometry.

5.2.1 Correction Factors

Dead time occurs when two signals occur too close in time to one another to allow processing of both signals. This happens when the ADC (Analog-to-Digital converter) is busy digitizing the first signal when the second signal arrives. A scaler records the total number of events, n_s, occurring in each detector. This is compared to the number of events actually processed by the ADC, n_a, and a dead time ratio, C_d, is defined as

$$C_d = \frac{n_s - n_a}{n_s}. \tag{5.1}$$

There is an associated dead time ratio for each detector (CSGe and USGe) at each USGe angle (25°, 38°, 50°, 63°, and 90°), where the subscripts have been suppressed. (Note that although the CSGe is always at 90°, CSGe spectra are often labelled the corresponding USGe angle – the angle at which the USGe was located when the CSGe data were taken.) The dead-time-corrected area, A_c, is determined from the raw (or measured) area, A_r, by

$$A_c = \frac{1}{1 - C_d} A_r. \tag{5.2}$$

Every peak analyzed in this experiment was corrected for dead time before any other analysis. Dead times for this work were usually less than 2% for the USGe and less than 5% for the CSGe.

Under ideal conditions, all spectra measured by a fixed detector should be the same for a given amount of total beam on target. However, changes in target thickness, beam stability, and energy resolution can affect the γ-ray luminosity. Changes in yield in the stationary CSGe detector for similar runs are used to correct final data to account for these factors. What follows is a general discussion of this method. This general method will be used specifically twice later in this section. Peaks of interest were selected from the spectra, fit using the GELIFT package, and were corrected with an appropriate dead time correction.

The monitor factor for a given angle θ takes into account the fluctuations observed in each of the corrected areas. There are N peaks used to determine each correction factor. A monitor correction factor C_m for each peak x at each angle θ is defined as

$$C_m^{\theta,x} = \frac{{}_{cs}A_c^{90,x}}{{}_{cs}A_c^{\theta,x}} \tag{5.3}$$

where ${}_{cs}A_c^{\theta,x}$ is the corrected area of peak x in the CSGe with the USGe at angle θ. In this way, $C_m^{90,x}$ is defined to be unity, and for other θ-values $C_m^{\theta,x}$ is a relative luminosity correction. The monitor correction for angle θ is given by the weighted average over all N peaks,

$$C_m^{\theta} = \frac{\sum_{x=1}^{N} w_m^{\theta,x} C_m^{\theta,x}}{\sum_{x=1}^{N} w_m^{\theta,x}}, \tag{5.4}$$

where $w_m^{\theta,x}$ is a weighting factor given by the inverse square of the uncertainty in each monitor correction factor $C_m^{\theta,x}$. The monitor correction factor C_m is applied to each corrected area A_c to obtain a monitor-corrected yield Y_m,

$$Y_m = C_m A_c \tag{5.5}$$

where the θ's have been suppressed for clarity.

The exact location where the beam intersects the target may not be the center of the axis of rotation of the unsuppressed germanium detector. This discrepancy could lead to an inaccurate description of the angular distribution. To correct for this problem, the relationship between the center of the chamber and the location of the USGe at each angle needs to be well understood. An isotropic source (^{152}Eu, the same source used for energy calibration of the detectors) was placed on the target rod in the target chamber, and data were collected in the two HPGe's. The process was repeated five times, with the USGe placed at each of the five angles. The γ-rays of interest, listed in Table 5.1, were fit using the GELIFT package. The raw areas measured with the CSGe are dead-time corrected (Equations 5.1 and 5.2) and used to extract a monitor correction factor $C_{m_1}^{\theta}$ (Equations 5.3 and 5.4). The raw areas measured with the USGe were also dead-time corrected. In a similar way to Equation 5.3, a geometry correction factor for each peak x at each angle θ

Table 5.1: ^{152}Eu source γ-Rays[1]. Energies of the γ-rays and their errors are given in keV. Intensities are normalized to the 1408.011 keV line.

E_γ (keV)	E_γ Error (keV)	I_γ (Relative)	I_γ Error (Relative)
244.692	0.002	3590	60
295.939	0.008	211	5
344.276	0.004	12750	90
367.789	0.005	495	8
411.115	0.005	1070	10
488.661	0.039	195	2
778.903	0.006	6190	80
867.388	0.008	1990	40
964.131	0.009	6920	90
1212.950	0.012	670	8
1299.124	0.012	780	10
1408.011	0.014	10000	30

[1] From [Fir96]

is defined as

$$C_g^{\theta,x} = \frac{{}_{us}A_c^{90,x} C_{m_1}^{90}}{{}_{us}A_c^{\theta,x} C_{m_1}^{\theta}} \tag{5.6}$$

where ${}_{us}A_c^{\theta,x}$ is the corrected area of peak x in the USGe (at angle θ) and is multiplied by the monitor correction factor $C_{m_1}^{\theta}$. As explained previously, $C_{m_1}^{90}$ is defined to be unity. In this way, $C_g^{90,x}$ is also defined to be unity. Similar to Equation 5.4, the monitor correction for angle θ is given by the weighted average over all N peaks,

$$C_g^{\theta} = \frac{\sum_{x=1}^{N} w_g^{\theta,x} C_g^{\theta,x}}{\sum_{x=1}^{N} w_g^{\theta,x}}, \tag{5.7}$$

where $w_g^{\theta,x}$ is a weighting factor, given by the inverse square of the uncertainty in each geometry correction factor $C_g^{\theta,x}$.

Next, γ-rays of interest are identified from the resonance spectra. Peaks from the CSGe are fit using the GELIFT package, dead-time corrected, and used to extract a monitor correction factor $C_{m_2}^{\theta}$. Peaks from the USGe are fit using the GELIFT package, dead-time

corrected, monitor corrected, and geometry corrected:

$$Y_c^{\theta,x} = C_g^{\theta} C_{m_2}^{\theta} \frac{1}{1 - C_d^{\theta}} A_r^{\theta,x}. \tag{5.8}$$

In addition to the above calculations, original uncertainties in each of the contributing raw areas were propagated through the entire calculation. In this way, corrected yields and their errors are extracted from the data. Table 5.2 gives sample raw areas, correction factors, and corrected yields (and their errors) for the $E_x = 7282.0$ keV to $E_x = 4182.65$ keV transition. Note that for the measurements at 25°, the raw area A_r is small and the monitor correction factor C_{m2} is large compared to other angles. This is due to a hole developing in the target during the 25° run. However, the monitor correction factor appropriately accounts for this, and the corrected yield Y_c is accurate.

Table 5.2: Example: Raw Areas, Correction Factors, and Corrected Yields. For the $E_x = 7282.0$ keV to $E_x = 4182.65$ keV transition, data are listed for each of the experimental angles θ.

θ (°)	A_r	C_d	C_g	C_{m2}	Y_c
25	1541 ± 60	1.0922	0.7606 ± 0.0017	1.8631 ± 0.0244	2376 ± 98
38	3141 ± 80	1.0998	0.7740 ± 0.0017	1.0288 ± 0.0112	2742 ± 76
50	3574 ± 84	1.0940	0.7786 ± 0.0017	0.9913 ± 0.0107	3010 ± 78
63	3964 ± 88	1.0930	0.8060 ± 0.0018	1.0095 ± 0.0109	3518 ± 87
90	3820 ± 87	1.0933	1.0000 ± 0.0000	1.0000 ± 0.0000	4176 ± 95

A FORTRAN program ANGDIST performs all of the above corrections to the raw areas and fits the corrected yields to Legendre polynomials of different order. For each (^{152}Eu and resonance) transition to be studied, raw areas, errors, and deadtimes from each detector at each different USGe angle are input into the ANGDIST code. Also input into ANGDIST are the possible J^{π} assignments for final states, and output from EGS4 simulations (for Q_2, Q_4, and Q_6 factors). In addition to all of the correction factors, ANGDIST outputs the corrected areas and errors for each transition at each angle. These coefficients will serve as input to the FORTRAN program MIXCALC. A typical plot of

the corrected data fit to Legendre polynomials plotted as a function of $\cos^2(\theta)$ is shown in Figure 5.1.

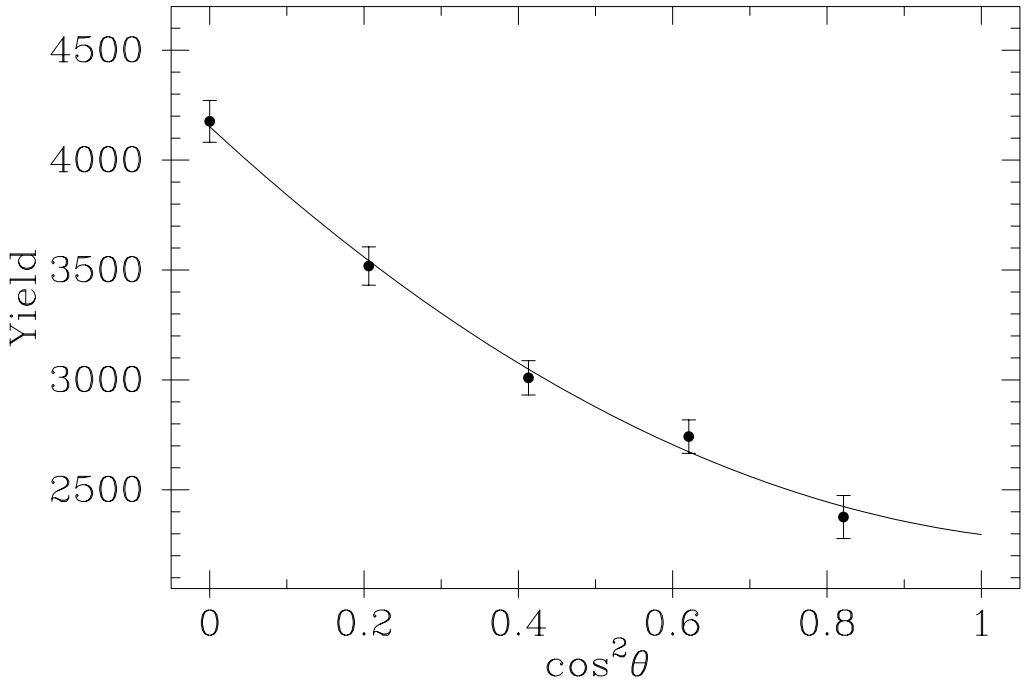

Figure 5.1: ANGDIST Fit of Experimental Data. This data for the $E_x = 7282.0$ keV to $E_x = 4182.65$ keV transition has been dead-time, geometry, and monitor corrected. The yield is plotted with the best fit line as a function of $\cos^2\theta$. Experimental error bars show the fit is good, as does the χ^2 value.

5.2.2 MIXCALC

The FORTRAN program MIXCALC uses output from the ANGDIST code and the J^π value of the resonance as input. The entire process must be repeated multiple times if there is ambiguity in the resonance J^π assignment. MIXCALC fits the mixing ratios in expressions of a_2, a_4, and a_6 (Section 3.2) to match experimentally measured yields. This is done in four distinct steps: a grid and a fine search for both primary and secondary transitions. These four steps are very similar.

The grid search for primary transitions varies the proton mixing ratio and each of the primary transition mixing ratios individually through their entire range. Each mixing

ratio can vary between $-\infty$ and $+\infty$. Typically, 13 to 19 (the exact number depends on the number of parameters) discrete values are chosen between these two limits, with an emphasis on the area around zero. This is visualized as a "grid" which spans the parameter space containing the mixing ratios. As each combination of mixing values is substituted into the a_2, a_4, and a_6 expressions, a χ^2 value is calculated, evaluating the goodness of fit of these a_2, a_4, and a_6 coefficients to the measured angular distributions. For each mixing ratio, the mixing ratio values which produce local minima in the χ^2 space are identified.

These mixing ratio values are used as starting points for the primary transition fine search. Instead of starting at discrete points, a χ^2 minimization procedure is used to "explore" the local area contained in the parameter space and to find the best possible local solution. The program also adjusts the overall normalization constant A_0 for each distribution. Since there can be more than one initial starting point for the fine search, there are often multiple local solutions after the fine search. Only those solutions within 1.0 of the best χ^2 value are retained.

These solutions are used as starting points to repeat the above two steps for a search on the secondary transition mixing ratios. For the secondary transition grid search, the values for primary transition mixing ratios are kept constant. During the secondary transition fine search, all mixing ratios are varied to find the best solution.

The output of the last step of the MIXCALC program is one or more values for the proton mixing ratio and each of the γ-ray mixing ratios and a χ^2 value for each of the combinations.

5.3 Mixing Ratios and Recommended Upper Limits

The transitions analyzed in this work are γ-ray transitions between two levels. The total γ-ray resonance width Γ_γ includes all of the open γ-ray channels and has been measured for many resonances [Fra91, End93]. The branching ratio for the i^{th} transition BR_i has also been measured for many resonances [Vav96, Wal96]. The partial γ-ray width for transition i

is the product of the resonance width and the branching ratio for the i^{th} channel, expressed as

$$\Gamma_{\gamma_i} = \Gamma_\gamma \mathrm{BR}_i. \tag{5.9}$$

In a similar way, the partial γ-ray width for transition i can be written as the sum of the partial γ-ray widths for transition i in channel QL, $\Gamma_{QL,i}$, over all of the open QL channels. In practice, a maximum of two of the QL channels is included (Section 3.2). If two are included, the sum is written as

$$\Gamma_{\gamma_i} = \Gamma_{E(L+1),i} + \Gamma_{ML,i}. \tag{5.10}$$

The γ-ray mixing ratio is defined (Equation 3.17) such that Equation 5.10 can be easily factored into the form

$$\Gamma_{\gamma_i} = \Gamma_{E(L+1),i} \left(\frac{1}{\delta^2_{\gamma,i}} + 1 \right) = \Gamma_{ML,i} \left(1 + \delta^2_{\gamma,i} \right). \tag{5.11}$$

Equation 5.9 is combined with Equation 5.11 to yield

$$\Gamma_\gamma \mathrm{BR}_i = \Gamma_{E(L+1),i} \left(\frac{1}{\delta^2_{\gamma,i}} + 1 \right) = \Gamma_{ML,i} \left(1 + \delta^2_{\gamma,i} \right). \tag{5.12}$$

The left hand side of Equation 5.12 contains well known measured quantities. The right hand side of Equation 5.12 contains mixing ratios, which were primarily determined in this work, and partial widths for transition i in channel QL. Partial transition widths are conveniently represented in Weisskopf units (W.u.). For a specific transition type, 1 W.u. [Wei51] corresponds to a width Γ_W (in eV) of

$$\begin{aligned}
\Gamma_W\,(M1) &= 2.072 \times 10^{-2} E_\gamma^3 \\
\Gamma_W\,(M2) &= 1.471 \times 10^{-8} A^{\frac{2}{3}} E_\gamma^5 \\
\Gamma_W\,(E1) &= 6.474 \times 10^{-2} A^{\frac{2}{3}} E_\gamma^3 \\
\Gamma_W\,(E2) &= 4.791 \times 10^{-8} A^{\frac{4}{3}} E_\gamma^5 \\
\Gamma_W\,(E3) &= 2.232 \times 10^{-14} A^2 E_\gamma^7.
\end{aligned} \tag{5.13}$$

These widths Γ_W depend on the mass number of the nucleus and the γ-ray energy (in MeV) of the specific transition. The reduced transition strength B in W.u. is the partial width of the transition divided by the appropriate Γ_W.

Endt [End93] has tabulated experimental values of γ-ray strengths in different mass regions. The types of transitions in this review were classified by their mass region, electromagnetic radiation type (i.e., E1 or M2), and as either isoscalar or isovector (IS or IV). Isoscalar refers to transitions with $|T_i - T_f| = 0$ and isovector refers to transitions with $|T_i - T_f| = 1$. RUL's were defined such that the probability of one of the logarithmic reduced transition strengths x exceeding the RUL for that transition character was 0.001 [End93]. Using this method, the RUL's for various transition characters were determined and are listed in Table 5.3. The recommendation of Endt is that a transition is extremely unlikely if the reduced transition strength B for that specific character exceeds the RUL.

Table 5.3: Recommended Upper Limits[1] (RUL's) on B. These RUL's are for $A =$ 21 - 44 nuclei. RUL's are given in Weisskopf units (W.u.) for each transition character. The transition characters are described by their electromagnetic character (E or M), their multipolarity (1, 2, or 3), and as either isoscalar (IS) or isovector (IV).

Transition Character	RUL (W.u.)
$E1_{IS}$	0.002
$E1_{IV}$	0.1
$E2_{IS}$	100
$E2_{IV}$	5
$E3_{IS}$	50
$M1_{IS}$	0.05
$M1_{IV}$	5
$M2_{IS}$	0.2
$M2_{IV}$	5

[1] From [End93]

5.4 Quantum Number Assignments

Although previous work (e.g., [End90, Vav96, Wal96]) had assigned many $J^\pi;T$ values for levels in ^{30}P, there remained many ambiguities. The purpose of this work was to study angular distributions of transitions which involve unknown quantum number assignments and attempt to make assignments based on these angular distributions.

For a given transition, it is possible that the $J^\pi;T$ value for the compound state, final state, or both are ambiguous. The expressions for a_2, a_4, and a_6 discussed in Equation 3.15 (example given in Equation 3.24) depend on the J^π values for both the compound and the final state. Different a_2, a_4, and a_6 expressions were calculated for each possible pair of compound and final state J^π values (see Appendix A). For each of these possibilities, the χ^2 values from the mixing ratio fine search (Section 5.2.2) were compared to 99% confidence levels. When χ^2 values exceeded 99% confidence levels, the combination of J^π values was unacceptable and was no longer considered.

The γ-ray mixing ratios determined from the analysis were used to eliminate further the ambiguities in the compound and final state J^π values. Since the RUL's described in Section 5.3 are dependent on T values, ambiguities were also eliminated in compound and final state T values. The experimentally determined γ-ray mixing ratio was used to divide the partial width of the transition into its two components. A reduced transition strength B for each of these components was compared to its respective RUL. When the reduced transition strength of one of these components exceeded the RUL, the combination of $J^\pi;T$ values was unacceptable and no longer considered.

5.5 Example: Decay of $E_x = 7282.0$ keV Resonance

The $E_x = 7282.0$ keV resonance was one level studied in this work. The analysis of the $E_x = 7282.0$ keV to $E_x = 4182.65$ keV transition will be outlined here. The resonance (compound state) had a previous assignment of $J = 3$, with no π or T information [Vav96]. The six primary transitions used in this analysis all had known $J^\pi;T$ values for their final

states, listed in Table 5.4.

Table 5.4: Transitions used in the Analysis of the E_x = 7282.0 keV Resonance. Each transition has its initial and final state energy, previous J^π and T assignment, and transition character listed.

Initial State			Final State			Transition Character	
E_x (keV)	J^π	T	E_X (keV)	J^π	T	EM	IS/IV
7282.0	3^- or 3^+	0 or 1	5576.90	2^+	1	E1 or M1/E2	IV or IS
7282.0	3^- or 3^+	0 or 1	4182.65	2^+	1	E1 or M1/E2	IV or IS
7282.0	3^- or 3^+	0 or 1	2839.9	3^+	0	E1 or M1/E2	IS or IV
7282.0	3^- or 3^+	0 or 1	2723.96	2^+	0	E1 or M1/E2	IS or IV
7282.0	3^- or 3^+	0 or 1	2539.03	3^+	0	E1 or M1/E2	IS or IV
7282.0	3^- or 3^+	0 or 1	1454.67	2^+	0	E1 or M1/E2	IS or IV
2839.9	3^+	0	709.02	1^+	0	E2	IS
4182.65	2^+	1	709.02	1^+	0	M1/E2	IS

Since all of the final states have known $J^\pi;T$, the MIXCALC calculation needs to be repeated twice: once for the J^π resonance value of 3^- and once for 3^+. First, only the primary γ-rays were fit. For the 3^- possibility, there were 23 degrees of freedom, which corresponded to a 99% confidence level of 41.6. The best fit from the primary transition fine searches yielded a χ^2 value of 57.9, which is above than the 99% confidence level. For the 3^+ possibility, there were 17 degrees of freedom, which corresponded to a 99% confidence level of 33.4. The best fit from the primary transition fine searches yielded a χ^2 value of 27.5. which is below the 99% confidence level. The 3^- possibility was removed from consideration, leaving a final J^π assignment for the 7282.0 resonance of 3^+.

The two secondary transitions listed in Table 5.4 were transitions between two states both of which had known $J^\pi;T$. A complete fit including both primary and secondary transitions had 24 degrees of freedom, which corresponded to a 99% confidence level of 43.0. The best fit from the secondary transition fine searches yielded a χ^2 value of 41.0, which is below than the 99% confidence level. This allows the 3^+ assignment and is consistent with the results from analysis of the primary transitions.

For four of the primary transitions studied, a mixing ratio was determined which was used to separate the components of each of the reduced transition strengths. For the other two primary transitions studied, two possible mixing ratios were obtained. These mixing ratios, and the separate components, are listed in Table 5.5. The reduced transition strengths can be compared to the RUL's in Table 5.3. The RUL for a transition of character $E2_{IS}$ is 100 W.u., which none of the determined strengths exceed. The RUL for a transition of character $E2_{IV}$ is 5 W.u.. Only the mixing ratio assignment of $+\infty$ for the 7282.0 $\rightarrow$ 5576.90 transition exceeds this RUL. However, since there is another possible mixing ratio for this transition which does not exceed the RUL, it leads to no isospin assignment. The RUL for a transition of character $M1_{IV}$ is 5 W.u., which none of the determined strengths exceed. The RUL for a transition of character $M1_{IS}$ is 0.05 W.u.. Only the mixing ratio assignment for the 7282.0 $\rightarrow$ 4182.65 transition exceeds this RUL. This implies the transition can not be isoscalar, suggesting the resonance has a T value of 0. Since the measured strength exceeds the RUL, an assignment of $T = 0$ is made. With an assignment of $T = 0$, the value of $+\infty$ for the 7282.0 $\rightarrow$ 5576.90 transition mixing ratio can be eliminated.

The analysis has allowed the umambiguous determination of five primary mixing ratios, and also assigned a $J^{\pi}; T$ value of $3^{+}; 0$ to the resonance.

Table 5.5: Reduced Transition Strengths for the $E_x = 7282.0$ keV Resonance. For each primary transition (designated by its final state energy, E_f) the experimentally determined mixing ratio value(s) is (are) listed. Given this mixing ratio value, each of the components of the total reduced transition strength (B(M1) and B(E2)) was calculated and is listed in Weisskopf units (W.u.).

E_f (keV)	δ_γ	B(M1) W.u.	B(E2) W.u.
5576.90	$+\infty$	0.	37.3632
	-0.182	0.0227	1.1979
4182.65	$+0.066$	0.0818	0.1721
2839.9	-1.40	0.0023	1.0467
2723.96	$+3.76$	0.0006	1.9271
2539.03	$+0.229$	0.0083	0.0894
1454.67	$+3.68$	0.0017	3.1000
	$+0.054$	0.0243	0.0097

Chapter 6

Quantum Number Assignments

A summary of the quantum number assignments will be presented in this chapter. All states are listed by their excitation energy E_x. Unbound states, when elastic scattering or capture data exists, are also listed by their bombarding energy E_p.

Most previous quantum number assignments are given by Endt [End93] and are updated by one of various sources [Fra91, Vav96, Wal96, Byb95]. The relative goodness of fits of angular distributions of primary and secondary transitions were used to eliminate J^π possibilities (Section 5.2.2). Comparison of experimentally determined transition strengths to RUL's [End93] were used to eliminate $J^\pi;T$ possibilities (Section 5.3).

Comparisons between experimentally determined levels and positive parity shell model calculations [Orm99] aid in removing remaining ambiguities. Comparisons between experimentally determined levels and parent states in ^{30}Si [End93] also aid in removing ambiguities. Ambiguities can be removed by identifying levels with the same quantum number assignments, or by the absence of a corresponding level. Appendix D lists all experimentally measured levels, levels from shell model calculations, and ^{30}Si levels. Note that in Table D, ^{30}Si states have been shifted by 677.29 keV to ease comparison.

6.1 Unbound States

E_x = 5714 keV

This level had a previous assignment of 5^+ or 7^+ [Fra91]. Comparison to shell model calculations (5104 keV) supports a $5^+;0$ assignment. An assignment of $5^+;0$ is made.

E_x = 5808 keV

This level had a previous assignment of 3^+ or 5^+ [Fra91]. Comparison to shell model calculations (5570 keV) supports a $5^+;0$ assignment. An assignment of $5^+;0$ is made.

E_x = 5890 keV

This level had a previous assignment of 1^+, 2^+, or 3^+, with a favored assignment of $T = 1$ [Fra91]. Comparison to shell model calculations (5887 keV) supports a $2^+;1$ assignment. Comparison to ^{30}Si parent states (5907 keV) supports a $2^+;1$ assignment. An assignment of $2^+;1$ is made.

E_x = 5907.7 keV E_p = 324.1 keV

This level had a previous assignment of 2^- [Fra91]. The absence of a $2^-;1$ ^{30}Si parent state in this energy region supports a $T = 0$ assignment. An assignment of $2^-;0$ is made.

E_x = 5933.96 keV

This level had a previous assignment of 2^-, 3^-, 3^+, 4^-, or 4^+ [Byb95]. Feeding from the $E_x = 8007.4$ keV resonance eliminated the 4^- assignment. Angular distribution analysis of the transitions from the $E_x = 8007.4$ keV resonance eliminated the $J^\pi = 2^-$ and 4^+ assignments. Angular distribution analysis of the transitions from the $E_x = 7560.49$ keV and $E_x = 7752.7$ keV resonances eliminated the 3^- assignment. RUL analysis of the $E_x = 7560.49$ keV to $E_x = 5933.96$ keV transition eliminated the $3^+;1$ assignment. Comparison

to shell model calculations (6166 keV) supports the $3^+;0$ assignment. An assignment of $3^+;0$ is made.

E_x = 6006.04 keV

This level had a previous assignment of 1^+, 2^-, 2^+, 3^-, 3^+, 4^-, or 4^+ [Wal96]. Analysis of the decay from the $E_x = 7203.0$ keV resonance to this state eliminated the 4^- assignment. Angular distribution analysis of the transitions from the $E_x = 7560.49$ keV resonance eliminated the 1^+, 2^-, 2^+, 3^-, and 4^+ assignments. RUL analysis of the $E_x = 7560.49$ keV to $E_x = 6006.04$ keV transition eliminated the $3^+;1$ assignment. Comparison to shell model calculations (6309 keV) supports a $3^+;0$ assignment. An assignment of $3^+;0$ is made.

E_x = 6050 keV

This level had a previous assignment of 0^+ or 1^+, with a suggested assignment of $T = 1$ [Fra91]. Comparison to shell model calculations (6217 keV) supports an assignment of $0^+;1$. Comparison to ^{30}Si parent states (6047 keV) supports an assignment of $0^+;1$. An assignment of $0^+;1$ is made.

E_x = 6051 keV

This level had a previous assignment of 3^+, 4^+, or 5^+ [Fra91]. Comparison to shell model calculations (6198 keV) supports an assignment of $4^+;1$. Comparison to ^{30}Si parent states (5957 keV) supports an assignment of $4^+;1$. An assignment of $4^+;1$ is made.

E_x = 6228.95 keV

This level had a previous assignment of 3^+ or 5^+ [Byb95]. Comparison to shell model calculations (6376 keV) supports an assignment of $5^+;0$. An assignment of $5^+;0$ is made.

E_x = 6269.6 keV E_p = 698.6 keV

This level had a previous assignment of $1^+;1$ or $2;1$ [End93]. Analysis of the E_x = 6269.6 keV to E_x = 1973.62 keV and E_x = 2539.03 keV transitions eliminated the 1^+ assignment. Angular distribution analysis of the E_x = 7306.3 keV resonance eliminated the 2^+ assignment. An assignment of $2^-;1$ is made.

E_x = 6468 keV

This level had a previous assignment of 5^+ or 6^- [Fra91]. The absence of $5^+;1$ or $6^-;1$ ^{30}Si parent states in this energy region support a $T = 0$ assignment. The absence of a 5^+ shell model state in this energy region supports a $\pi = -$ assignment. An assignment of $6^-;0$ is made.

E_x = 6520.8 keV E_p = 957.1 keV

This level had a previous assignment of 1^+ or 2^+ [End93]. Angular distribution analysis of the transitions from this resonance eliminated the 1^+ assignment. RUL analysis of the E_x = 6520.8 keV to E_x = 4502.32 keV transition eliminated the $T = 1$ assignment. Comparison to shell model calculations (6652 keV) supports an assignment of $2^+;0$. An assignment of $2^+;0$ is made.

E_x = 6597.7 keV E_p = 1038.0 keV

This level had a previous assignment of 3^-, 3^+, 4^-, 4^+, or 5^+ [Vav96]. Angular distribution analysis of the transitions from this resonance eliminated the 4^- assignment. Comparisons to shell model calculations (6607 keV) and ^{30}Si parent states (6627 keV) support a $4^+;1$ assignment. An assignment of $4^+;1$ is made.

E_x = 6607 keV

This level had a previous assignment of 3^+ or 5^+ [End90]. Comparison to shell model calculations (6574 keV) supports a $5^+;0$ assignment. An assignment of $5^+;0$ is made.

E_x = 6656 keV

This level did not have a previous assignment, but had a recommended $T = 1$ assignment [Fra91]. Comparisons to shell model calculations (6898 keV) and ^{30}Si parent states (6287 keV) support a $2^+;1$ assignment. An assignment of $2^+;1$ is made.

E_x = 6667.8 keV E_p = 1111.3 keV

This level had a previous assignment of 2^- or 3^+ [Vav96]. Angular distribution analysis of the transitions from this resonance eliminated the 2^- assignment. Comparisons to shell model calculations (7065 keV) support a $3^+;0$ assignment. An assignment of $3^+;0$ is made.

E_x = 6853.9 keV E_p = 1302.0 keV

This level had a previous assignment of 1^+ [Vav96]. RUL analysis of the E_x = 6853.9 keV to $E_x = 2937.87$ keV and $E_x = 4468.33$ keV transitions eliminated the $T = 1$ assignment. Comparison to shell model calculations (7085 keV) supports a $1^+;0$ assignment. An assignment of $1^+;0$ is made.

E_x = 6873.4 keV E_p = 1323.8 keV

This level had a previous assignment of 3^+ [Vav96]. RUL analysis of the E_x = 6873.4 keV to $E_x = 5508.55$ keV transition eliminated the $T = 0$ assignment. An assignment of $3^+;1$ is made.

E_x = 6877 keV E_p = 1327 keV

This level had a previous assignment of 2^- [Vav96]. Since there is no $2^-;1$ ^{30}Si parent state in this energy region, a $T = 0$ assignment is supported. An assignment of $2^-;0$ is made.

E_x = 6978.3 keV E_p = 1433.3 keV

This level had a previous assignment of $3^-;1$, 3^+, $4^-;1$, or 4^+ [Vav96]. Angular distribution analysis of the transitions from this resonances eliminated the 3^- assignment. RUL analysis of the $E_x = 6978.3$ keV to $E_x = 5508.55$ keV transition eliminated the $3^+;1$, $4^+;1$ assignments. RUL analysis of the $E_x = 6978.3$ keV to $E_x = 2937.87$ keV transition eliminated the $4^-;1$ assignment. Comparison to shell model calculations (7012 keV) supports a $4^+;0$ assignment. An assignment of $4^+;0$ is made.

E_x = 6981 keV

This level had a previous assignment of 5^+, 6^+, or 7^+ [Fra91]. Comparison to shell model calculations (6945 keV) supports a $5^+;0$ assignment. An assignment of $5^+;0$ is made.

E_x = 7045.0 keV E_p = 1502.3 keV

This level had a previous assignment of $2^-;0$, 3^-, or 4^- [Vav96]. Angular distribution analysis of the transitions from this resonance eliminated the 2^- and 3^- assignments. RUL analysis of the $E_x = 7045.0$ keV to $E_x = 6094.60$ keV transition eliminated the $4^-;1$ assignment. An assignment of $4^-;0$ is made.

E_x = 7119.1 keV 1578.7 keV

This level had a previous assignment of $1^-;1$, 1^+, 2, or 3 [Vav96]. RUL analysis of the $E_x = 7119.1$ keV to $E_x = 5508.55$ keV transition eliminated the 1^- and 1^+ possibilities. RUL analysis of the $E_x = 7119.1$ keV to $E_x = 1973.62$ keV and $E_x = 2539.03$ keV levels

also eliminated the $1^-;0$ assignment. Comparison to shell model calculations (7067 keV) supports a $2^+;0$ assignment. An assignment of $2^+;0$ is made.

E_x = 7179 keV E_p = 1639 keV

This level had a previous assignment of 1^- [Vav96]. RUL analysis of the E_x = 7179 keV to E_x = 709.02 keV and E_x = 3019.39 keV transitions eliminated the $1^-;0$ assignment. An assignment of $1^-;1$ is made.

E_x = 7199.1 keV

This level had a previous assignment of 5^+, 6^+, or 7^+ [Fra91]. Comparison to shell model calculations (7120 keV) supports a $6^+;0$ assignment. An assignment of $6^+;0$ is made.

E_x = 7203.0 keV E_p = 1663.9 keV

This level had a previous assignment of 1^+ or 2^+, with the 2^+ assignment preferred. [Vav96]. Angular distribution analysis of the transitions from this resonance eliminated the 1^+ assignment. The absence of a $2^+;1$ ^{30}Si parent state in this energy region supports a $T = 0$ assignment. An assignment of $2^+;0$ is made.

E_x = 7207.5 keV E_p = 1668.5 keV

This level had a previous assignment of $0^+;1$ or $1^+;1$ [Vav96]. Comparisons to shell model calculations (7456 keV) and ^{30}Si parent states (7319 keV) support a $0^+;1$ assignment. An assignment of $0^+;1$ is made.

E_x = 7282.0 keV E_p = 1745.0 keV

This level had a previous assignment of 3 [Vav96]. Angular distribution analysis of the transitions from this resonance eliminated the 3^- possibility. RUL analysis of the E_x = 7282.0 keV to E_x = 4182.65 keV transition eliminated the $3^+;1$ assignment. Comparison

with shell model states (7263 keV) supports the $T = 0$ assignment. An assignment of $3^+; 0$ is made.

E_x = 7283.4 keV E_p = 1747.2 keV

This level had a previous assignment of 2^+, with a preferred assignment of $2^+; 1$. [Vav96]. Comparisons with shell model states (7213 keV) and ^{30}Si parent states (7217 keV) support the $2^+; 1$ assignment. An assignment of $2^+; 1$ is made.

E_x = 7304.9 keV E_p = 1769.8 keV

This level had a previous assignment of 2^- [Wal96]. RUL analysis of the E_x = 7304.9 keV to $E_x = 4502.43$ keV transition eliminated the $2^-; 1$ assignment. An assignment of $2^-; 0$ is made.

E_x = 7306.3 keV E_p = 1771.5 keV

This level had a previous assignment of 2^-, with a preferred assignment of $2^-; 0$ [Wal96]. RUL analysis of the $E_x = 7306.3$ keV to $E_x = 6094.60$ keV and $E_x = 6269.60$ keV transitions eliminated the $2^-; 1$ assignment. An assignment of $2^-; 0$ is made.

E_x = 7322 keV E_p = 1788 keV

This level had a previous assignment of 1^- [Wal96]. Comparison to ^{30}Si parent states (7417 keV) supports the $1^-; 1$ assignment. An assignment of $1^-; 1$ is made.

E_x = 7347 keV

This level had a previous assignment of 5^+, 6^+, or 7^+ [Fra91]. Comparison to ^{30}Si parent states (7677 keV) supports a $5^+; 1$ assignment. An assignment of $5^+; 1$ is made.

E_x = 7383.4 keV E_p = 1.853 keV

This level had a previous assignment of 2 or 3 [Wal96]. Angular distribution analysis of the transitions from this resonance removed the 2^- and 3^+ possibilities. RUL analysis of the E_x = 7383.4 keV to E_x = 5933.96 keV transition eliminated the $2^+;0$ and $3^-;0$ assignments. The absence of $3^+;1$ and $2^+;1$ shell model states in this energy region supports a $3^-;1$ assignment. An assignment of $3^-;1$ is made.

E_x = 7493 keV E_p = 1963 keV

This level had a previous assignment of 1^+ [Wal96]. RUL analysis of the E_x = 7493 keV to E_x = 2937.87 keV transition eliminated the $1^+;0$ assignment. An assignment of $1^+;1$ is made.

E_x = 7560.5 keV E_p = 2033.6 keV

This level had a previous assignment of 3^+ [Wal96]. RUL analysis of the E_x = 7560.5 keV to E_x = 5576.90 keV transition eliminated the $3^+;1$ assignment. Comparison with shell model states (7443 keV) supports the $3^+;0$ assignment. An assignment of $3^+;0$ is made.

E_x = 7605.0 keV E_p = 2078.9 keV

This level had a previous assignment of 1^+ or 2^+ [Wal96]. Angular distribution analysis of the transitions from this resonance eliminated the 1^+ assignment. RUL analysis of the E_x = 7605.0 keV to E_x = 2937.87 keV transition eliminated the $2^+;0$ assignment. Comparisons to shell model states (7660 keV) and ^{30}Si parent states (7597 keV) support the $2^+;1$ assignment. An assignment of $2^+;1$ is made.

E_x = 7636.0 keV E_p = 2111.7 keV

This level had a previous assignment of 3 [Wal96]. Angular distribution analysis of the transitions from this resonance eliminated the 3^- possibility. The absence of a $3^+;1$ ^{30}Si parent state in this energy region supports a $T = 0$ assignment. An assignment of $3^+;0$ is made.

E_x = 7644.3 keV E_p = 2120.3 keV

This level had a previous assignment of 3^+, with a preferred assignment of $3^+;1$ [Wal96]. RUL analysis of the $E_x = 7644.3$ keV to $E_x = 4422.4$ keV transition eliminated the $3^+;1$ assignment. An assignment of $3^+;0$ is made.

E_x = 7647 keV E_p = 2117 keV

This level had a previous assignment of 4^-, 5^-, or 6^-, with a preferred T assignment of 1 [Fra91]. Comparison to ^{30}Si parent states (7717 keV) supports an assignment of $5^-;1$. An assignment of $5^-;1$ is made.

E_x = 7688.2 keV E_p = 2165.6 keV

This level had a previous assignment of $3^+;0$ or $4^-;0$ [Byb95]. Angular distribution analysis of the transitions from this resonance eliminated the 3^+ assignment. An assignment of $4^-;0$ is made.

E_x = 7742 keV E_p = 2222 keV

This level had a previous assignment of 1^- [Byb95]. The absence of a $1^-;1$ ^{30}Si parent state in this energy region supports a $T = 0$ assignment. An assignment of $1^-;0$ is made.

E_x = 7752.7 keV E_p = 2223.3 keV

This level had a previous assignment of 3^+ [Byb95]. RUL analysis of the E_x = 7752.7 keV to E_x = 5508.55 keV and E_x = 5933.96 keV transitions favors an assignment of $T = 1$. Comparison to ^{30}Si parent states (7547 keV) supports an assignment of $3^+; 1$. An assignment of $3^+; 1$ is made.

E_x = 7759.0 keV E_p = 2238.1 keV

Fixed detector measurements are consistent with assignments of $1^+; 0$, 2^+, $2^-; 0$, and 3^+. Previous angular distribution measurements [Rei85] eliminated the 2^- assignment. Angular distribution analysis of the transitions from this resonance eliminated the 1^+ and 2^- assignments. RUL analysis of the E_x = 7759.0 keV to E_x = 2723.96 keV transition eliminated the $2^+; 0$, $2^+; 1$, and $3^+; 0$ assignments. Angular distribution analysis of the E_x = 2723.96 keV to E_x = 0 keV transition eliminated the 2^+ assignment. Comparisons to shell model calculations (7894 keV) and ^{30}Si parent states (7757 keV) support a $3^+; 1$ assignment. An assignment of $3^+; 1$ is made.

E_x = 7786.4 keV E_p = 2267.9 keV

This level had a previous assignment of 2^-, 3^-, or 4^- [Wal96]. Angular distribution analysis of the transitions from this resonance eliminated the 3^- assignment and favors the 2^- assignment. The absence of a $2^-; 1$ ^{30}Si parent state in this energy region supports a $T = 0$ assignment. An assignment of $2^-; 0$ is made.

E_x = 7873.7 keV E_p = 2358.8 keV

This level had a previous assignment of 4^- [Wal96]. The absence of a $4^-; 1$ ^{30}Si parent state in this energy region supports a $T = 0$ assignment. An assignment of $4^-; 0$ is made.

E_x = 7883.8 keV E_p = 2369.2 keV

This level had a previous assignment of 3^+ or 4^+ [Wal96]. Angular distribution analysis of the transitions from this resonance eliminated the 3^+ possibility. Comparisons to shell model calculations (7690 keV) and ^{30}Si parent states (7897 keV) support a $4^+;1$ assignment. An assignment of $4^+;1$ is made.

E_x = 7892 keV E_x = 2377 keV

This level had a previous assignment of 2^- [Wal96]. Comparison to ^{30}Si parent states (8187 keV) supports a $2^-;1$ assignment. An assignment of $2^-;1$ is made.

E_x = 7920.9 keV E_p = 2406.3 keV

This level had a previous assignment of 2^+ [Wal96]. RUL analysis of the E_x = 7920.9 keV to E_x = 4736.4 keV transition eliminated the $2^+;1$ assignment. Comparison to shell model calculations (7701 keV) supports a $2^+;0$ assignment. An assignment of $2^+;0$ is made.

E_x = 7921.8 keV E_p = 2407.7 keV

This level had a previous assignment of $3^+;0$ [Wal96]. Comparison with shell model calculations (8027 keV) supports a $3^+;0$ assignment. An assignment of $3^+;0$ is made.

E_x = 7922 keV E_p = 2409 keV

This level had a previous assignment of 2^-, 3, 4, and 5^- [Wal96]. Angular distribution analysis of the transitions from this resonance eliminated the 2^- and 3^- assignments, and favor a 4^+ assignment. The 5^- possibility was ruled out on the grounds it requires an $\ell = 5$ proton. Angular distribution analysis of the E_x = 2839.9 keV to E_x = 709.02 keV transition eliminated the 3^+ assignment. Proton mixing ratios are consistent with the 4^+

assignment. Comparison with shell model calculations (7765 keV) supports a $4^+;0$ assignment. An assignment of $4^+;0$ is made.

E_x = 7932 keV E_p = 2418 keV

This level had a previous assignment of 0^+ [Wal96]. Comparison with ^{30}Si parent states (8117 keV) supports a $0^+;1$ assignment. An assignment of $0^+;1$ is supported.

E_x = 7996.7 keV E_p = 2486.6 keV

This level had a previous assignment of 1^+ [Wal96]. RUL analysis of the E_x = 7996.7 keV to $E_x = 5506.1$ keV transition eliminated the $1^+;0$ possibility. An assignment of $1^+;1$ is made.

E_x = 8001 keV E_p = 2490 keV

This level had a previous assignment of 1^- [Wal96]. The absence of a $1^-;1$ ^{30}Si parent state in this energy region supports a $T = 0$ assignment. An assignment of $1^-;0$ is made.

E_x = 8007.4 keV E_p = 2497.9 keV

This level had a previous assignment of 1^+ or 2^+ [Wal96]. Angular distribution analysis of the transitions from this resonance eliminated the 1^+ assignment. RUL analysis of the E_x = 8007.4 keV to E_x = 4182.65 keV transition eliminated the $2^+;0$ assignment. Comparison to shell model states (7999 keV) and ^{30}Si parent states (7937 keV) support a $2^+;1$ assignment. An assignment of $2^+;1$ is made.

E_x = 8014.3 E_p = 2505.6 keV

This level had a previous assignment of 2^+ [Wal96]. RUL analysis of the E_x = 8014.3 keV to $E_x = 5508.55$ keV transition eliminated the $2^+;1$ assignment. Comparison

with shell model calculations (8083 keV) support the $2^+;0$ assignment. An assignment of $2^+;0$ is made.

6.2 Bound States

E_x = 4926.4 keV

This level had a previous assignment of $5^-;0$ [End93] or 3^- [Fra91]. Reinecke [Rei85] measured an 11% branch to the 1454.67 keV level, which is not allowed for a 5^- assignment. $5^-;1$ is not allowed by a transition strength from the 7049.4 keV level. Both a $3^-;0$ and $5^-;0$ are supported by comparison to shell model states. The absence of a $3^-;1$ ^{30}Si parent state in this energy region supports a $T = 0$ assignment. An assignment of $3^-;0$ is made.

E_x = 4937.9 keV

This level had a previous assignment of 1^- or 1^+ [End93], or $1^-;0$, $1^-;1$, $1^+;0$, or $2^+;0$ [Fra91]. RUL analysis of the E_x = 7562.5 keV to E_x = 4937.9 keV transition eliminated the $1^+;0$ assignment. RUL analysis of the E_x = 4937.9 keV to E_x = 677.29 keV eliminated the $2^+;0$ assignment. Based on experimental results, this level can only have a $J^\pi;T$ assignment of $1^+;1$ or $2^+;1$, or a J^π assignment of 1^-. The absence of a $1^-;1$ ^{30}Si parent state in this energy region support a $T = 0$ assignment. The absence of 1^+ or 2^+ shell model states in this energy region supports a 1^- assignment. An assignment of $1^-;0$ is made.

E_x = 5028 keV

This level had a previous assignment of 4^-, 5^-, 5^+, or 6^-, with favored assignments of 5^- or 5^+. The absence of $4^-;1$, $5^-;1$, $5^+;1$, or $6^-;1$ ^{30}Si parent states in this energy region support a $T = 0$ assignment. The absence of a 5^+ shell model state in this energy region supports a $\pi = -$ assignment. An assignment of $5^-;0$ is made.

E_x = 5206.6 keV

This level had a previous assignment of 3^+, with a favored assignment of $3^+;0$ [Fra91]. Comparisons with shell model calculations (5654 keV) and ^{30}Si parent states (5507 keV) support a $3^+;1$ assignment. A $3^+;1$ assignment is made.

E_x = 5231.6 keV

This level had a previous assignment of 2^- [End93] or 2^- or 4^- [Fra91]. The absence of $2^-;1$ or $4^-;1$ ^{30}Si parent states in this energy region support a $T = 0$ assignment. An assignment of $2^-;0$ is made.

E_x = 5411.13 keV

This level had a previous assignment of 0^- or 2^- [End93, Fra91]. RUL analysis of the $E_x = 7688.15$ keV to $E_x = 5411.13$ keV transition eliminated the 0^- assignment. The absence of a $2^-;1$ ^{30}Si parent state in this energy region supports a $T = 0$ assignment. An assignment of $2^-;0$ is made.

E_x = 5506.1 keV

This level had a previous assignment of $1;0$ [End93] or $1^-;0$, $1^+;0$, or $2^+;0$ [Fra91]. RUL analysis of the $E_x = 5506.1$ keV to $E_x = 677.29$ keV transition eliminated the $2^+;0$ assignment. Endt claims the $T = 0$ assignment is determined from γ-ray feeding. The absence of a $1^+;0$ shell model state in this energy region supports a $1^-;0$ or $2^+;0$ assignment. An assignment of $1^-;0$ is made.

E_x = 5508.55 keV

This level had a previous assignment of 1^+, 2^-, 2^+, 3^-, or 3^+ [Fra91] with a suggested T assignment of 1. Angular distribution analysis of the transitions from the $E_x = 8014.3$ keV resonance eliminated the 2^- assignment. Angular distribution analysis of

the transitions from the $E_x = 7752.7$ keV resonance eliminated the 1^+ and 3^- assignments. Angular distribution analysis of the transitions from the $E_x = 7045.0$ keV resonance eliminated the 2^+ assignment. RUL analysis of the $E_x = 7560.5$ keV to $E_x = 5508.55$ keV transition eliminated the $3^+;1$ assignment. Comparison to shell model calculations (5574 keV) supports a $3^+;0$ assignment. An assignment of $3^+;0$ is made.

E_x = 5576.90 keV

This level had a previous assignment of $1^+;1$ or $2^+;1$ [Fra91]. Angular distribution analysis of the $E_x = 7560.49$ keV resonance eliminated the $J^\pi = 1^+$ assignment. Comparison to shell model calculations (5741 keV) and ^{30}Si parent states (5487 keV) supports a $2^+;1$ assignment. An assignment of $2^+;1$ is made.

E_x = 5595 keV

This level had a previous assignment of 4^+ [Fra91]. Comparison to shell model calculations (5455 keV) supports a $4^+;0$ assignment. An assignment of $4^+;0$ is made.

6.3 Unassigned Levels

After subjecting all levels to the analysis presented earlier in this dissertation, seven levels remained still unassigned. These levels are listed in Table 6.1. Two of the levels, at $E_x = 6295$ keV and $E_x = 6791$ keV, have previous assignments of greater than $J = 5$, which is higher than the maximum J cutoff used in this work for sequences. The other five levels are all assigned $T = 0$, due to an absence of appropriate ^{30}Si parent states in their respective energy ranges. There is no information concerning the $E_x = 7270$ keV state.

Since there are six other $5^+;0$ states, one other $6^+;0$ state, and no other $7^+;0$ states, a $5^+;0$ assignment is suggested for the $E_x = 6181$ keV state. Since there are four other $4^-;0$ states, one other $5^-;0$ state, and one other $6^-;0$ state, a $4^-;0$ assignment is suggested for the $E_x = 6361$ keV state. No assignment is made for the $E_x = 5933$, 6295, 6791, 7370,

and 7803 keV states and they are omitted from the statistical analysis.

Table 6.1: Unassigned ^{30}P Levels. Previous assignments are from Frankle [Fra91].

E_x (keV)	$J^\pi;T$ assignment previous	current
5993	0^- 1^- 2^-	$0^-;0$ $1^-;0$ $2^-;0$
6181	5^+ 6^+ 7^+	$5^+;0$
6295	>5	>5
6361	4^- 5^- 6^-	$4^-;0$
6791	>5	>5
7370	?	
7803	2^- 3^- 4^-	$2^-;0$ $3^-;0$ $4^-;0$

6.4 Summary

The final assignments made in Sections 6.1, 6.2, and 6.3 are listed in Table 6.2.

Table 6.2: All ^{30}P States.

E_x (keV)	$J^\pi;T$
0.0	$1^+;0$
677.29	$0^+;1$
709.02	$1^+;0$
1454.67	$2^+;0$
1973.62	$3^+;0$
2539.03	$3^+;0$
2723.96	$2^+;0$
2839.9	$3^+;0$
2937.87	$2^+;1$
3019.39	$1^+;0$
3733.9	$1^+;0$
3835.9	$2^+;0$
3928.9	$3^+;0$
4143.67	$2^-;0$
4182.65	$2^+;1$

Table 6.2 *(continued)*

E_x (keV)	$J^\pi;T$
4232.2	$4^-;0$
4298.1	$4^+;0$
4343.6	$5^+;0$
4422.4	$2^+;0$
4468.33	$0^+;1$
4502.32	$1^+;1$
4626.55	$3^-;0$
4736.4	$3^+;0$
4926.4	$3^-;0$
4937.9	$1^-;0$
4941.0	$1^+;0$
5028	$5^-;0$
5206.6	$3^+;1$
5231.6	$2^-;0$
5411.13	$2^-;0$
5506.1	$1^-;0$
5508.55	$3^+;0$
5576.90	$2^+;1$
5595	$4^+;0$
5701.7	$1^+;0$
5714	$5^+;0$
5808	$5^+;0$
5890	$3^+;1$
5907.7	$2^-;0$
5933.96	$3^+;0$
5993	$0^-;0,\ 1^-;0,\ 2^-;0$
5997.1	$1^+;0$
6006.04	$3^+;0$
6050	$0^+;1$
6051	$4^+;1$
6094.6	$3^-;1$
6181	$5^+;0$
6228.95	$5^+;0$
6269.6	$2^-;1$

Table 6.2 *(continued)*

E_x (keV)	$J^\pi;T$
6295	> 5
6299.3	$3^+;0$
6361	$4^-;0$
6468	$6^-;0$
6481.4	$1^+;0$
6520.8	$2^+;0$
6597.7	$4^+;1$
6607	$5^+;0$
6656	$2^+;1$
6667.8	$3^+;0$
6791	> 5
6853.9	$1^+;0$
6873.4	$3^+;0$
6877	$2^-;0$
6921	$1^-;0$
6978.3	$4^+;0$
6981	$5^+;0$
7014.9	$2^-;0$
7045.0	$4^-;0$
7049.4	$4^-;1$
7119.1	$2^+;0$
7179	$1^-;1$
7199.1	$6^+;0$
7203.0	$2^+;0$
7207.5	$0^+;1$
7223.3	$2^-;1$
7282.0	$3^+;0$
7283.4	$2^+;1$
7304.9	$2^-;0$
7306.3	$2^-;0$
7322	$1^-;1$
7347	$5^+;1$
7370	?
7383.4	$3^-;1$

Table 6.2 *(continued)*

E_x (keV)	$J^\pi;T$
7493	$1^+;1$
7560.5	$3^+;0$
7562.5	$2^+;1$
7579.9	$2^-;0$
7605.0	$2^+;1$
7636.0	$3^+;0$
7647	$5^-;1$
7644.3	$3^+;0$
7688.2	$4^-;0$
7742	$1^-;0$
7749.3	$1^+;0$
7752.7	$3^+;1$
7759.0	$3^+;1$
7786.4	$2^-;0$
7803	$2^-;0$, $3^-;0$, $4^-;0$
7826.3	$2^-;0$
7873.7	$4^-;0$
7883.8	$4^+;1$
7892	$2^-;1$
7920.9	$2^+;0$
7921.8	$3^+;0$
7922	$4^+;0$
7932	$0^+;1$
7996.7	$1^+;1$
8001	$1^-;0$
8007.4	$2^+;1$
8014.3	$2^+;0$

Chapter 7

Results

The goal of this work was to examine the fluctuation properties of ^{30}P and compare them with previous results for ^{26}Al. The quantum numbers J and π represent conserved symmetries in these nuclei. However, since the Coloumb force is not negligible (though relatively small when compared to the strong force), T is only an approximate symmetry. Theory predicted that the fluctuation patterns in the presence of a broken symmetry rapidly return to the fluctuation patterns in the absence of the symmetry [Dys62, Pan81]. Results from ^{26}Al showed fluctuation properties midway between GOE and Poisson and independent of isospin [Shr90], consistent with the predictions of Dyson and Pandey. One of the goals of these measurements of ^{30}P was to examine these statistical properties in a different nucleus. One method of doing this is to compare fluctuations with T considered as a good quantum number to those where T is not considered as a symmetry of the system.

The experimental data were subjected to the two tests described in Chapter 2: the nearest-neighbor spacing distribution (NNSD) and the Dyson-Mehta Δ_3 statistic. The NNSD reveals the short range order of a system and the Δ_3 statistic the long range order. The NNSD is expressed in terms of x, the ratio of a given nearest neighbor spacing to the average level spacing. The Δ_3 statistic is a function of L, in integer units of the average level spacing. Each of these tests can be quantified by an interpolation parameter, ω for the NNSD and μ for the Δ_3 statistic, whose value is unity when the system has GOE

Table 7.1: Sequences used for ^{30}P Analysis. Only sequences with $J \leq 5$ are included, with energies between $E_x = 0$ keV and 8015 keV. Sequences with fewer than five members are shown in parenthesis and were not used in the analysis.

J^π	Number of levels		
	Total	T=0	T=1
0^-	(0)	(0)	(0)
0^+	5	(0)	5
1^-	7	5	(2)
1^+	13	10	(3)
2^-	14	11	(3)
2^+	17	9	8
3^-	(4)	(2)	(2)
3^+	20	16	(4)
4^-	6	5	(1)
4^+	7	(4)	(3)
5^-	(2)	(1)	(1)
5^+	8	7	(1)
6^-	(1)	(1)	(0)
6^+	(1)	(1)	(0)
7^-	(0)	(0)	(0)
7^+	(0)	(0)	(0)
Analyzed	97	63	13
Total	105	72	33

behavior and zero when the system has Poisson behavior. Each test requires that the levels be separated into sequences. A sequence is defined as a group of levels which have the same quantum numbers. Two types of sequences were used in this work. The J^π sequences considered only the quantum numbers J and π. The $J^\pi;T$ sequences considered the quantum numbers J, π, and T. Only sequences which contain at least five members were used in this analysis. In addition, no sequences with J values greater than five were used, since the number of states with these J values are small.

The sequences used in this analysis are listed in Table 7.1. The sequences are listed according to their J^π values, with only those members with energies less than 8015 keV

Table 7.2: Sequences Used for ^{26}Al Analysis[a]

J^π	Number of levels		
	Total	$T=0$	$T=1$
1^-	10	8	2
1^+	19	16	3
2^-	11	9	2
2^+	25	14	11
3^-	12	10	2
3^+	23	18	5
4^-	10	9	1
4^+	20	13	7
5^+	12	10	2
Total $^+$	99	71	28
Total $^-$	43	36	7
Total	142	107	35

[a]From Shriner *et al.* [Shr90].

included. The second column ("Total") lists the total number of members in each sequence. The third and fourth columns ("$T=0$" and "$T=1$") list the total number of members in each of the isospin sequences. There are ten J^π sequences and eight $J^\pi;T$ sequences with $T=0$ which have more than five members and are used in this analysis. There are only two $J^\pi;T$ sequences $T=1$. There are approximately twice as many positive parity states as negative parity states.

For comparison, Table 7.2 lists the sequences used in the ^{26}Al analysis [Shr90]. Approximately 50% more total levels and 50% more $T=0$ levels were available for the ^{26}Al analysis than for the ^{30}P analysis. The number of $T=1$ levels was approximately the same. The fractional number of $T=0$ states is smaller for ^{26}Al (25%) than for ^{30}P (31%). There are too few $T=1$ sequences in either nucleus to allow for a proper analysis of these sequences by themselves. The fractional number of positive parity states is approximately the same in ^{26}Al and ^{30}P.

The average NNSD for the J^π sequences is shown in Figure 7.1. For the ^{30}P analysis,

six positive parity J^π sequences were used: 0^+, 1^+, 2^+, 3^+, 4^+, and 5^+. Three negative parity J^π sequences were used: 1^-, 2^-, and 4^-. For this small number of levels in each sequence, the independence from histogram bin size makes the $F(x)$ a more reliable test. The experimental data for both the positive parity and negative parity sequences are in closer agreement with GOE statistics than with Poisson statistics. For the negative parity sequences, the data lie slightly above the GOE curve for $x < 1$, and slightly below the GOE curve for $x > 1$. This behavior is present in the positive parity sequences, though not as extreme for the $x > 1$ region. A total of nine J^π sequences were used in this analysis. The behavior observed in the positive and negative parity sequences is also observed when all J^π sequences were included. The Δ_3 statistic for these sequences is shown in Figure 7.2. The experimental data for both positive and negative parity sequences are again in closer agreement with GOE statistics than with Poisson statistics. For both sets of sequences, the data closely match the GOE curve with $L \leq 2$, but lie midway between GOE and Poisson for $L > 2$. The $L > 2$ behavior is more evident in the positive parity sequences because there are more levels, allowing for greater values of L.

The average NNSD for the $J^\pi;T$ sequences with $T = 0$ are shown in Figure 7.3. Four positive parity $J^\pi;T$ sequences with $T = 0$ were used: $1^+;0$, $2^+;0$, $3^+;0$, and $5^+;0$. Three negative parity $J^\pi;T$ sequences with $T = 0$ were used: $1^-;0$, $2^-;0$, and $4^-;0$. As with the J^π sequences, the data are in closer agreement with GOE statistics than with Poisson statistics. For the negative parity sequences, the behavior of the cumulative spacing distribution is similar to the J^π sequences: the data are slightly above the GOE curve for $x < 1$, and slightly below it for $x > 1$. The positive parity sequences shows a slightly different character. For $x < 0.75$, the data are slightly above the GOE curve. Between $x = 0.75$ and $x = 1.25$, the data are slightly below the GOE curve. Then, at $x > 1.25$, the data match the curve very well. In addition to the seven $J^\pi;T$ sequences listed above, the $0^+;1$ and $2^+;1$ $J^\pi;T$ sequences were used in this analysis. Nine total $J^\pi;T$ sequences were used in this analysis. The trend for all $J^\pi;T$ sequences is similar to the positive parity $J^\pi;T$ sequences with $T = 0$, although slightly smoother. The Δ_3 statistic for these sequences is

Figure 7.1: The NNSD for the J^π Sequences. The positive parity J^π sequences (top left), negative parity J^π sequences (top right), and all parity J^π sequences (bottom) are shown.

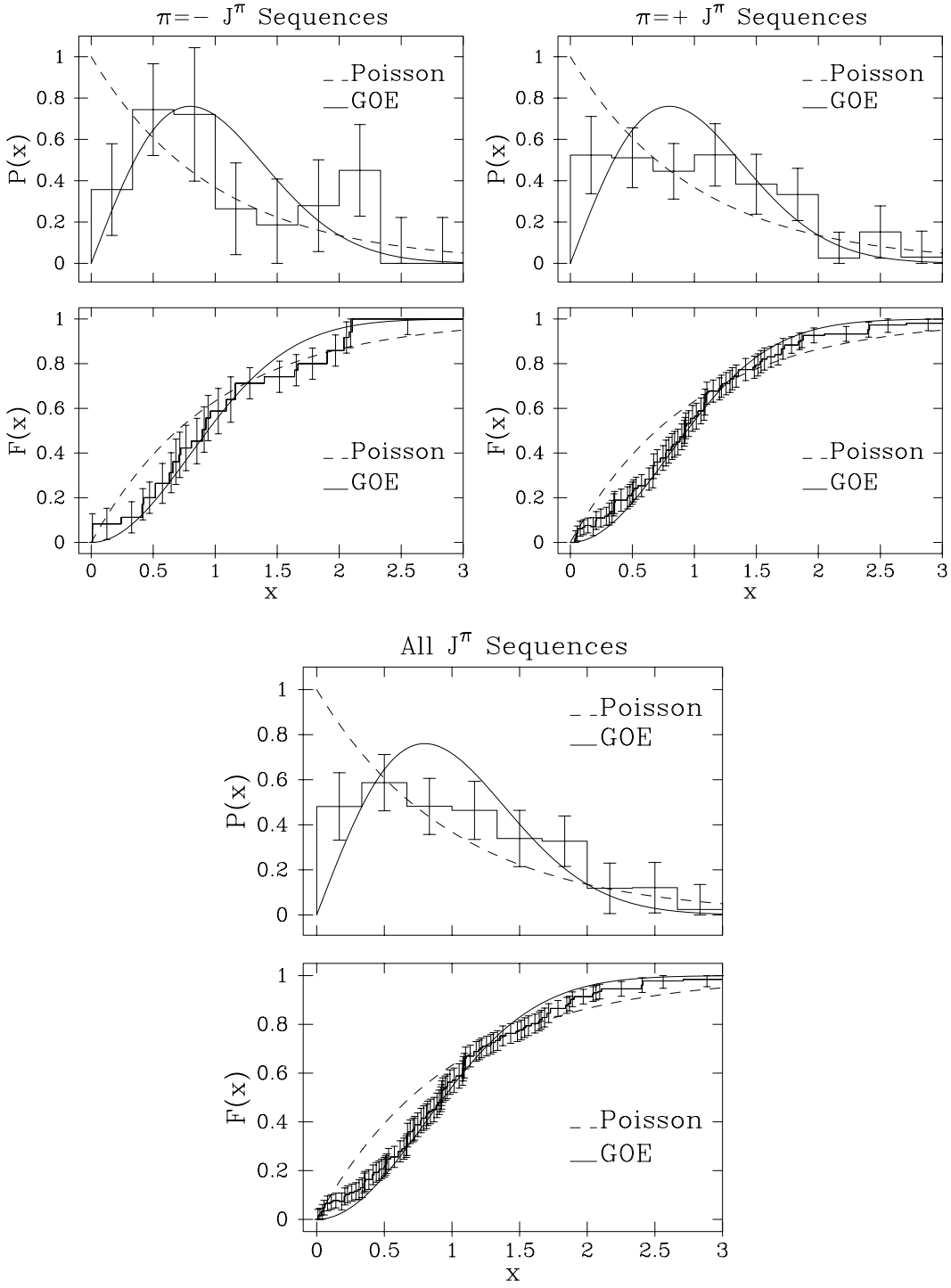

Figure 7.2: The positive parity J^π sequences (top left), negative parity J^π sequences (top right), and all parity J^π sequences (bottom) are shown.

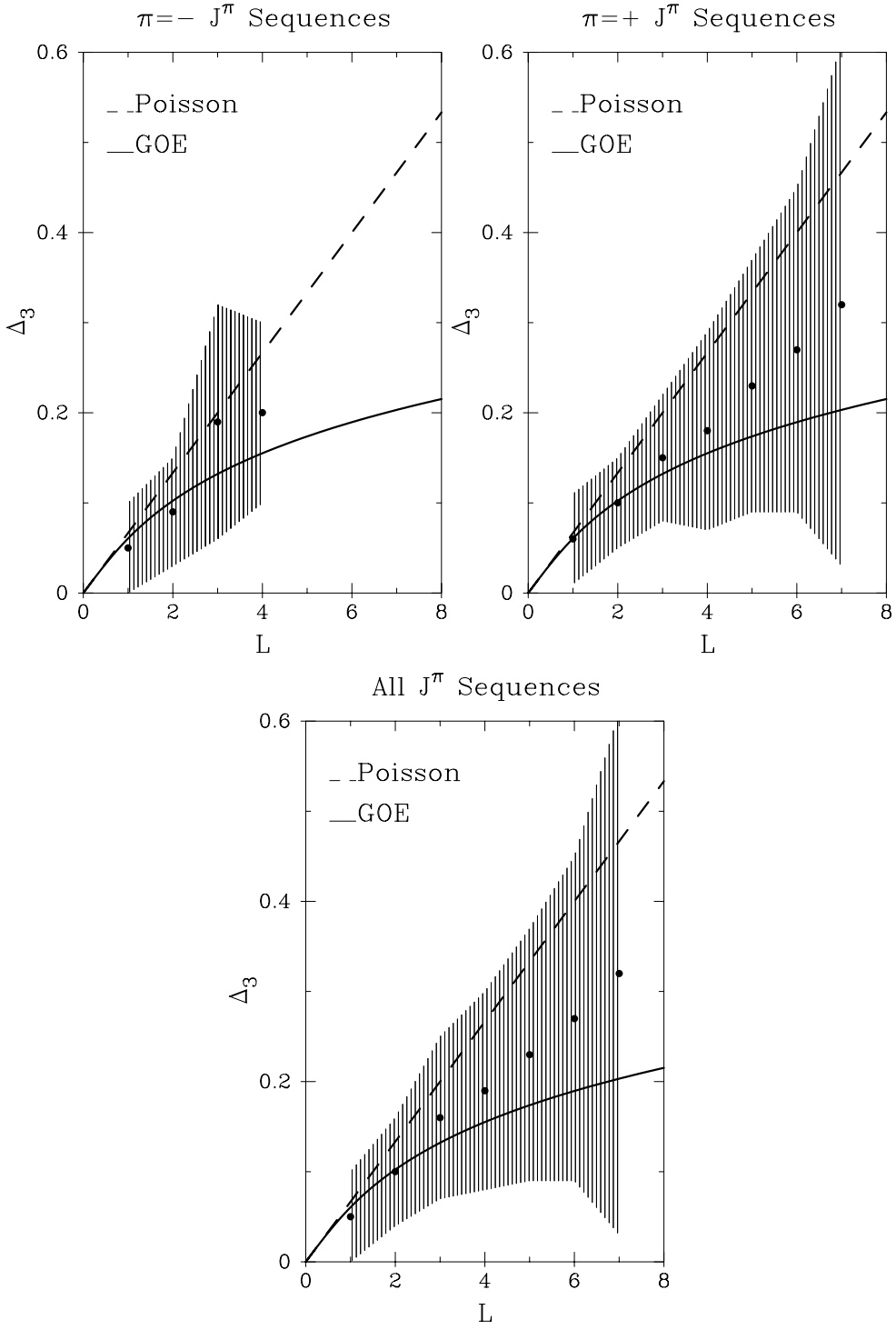

shown in Figure 7.4. The negative parity sequences have only three points: $L = 1$ lies on the GOE curve, $L = 2$ lies barely above the Poisson curve, and $L = 3$ lies midway between the two curves, but closer to the GOE curve. The positive parity sequences agree with the GOE curve. It is possible that the points at $L \geq 4$ are forming an upward trend away from the GOE curve. When all $J^\pi;T$ sequences are included, the data are almost indistinguishable from the positive parity $J^\pi;T$ sequences. The $L = 1$ point is slightly higher, making the data appear slightly higher than the GOE curve.

Another important comparison is between the distributions for all J^π sequences and for all $J^\pi;T$ sequences with $T = 0$. The NNSD for all J^π sequences (bottom plot of Figure 7.1) and the NNSD for all $J^\pi;T$ sequences with $T = 0$ (bottom plot of Figure 7.3) are very similar. In the $x < 1$ region, the amount the data are above the GOE curve is more pronounced in the $J^\pi;T$ sequences with $T = 0$. In the $x \approx 2$ region, the amount the data are below the GOE curve is more pronounced in the J^π sequences. The Δ_3 statistic for all J^π sequences (bottom plot of Figure 7.2) and the Δ_3 statistic for all $J^\pi;T$ sequences with $T = 0$ (bottom plot of Figure 7.4) are not as similar as the corresponding NNSD plots. For $L < 3$, there is good agreement with the GOE curve for both sets of sequences. However, for $L \geq 3$, the data for the J^π sequences lie midway between the GOE and Poisson curves, while the data for the $J^\pi;T$ sequences with $T = 0$ are in agreement, although slightly above the GOE curve.

The fit parameters for each of the statistical functions provide a more quantitative way to compare the sequences. The fit parameters are listed in Table 7.3. The ω parameter for the NNSD and the μ parameter for the Dyson-Mehta Δ_3 statistic are defined in Section 2.1.3. A value of unity for ω or μ corresponds to a GOE spectrum, and a value of zero corresponds to a Poisson spectrum. The ω parameters for all $J^\pi;T$ sequences and for all J^π sequences are in good agreement with one another, within one-fifth of the standard deviation for $P(x)$ and within one-half of the standard deviation for $F(x)$. The μ parameters for the all $J^\pi;T$ sequences and for all J^π sequences are also in good agreement with one another, within one-fifth of the standard deviation. The quantitative differences for

Figure 7.3: The positive parity $J^\pi;T$ sequences with $T = 0$ (top left), negative parity $J^\pi;T$ sequences with $T = 0$ (top right), and all parity $J^\pi;T$ sequences with $T = 0$ (bottom) are shown.

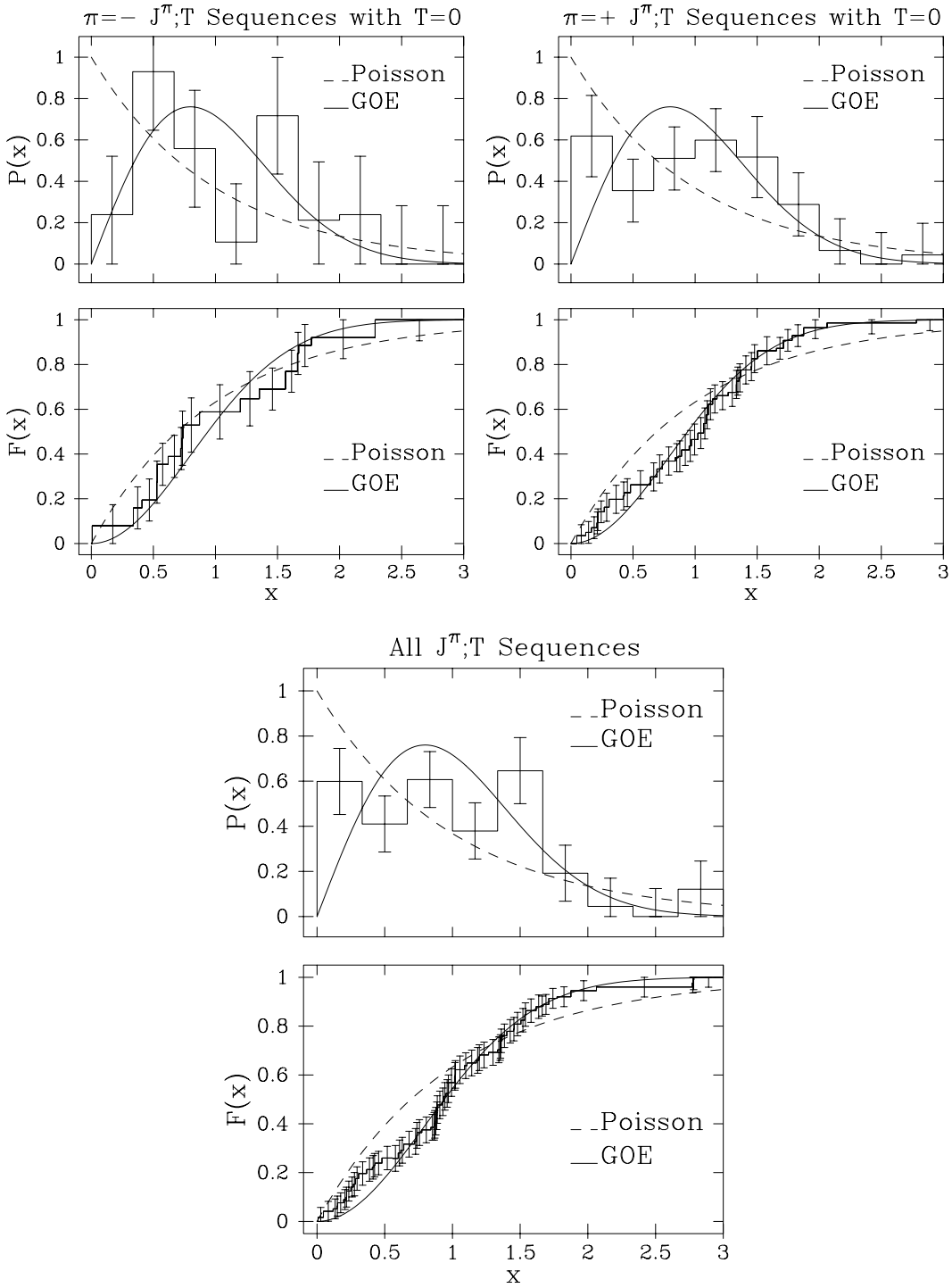

Figure 7.4: The positive parity $J^\pi;T$ sequences with $T = 0$ (top left), negative parity $J^\pi;T$ sequences with $T = 0$ (top right), and all parity $J^\pi;T$ sequences with $T = 0$ (bottom) are shown.

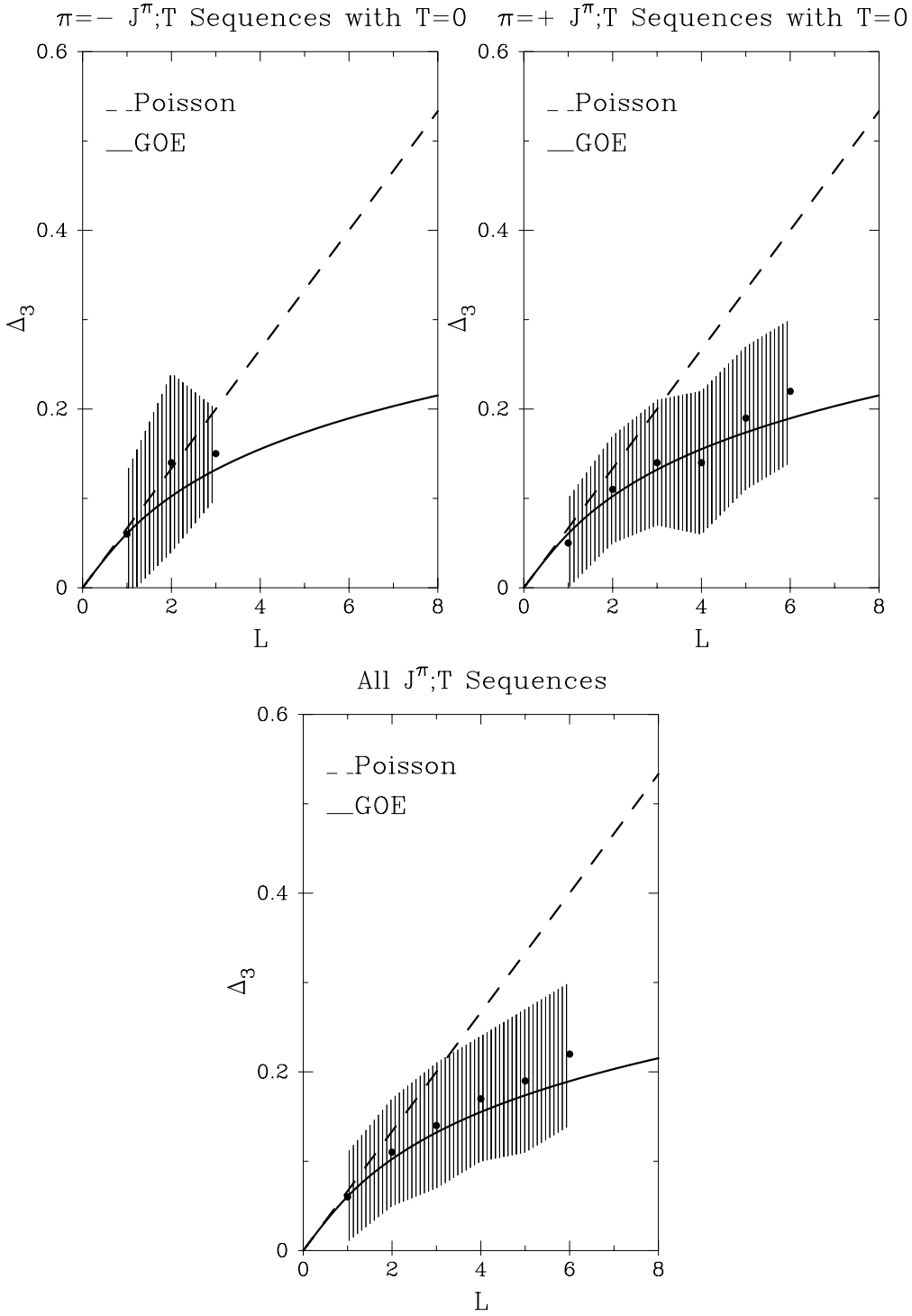

Table 7.3: Fit Parameters for Fluctuation Properties.

Sequence		$\omega \pm \sigma_\omega$ $P(x)$	$\omega \pm \sigma_\omega$ $F(x)$	$\mu \pm \sigma_\mu$ $i\Delta_3$
J^π	$\pi = -$	0.51 ± 0.26	0.56 ± 0.39	$0.74^{+0.79}_{-0.74}$
J^π	$\pi = +$	0.40 ± 0.20	0.60 ± 0.25	$0.77^{+0.50}_{-0.77}$
J^π		0.43 ± 0.17	0.59 ± 0.21	$0.75^{+0.51}_{-0.75}$
$J^\pi;T$	$\pi = -,\ T = 0$	0.62 ± 0.32	0.51 ± 0.48	$0.73^{+0.80}_{-0.73}$
$J^\pi;T$	$\pi = +,\ T = 0$	0.46 ± 0.27	0.85 ± 0.41	$0.92^{+0.33}_{-0.38}$
$J^\pi;T$		0.41 ± 0.19	0.68 ± 0.30	$0.89^{+0.33}_{-0.38}$

$F(x)$ and Δ_3 are in agreement with the obsevations made on the distributions: the $J^\pi;T$ sequences are in closer agreement to GOE than the J^π sequences.

There is a slight disagreement between the J^π sequences and the $J^\pi;T$ sequences with $T = 0$. Within one standard deviation, all J^π sequences and all $J^\pi;T$ sequences are consistent with the range of ω values for $F(x)$ for the ^{26}Al sequences, $0.45 - 0.59$ [Shr90]. Within one standard deviation, all results are consistent with μ values in the range $0.77 - 1.25$. The accepted range for μ values for the ^{26}Al sequences was $0.7 - 0.9$ [Shr90], also in agreement with the present data.

Chapter 8

Summary

The research presented in this dissertation was motivated by the results of a study of fluctuation properties of the ^{26}Al nucleus. These results indicated a need to test the effects of symmetry breaking on the statistical distributions in more nuclei. The ^{30}P nucleus was chosen as the next candidate for such a study. These tests require purity and completeness of the spectroscopic data. Numerous experiments have been performed, with the common goal of achieving pure and complete level spectroscopy for ^{30}P. High-resolution elastic scattering measurements in the energy range $E_p = 0.94 - 3.3$ MeV [Nel83, Fra91] and high-resolution (p,γ) measurements in the energy range $E_p = 1.04 - 2.50$ MeV [Vav96, Wal96] were made to identify all levels and to assign quantum numbers J, π, and T. With ambiguities remaining after these measurements, it was decided that a measurement capable of improving the quantum number assignments was necessary.

Angular distributions were measured using the high-resolution proton beam at the HRL and the CSS system for more than thirty ^{29}Si(p,γ) resonances. Comparison to calculated angular distribution coefficients allowed determination of a number of previously ambiguous J^π assignments. In approximately 20 states, angular distributions measurements were used to aid in J^π assignments. Mixing ratios were also measured, and used to compare the strengths of transitions to RUL's to aid in determining T assignments. In approximately 25 states, RUL analysis was used to aid in J, π, or T assignments. Remaining ambigui-

ties were eliminated by comparing levels to shell model calculations and to parent states in ^{30}Si. Approximately 50 assignments of $J^{\pi};T$ were aided by comparison to shell model calculations, parent states in ^{30}Si, or both. A total of approximately 65 assignments were made in ^{30}P between 0 and 8015 keV as a result of this work.

Ten sequences were used in the statistical analysis of ^{30}P. Results were found to be between GOE and Poisson. There was a little dependence on isospin. Within one standard deviation, quantitative measures of the statistical distributions were independent of isospin and in agreement with ^{26}Al results [Shr90].

Appendix A

Angular Distribution Coefficient Expressions

The a_2, a_4, and a_6 expressions used in this work are listed in this appendix. In all cases, $a_4 = 0$ and $a_6 = 0$ unless stated otherwise. The transitions are grouped into sections according to their initial state J_i^π, and listed within each section as a transition from initial state J_i^π to increasing final state values of J_f^π. The proton mixing ratio δ_p and γ-ray mixing ratio δ_γ, as defined in Section 3.2, are given when appropriate.

Table A.1: Initial State $J^\pi = 1^-$, $\delta_p \equiv \frac{g_{11}}{g_{01}}$

$1^- \rightarrow 0^-$		$a_2 = -\frac{\left(1-\frac{1}{2}\delta_p^2\right)}{\left(1+\delta_p^2\right)}$
$1^- \rightarrow 0^+$		$a_2 = -\frac{\left(1-\frac{1}{2}\delta_p^2\right)}{\left(1+\delta_p^2\right)}$
$1^- \rightarrow 1^-$	$\delta_\gamma \equiv \frac{g_{E2}}{g_{M1}}$	$a_2 = \frac{1}{2}\frac{\left(1-6\delta_\gamma+\delta_\gamma^2\right)\left(1-\frac{1}{2}\delta_p^2\right)}{\left(1+\delta_\gamma^2\right)\left(1+\delta_p^2\right)}$
$1^- \rightarrow 1^+$		$a_2 = \frac{1}{2}\frac{\left(1-\frac{1}{2}\delta_p^2\right)}{\left(1+\delta_p^2\right)}$

Table A.1*(continued)*

$1^- \to 2^-$	$\delta_\gamma \equiv \frac{g_{E2}}{g_{M1}}$	$a_2 = -\frac{1}{10}\frac{\left(1-6\sqrt{5}\delta_\gamma+5\delta_\gamma^2\right)\left(1-\frac{1}{2}\delta_p^2\right)}{\left(1+\delta_\gamma^2\right)\left(1+\delta_p^2\right)}$
$1^- \to 2^+$		$a_2 = -\frac{1}{10}\frac{\left(1-\frac{1}{2}\delta_p^2\right)}{\left(1+\delta_p^2\right)}$
$1^- \to 3^-$		$a_2 = \frac{1}{7}\frac{\left(1-\frac{1}{2}\delta_p^2\right)}{\left(1+\delta_p^2\right)}$
$1^- \to 3^+$	$\delta_\gamma \equiv \frac{g_{E3}}{g_{M2}}$	$a_2 = \frac{4}{28}\frac{\left(1+2\sqrt{14}\delta_\gamma-\frac{21}{4}\delta_\gamma^2\right)\left(1-\frac{1}{2}\delta_p^2\right)}{\left(1+\delta_\gamma^2\right)(1+\delta_p^2)}$
$1^- \to 3^-$		$a_2 = \frac{1}{7}\frac{\left(1-\frac{1}{2}\delta_p^2\right)}{\left(1+\delta_p^2\right)}$
$1^- \to 4^+$		$a_2 = \frac{1}{4}\frac{\left(1-\frac{1}{2}\delta_p^2\right)}{\left(1+\delta_p^2\right)}$

Table A.2: Initial State $J^\pi = 1^+$, $\delta_p \equiv \frac{g_{12}}{g_{10}}$

$1^+ \to 0^-$		$a_2 = \frac{1}{2}\frac{2\sqrt{2}\cos(\xi_0-\xi_2)\delta_p-\delta_p^2}{\left(1+\delta_p^2\right)}$
$1^+ \to 0^+$		$a_2 = \frac{1}{2}\frac{2\sqrt{2}\cos(\xi_0-\xi_2)\delta_p-\delta_p^2}{\left(1+\delta_p^2\right)}$
$1^+ \to 1^-$		$a_2 = -\frac{1}{4}\frac{2\sqrt{2}\cos(\xi_0-\xi_2)\delta_p-\delta_p^2}{\left(1+\delta_p^2\right)}$
$1^+ \to 1^+$	$\delta_\gamma \equiv \frac{g_{E2}}{g_{M1}}$	$a_2 = -\frac{1}{4}\frac{\left(1-6\delta_\gamma+\delta_\gamma^2\right)\left(2\sqrt{2}\cos(\xi_0-\xi_2)\delta_p-\delta_p^2\right)}{\left(1+\delta_\gamma^2\right)\left(1+\delta_p^2\right)}$
$1^+ \to 2^-$		$a_2 = \frac{1}{20}\frac{2\sqrt{2}\cos(\xi_0-\xi_2)\delta_p-\delta_p^2}{\left(1+\delta_p^2\right)}$
$1^+ \to 2^+$	$\delta_\gamma \equiv \frac{g_{E2}}{g_{M1}}$	$a_2 = \frac{1}{20}\frac{\left(1-6\sqrt{5}\delta_\gamma+5\delta_\gamma^2\right)\left(2\sqrt{2}\cos(\xi_0-\xi_2)\delta_p-\delta_p^2\right)}{\left(1+\delta_\gamma^2\right)\left(1+\delta_p^2\right)}$
$1^+ \to 3^-$	$\delta_\gamma \equiv \frac{g_{E3}}{g_{M2}}$	$a_2 = -\frac{1}{14}\frac{\left(2\sqrt{2}\cos(\xi_0-\xi_2)\delta_p-\delta_p^2\right)\left(1+2\sqrt{14}\delta_\gamma-\frac{21}{4}\delta_\gamma^2\right)}{\left(1+\delta_\gamma^2\right)\left(1+\delta_p^2\right)}$
$1^+ \to 3^+$		$a_2 = -\frac{1}{14}\frac{2\sqrt{2}\cos(\xi_0-\xi_2)\delta_p-\delta_p^2}{\left(1+\delta_p^2\right)}$
$1^+ \to 4^-$		$a_2 = -\frac{1}{8}\frac{2\sqrt{2}\cos(\xi_0-\xi_2)\delta_p-\delta_p^2}{\left(1+\delta_p^2\right)}$

Table A.3: Initial State $J^\pi = 2^-$, $\delta_p \equiv \frac{g_{13}}{g_{11}}$

$2^- \to 0^-$		$a_2 = \frac{1}{2}\frac{\left(1-\frac{2}{7}\sqrt{6}\cos(\xi_1-\xi_3)\delta_p+\frac{8}{7}\delta_p^2\right)}{\left(1+\delta_p^2\right)}$
		$a_4 = \frac{4}{7}\frac{2\sqrt{6}\cos(\xi_1-\xi_3)\delta_p-\delta_p^2}{\left(1+\delta_p^2\right)}$
$2^- \to 0^+$		$a_2 = \frac{1}{2}\frac{\left(1-\frac{2}{7}\sqrt{6}\cos(\xi_1-\xi_3)\delta_p+\frac{8}{7}\delta_p^2\right)}{\left(1+\delta_p^2\right)}$
		$a_4 = \frac{4}{7}\frac{2\sqrt{6}\cos(\xi_1-\xi_3)\delta_p-\delta_p^2}{\left(1+\delta_p^2\right)}$
$2^- \to 1^-$	$\delta_\gamma \equiv \frac{g_{E2}}{g_{M1}}$	$a_2 = -\frac{7}{20}\frac{\left(1+2\sqrt{5}\delta_\gamma-\frac{5}{7}\delta_\gamma^2\right)\left(1-\frac{2}{7}\sqrt{6}\cos(\xi_1-\xi_3)\delta_p+\frac{8}{7}\delta_p^2\right)}{\left(1+\delta_\gamma^2\right)\left(1+\delta_p^2\right)}$
		$a_4 = -\frac{8}{21}\frac{\delta_\gamma^2\left(2\sqrt{6}\cos(\xi_1-\xi_3)\delta_p-\delta_p^2\right)}{\left(1+\delta_\gamma^2\right)\left(1+\delta_p^2\right)}$
$2^- \to 1^+$		$a_2 = -\frac{7}{20}\frac{\left(1-\frac{2}{7}\sqrt{6}\cos(\xi_1-\xi_3)\delta_p+\frac{8}{7}\delta_p^2\right)}{\left(1+\delta_p^2\right)}$
$2^- \to 2^-$	$\delta_\gamma \equiv \frac{g_{E2}}{g_{M1}}$	$a_2 = \frac{7}{20}\frac{\left(1-\frac{2}{7}\sqrt{105}\delta_\gamma-\frac{15}{49}\delta_\gamma^2\right)\left(1-\frac{2}{7}\sqrt{6}\cos(\xi_1-\xi_3)\delta_p+\frac{8}{7}\delta_p^2\right)}{\left(1+\delta_\gamma^2\right)\left(1+\delta_p^2\right)}$
		$a_4 = \frac{8}{49}\frac{\delta_\gamma^2\left(2\sqrt{6}\cos(\xi_1-\xi_3)\delta_p-\delta_p^2\right)}{\left(1+\delta_\gamma^2\right)\left(1+\delta_p^2\right)}$
$2^- \to 2^+$		$a_2 = \frac{7}{20}\frac{\left(1-\frac{2}{7}\sqrt{6}\cos(\xi_1-\xi_3)\delta_p+\frac{8}{7}\delta_p^2\right)}{\left(1+\delta_p^2\right)}$
$2^- \to 3^-$	$\delta_\gamma \equiv \frac{g_{E2}}{g_{M1}}$	$a_2 = -\frac{1}{10}\frac{\left(1-2\sqrt{30}\delta_\gamma+\frac{20}{7}\delta_\gamma^2\right)\left(1-\frac{2}{7}\sqrt{6}\cos(\xi_1-\xi_3)\delta_p+\frac{8}{7}\delta_p^2\right)}{\left(1+\delta_\gamma^2\right)\left(1+\delta_p^2\right)}$
		$a_4 = -\frac{2}{49}\frac{\delta_\gamma^2\left(2\sqrt{6}\cos(\xi_1-\xi_3)\delta_p-\delta_p^2\right)}{\left(1+\delta_\gamma^2\right)\left(1+\delta_p^2\right)}$
$2^- \to 3^+$		$a_2 = -\frac{1}{10}\frac{\left(1-\frac{2}{7}\sqrt{6}\cos(\xi_1-\xi_3)\delta_p+\frac{8}{7}\delta_p^2\right)}{\left(1+\delta_p^2\right)}$
$2^- \to 4^-$		$a_2 = \frac{1}{7}\frac{\left(1-\frac{2}{7}\sqrt{6}\cos(\xi_1-\xi_3)\delta_p+\frac{8}{7}\delta_p^2\right)}{\left(1+\delta_p^2\right)}$
		$a_4 = \frac{2}{441}\frac{2\sqrt{6}\cos(\xi_1-\xi_3)\delta_p-\delta_p^2}{\left(1+\delta_p^2\right)}$
$2^- \to 4^+$	$\delta_\gamma \equiv \frac{g_{E3}}{g_{M2}}$	$a_2 = \frac{1}{7}\frac{\left(1+\sqrt{35}\delta_\gamma-\frac{21}{8}\delta_\gamma^2\right)\left(1-\frac{2}{7}\sqrt{6}\cos(\xi_1-\xi_3)\delta_p+\frac{8}{7}\delta_p^2\right)}{\left(1+\delta_\gamma^2\right)\left(1+\delta_p^2\right)}$
		$a_4 = \frac{2}{441}\frac{\left(1-\frac{5}{2}\delta_\gamma+\frac{7}{2}\delta_\gamma^2\right)\left(2\sqrt{6}\cos(\xi_1-\xi_3)\delta_p-\delta_p^2\right)}{\left(1+\delta_\gamma^2\right)\left(1+\delta_p^2\right)}$

Table A.4: Initial State $J^\pi = 2^+$, $\delta_p \equiv \frac{g_{12}}{g_{02}}$

$2^+ \to 0^-$		$a_2 = \frac{5}{7}\frac{\left(1+\frac{1}{2}\delta_p^2\right)}{\left(1+\delta_p^2\right)}$
		$a_4 = -\frac{12}{7}\frac{\left(1-\frac{2}{3}\delta_p^2\right)}{\left(1+\delta_p^2\right)}$
$2^+ \to 0^+$		$a_2 = \frac{5}{7}\frac{\left(1+\frac{1}{2}\delta_p^2\right)}{\left(1+\delta_p^2\right)}$
		$a_4 = -\frac{12}{7}\frac{\left(1-\frac{2}{3}\delta_p^2\right)}{\left(1+\delta_p^2\right)}$
$2^+ \to 1^-$		$a_2 = -\frac{1}{2}\frac{\left(1+\frac{1}{2}\delta_p^2\right)}{\left(1+\delta_p^2\right)}$
$2^+ \to 1^+$	$\delta_\gamma \equiv \frac{g_{E2}}{g_{M1}}$	$a_2 = -\frac{1}{2}\frac{\left(1+2\sqrt{5}\delta_\gamma-\frac{5}{7}\delta_\gamma^2\right)\left(1+\frac{1}{2}\delta_p^2\right)}{\left(1+\delta_\gamma^2\right)\left(1+\delta_p^2\right)}$
		$a_4 = \frac{8}{7}\frac{\delta_\gamma^2\left(1-\frac{2}{3}\delta_p^2\right)}{\left(1+\delta_\gamma^2\right)\left(1+\delta_p^2\right)}$
$2^+ \to 2^-$		$a_2 = \frac{1}{2}\frac{\left(1+\frac{1}{2}\delta_p^2\right)}{\left(1+\delta_p^2\right)}$
$2^+ \to 2^+$	$\delta_\gamma \equiv \frac{g_{E2}}{g_{M1}}$	$a_2 = \frac{1}{2}\frac{\left(1-\frac{2}{7}\sqrt{105}\delta_\gamma-\frac{15}{49}\delta_\gamma^2\right)\left(1+\frac{1}{2}\delta_p^2\right)}{\left(1+\delta_\gamma^2\right)\left(1+\delta_p^2\right)}$
		$a_4 = -\frac{24}{49}\frac{\delta_\gamma^2\left(1-\frac{2}{3}\delta_p^2\right)}{\left(1+\delta_\gamma^2\right)\left(1+\delta_p^2\right)}$
$2^+ \to 3^-$		$a_2 = -\frac{1}{7}\frac{\left(1+\frac{1}{2}\delta_p^2\right)}{\left(1+\delta_p^2\right)}$
$2^+ \to 3^+$	$\delta_\gamma \equiv \frac{g_{E2}}{g_{M1}}$	$a_2 = -\frac{1}{7}\frac{\left(1-2\sqrt{30}\delta_\gamma+\frac{20}{7}\delta_\gamma^2\right)\left(1+\frac{1}{2}\delta_p^2\right)}{\left(1+\delta_\gamma^2\right)\left(1+\delta_p^2\right)}$
		$a_4 = \frac{6}{49}\frac{\delta_\gamma^2\left(1-\frac{2}{3}\delta_p^2\right)}{\left(1+\delta_\gamma^2\right)\left(1+\delta_p^2\right)}$
$2^+ \to 4^-$	$\delta_\gamma \equiv \frac{g_{E3}}{g_{M2}}$	$a_2 = \frac{10}{49}\frac{\left(1+\sqrt{35}\delta_\gamma-\frac{21}{8}\delta_\gamma^2\right)\left(1+\frac{1}{2}\delta_p^2\right)}{\left(1+\delta_\gamma^2\right)\left(1+\delta_p^2\right)}$
		$a_4 = -\frac{2}{147}\frac{\left(1-\frac{2}{3}\delta_p^2\right)\left(1-\frac{5}{2}\sqrt{35}+\frac{7}{2}\right)}{\left(1+\delta_\gamma^2\right)\left(1+\delta_p^2\right)}$
$2^+ \to 4^+$		$a_2 = \frac{10}{49}\frac{\left(1+\frac{1}{2}\delta_p^2\right)}{\left(1+\delta_p^2\right)}$
		$a_4 = -\frac{2}{147}\frac{\left(1-\frac{2}{3}\delta_p^2\right)}{\left(1+\delta_p^2\right)}$

Table A.5: Initial State $J^\pi = 3^-$, $\delta_p \equiv \frac{g_{13}}{g_{03}}$

$3^- \to 0^+$		$a_2 = \frac{\left(1+\frac{3}{4}\delta_p^2\right)}{\left(1+\delta_p^2\right)}$
		$a_4 = \frac{3}{11}\frac{\left(1+\frac{1}{6}\delta_p^2\right)}{\left(1+\delta_p^2\right)}$
		$a_6 = -\frac{25}{11}\frac{\left(1-\frac{3}{4}\delta_p^2\right)}{\left(1+\delta_p^2\right)}$
$3^- \to 1^-$		$a_2 = \frac{4}{7}\frac{\left(1+\frac{3}{4}\delta_p^2\right)}{\left(1+\delta_p^2\right)}$
		$a_4 = -\frac{4}{7}\frac{\left(1+\frac{1}{6}\delta_p^2\right)}{\left(1+\delta_p^2\right)}$
$3^- \to 1^+$	$\delta_\gamma \equiv \frac{g_{E3}}{g_{M2}}$	$a_2 = \frac{4}{7}\frac{\left(1-\frac{1}{2}\sqrt{14}\delta_\gamma+\frac{21}{16}\delta_\gamma^2\right)\left(1+\frac{3}{4}\delta_p^2\right)}{\left(1+\delta_\gamma^2\right)\left(1+\delta_p^2\right)}$
		$a_4 = -\frac{4}{7}\frac{\left(1+\frac{5}{4}\sqrt{14}\delta_\gamma-\frac{7}{88}\delta_\gamma^2\right)\left(1+\frac{1}{6}\delta_p^2\right)}{\left(1+\delta_\gamma^2\right)\left(1+\delta_p^2\right)}$
		$a_6 = \frac{75}{44}\frac{\delta_\gamma^2\left(1-\frac{3}{4}\delta_p^2\right)}{\left(1+\delta_\gamma^2\right)\left(1+\delta_p^2\right)}$
$3^- \to 2^-$	$\delta_\gamma \equiv \frac{g_{E2}}{g_{M1}}$	$a_2 = -\frac{2}{5}\frac{\left(1+\sqrt{30}\delta_\gamma-\frac{5}{14}\delta_\gamma^2\right)\left(1+\frac{3}{4}\delta_p^2\right)}{\left(1+\delta_\gamma^2\right)\left(1+\delta_p^2\right)}$
		$a_4 = \frac{6}{7}\frac{\delta_\gamma^2\left(1+\frac{1}{6}\delta_p^2\right)}{\left(1+\delta_\gamma^2\right)\left(1+\delta_p^2\right)}$
$3^- \to 2^+$		$a_2 = -\frac{2}{5}\frac{\left(1+\frac{3}{4}\delta_p^2\right)}{\left(1+\delta_p^2\right)}$
$3^- \to 3^-$	$\delta_\gamma \equiv \frac{g_{E2}}{g_{M1}}$	$a_2 = \frac{1}{2}\frac{\left(1-2\delta_\gamma-\frac{11}{21}\delta_\gamma^2\right)\left(1+\frac{3}{4}\delta_p^2\right)}{\left(1+\delta_\gamma^2\right)\left(1+\delta_p^2\right)}$
		$a_4 = -\frac{4}{7}\frac{\delta_\gamma^2\left(1+\frac{1}{6}\delta_p^2\right)}{\left(1+\delta_\gamma^2\right)\left(1+\delta_p^2\right)}$
$3^- \to 3^+$		$a_2 = \frac{1}{2}\frac{\left(1+\frac{3}{4}\delta_p^2\right)}{\left(1+\delta_p^2\right)}$
$3^- \to 4^-$	$\delta_\gamma \equiv \frac{g_{E2}}{g_{M1}}$	$a_2 = -\frac{1}{6}\frac{\left(1-10\delta_\gamma+\frac{15}{7}\delta_\gamma^2\right)\left(1+\frac{3}{4}\delta_p^2\right)}{\left(1+\delta_\gamma^2\right)\left(1+\delta_p^2\right)}$
		$a_4 = \frac{4}{21}\frac{\delta_\gamma^2\left(1+\frac{1}{6}\delta_p^2\right)}{\left(1+\delta_\gamma^2\right)\left(1+\delta_p^2\right)}$
$3^- \to 4^+$		$a_2 = -\frac{1}{6}\frac{\left(1+\frac{3}{4}\delta_p^2\right)}{\left(1+\delta_p^2\right)}$

Table A.5*(continued)*

$3^- \rightarrow 5^+$	$\delta_\gamma \equiv \frac{g_{E3}}{g_{M2}}$	$a_2 = \frac{5}{21}\frac{\left(1+2\sqrt{7}\delta_\gamma-\frac{7}{4}\delta_\gamma^2\right)\left(1+\frac{3}{4}\delta_p^2\right)}{\left(1+\delta_\gamma^2\right)\left(1+\delta_p^2\right)}$
		$a_4 = -\frac{2}{77}\frac{\left(1-5\sqrt{7}\delta_\gamma+\frac{119}{44}\delta_\gamma^2\right)\left(1+\frac{1}{6}\delta_p^2\right)}{\left(1+\delta_\gamma^2\right)\left(1+\delta_p^2\right)}$
		$a_6 = -\frac{25}{1452}\frac{\delta_\gamma^2\left(1-\frac{3}{4}\delta_p^2\right)}{\left(1+\delta_\gamma^2\right)\left(1+\delta_p^2\right)}$

Table A.6: Initial State $J^\pi = 3^+$, $\delta_p \equiv \frac{g_{14}}{g_{12}}$

$3^+ \to 0^-$		$a_2 = \frac{6}{7}\frac{\left(1-\frac{2}{3}\sqrt{3}\cos(\xi_2=\xi_4)\delta_p+\frac{25}{24}\delta_p^2\right)}{\left(1+\delta_p^2\right)}$
		$a_4 = \frac{1}{7}\frac{\left(1-\frac{10}{11}\sqrt{3}\cos(\xi_2-\xi_4)\delta_p+\frac{27}{22}\delta_p^2\right)}{\left(1+\delta_p^2\right)}$
		$a_6 = \frac{25}{44}\frac{\delta_p\left(4\sqrt{3}\cos(\xi_2=\xi_4)-\delta_p\right)}{\left(1+\delta_p^2\right)}$
$3^+ \to 1^-$	$\delta_\gamma \equiv \frac{g_{E3}}{g_{M2}}$	$a_2 = \frac{24}{49}\frac{\left(1-\frac{1}{2}\sqrt{14}\delta_\gamma+\frac{21}{16}\delta_\gamma^2\right)\left(1-\frac{1}{6}\sqrt{3}\cos(\xi_2-\xi_4)\delta_p+\frac{25}{24}\delta_p^2\right)}{\left(1+\delta_\gamma^2\right)\left(1+\delta_p^2\right)}$
		$a_4 = -\frac{44}{147}\frac{\left(1+\frac{5}{4}\sqrt{14}\cos(\xi_2-\xi_4)\delta_\gamma-\frac{7}{88}\delta_\gamma^2\right)\left(1-\frac{10}{11}\sqrt{3}\cos(\xi_2-\xi_4)\delta_p+\frac{27}{22}\delta_p^2\right)}{\left(1+\delta_\gamma^2\right)\left(1+\delta_p^2\right)}$
		$a_6 = \frac{75}{176}\frac{\delta_\gamma^2\delta_p\left(\delta_p-4\sqrt{3}\cos(\xi_2-\xi_4)\right)}{\left(1+\delta_\gamma^2\right)\left(1+\delta_p^2\right)}$
$3^+ \to 1^+$		$a_2 = \frac{24}{49}\frac{\left(1-\frac{1}{6}\sqrt{3}\cos(\xi_2-\xi_4)\delta_p+\frac{25}{24}\delta_p^2\right)}{\left(1+\delta_p^2\right)}$
		$a_4 = -\frac{44}{147}\frac{\left(1-\frac{10}{11}\sqrt{3}\cos(\xi_2-\xi_4)\delta_p+\frac{27}{22}\delta_p^2\right)}{\left(1+\delta_p^2\right)}$
$3^+ \to 2^-$		$a_2 = -\frac{12}{35}\frac{\left(1-\frac{1}{6}\sqrt{3}\cos(\xi_2-\xi_4)\delta_p+\frac{25}{24}\delta_p^2\right)}{\left(1+\delta_p^2\right)}$
$3^+ \to 2^+$	$\delta_\gamma \equiv \frac{g_{E2}}{g_{M1}}$	$a_2 = -\frac{12}{35}\frac{\left(1+\sqrt{30}\delta_\gamma-\frac{5}{14}\delta_\gamma^2\right)\left(1-\frac{1}{6}\sqrt{3}\cos(\xi_2-\xi_4)\delta_p+\frac{25}{24}\delta_p^2\right)}{\left(1+\delta_\gamma^2\right)\left(1+\delta_p^2\right)}$
		$a_4 = \frac{22}{49}\frac{\delta_\gamma^2\left(1-\frac{10}{11}\sqrt{3}\cos(\xi_2-\xi_4)\delta_p+\frac{27}{22}\delta_p^2\right)}{\left(1+\delta_\gamma^2\right)\left(1+\delta_p^2\right)}$
$3^+ \to 3^-$		$a_2 = \frac{3}{7}\frac{\left(1-\frac{1}{6}\sqrt{3}\cos(\xi_2-\xi_4)\delta_p+\frac{25}{24}\delta_p^2\right)}{\left(1+\delta_p^2\right)}$
$3^+ \to 3^+$	$\delta_\gamma \equiv \frac{g_{E2}}{g_{M1}}$	$a_2 = \frac{3}{7}\frac{\left(1-2\delta_\gamma-\frac{11}{21}\delta_\gamma^2\right)\left(1-\frac{1}{6}\sqrt{3}\cos(\xi_2-\xi_4)\delta_p+\frac{25}{24}\delta_p^2\right)}{\left(1+\delta_\gamma^2\right)\left(1+\delta_p^2\right)}$
		$a_4 = -\frac{44}{147}\frac{\delta_\gamma^2\left(1-\frac{10}{11}\sqrt{3}\cos(\xi_2-\xi_4)\delta_p+\frac{27}{22}\delta_p^2\right)}{\left(1+\delta_\gamma^2\right)\left(1+\delta_p^2\right)}$
$3^+ \to 4^-$		$a_2 = -\frac{1}{7}\frac{\left(1-\frac{1}{6}\sqrt{3}\cos(\xi_2-\xi_4)\delta_p+\frac{25}{24}\delta_p^2\right)}{\left(1+\delta_p^2\right)}$
$3^+ \to 4^+$	$\delta_\gamma \equiv \frac{g_{E2}}{g_{M1}}$	$a_2 = -\frac{1}{7}\frac{\left(1-10\delta_\gamma+\frac{15}{7}\delta_\gamma^2\right)\left(1-\frac{1}{6}\sqrt{3}\cos(\xi_2-\xi_4)\delta_p+\frac{25}{24}\delta_p^2\right)}{\left(1+\delta_\gamma^2\right)\left(1+\delta_p^2\right)}$
		$a_4 = \frac{44}{441}\frac{\delta_\gamma^2\left(1-\frac{10}{11}\sqrt{3}\cos(\xi_2-\xi_4)\delta_p+\frac{27}{22}\delta_p^2\right)}{\left(1+\delta_\gamma^2\right)\left(1+\delta_p^2\right)}$

Table A.6*(continued)*

$3^+ \rightarrow 5^+$	$a_2 = \frac{10}{49}\frac{\left(1-\frac{1}{6}\sqrt{3}\cos(\xi_2-\xi_4)\delta_p+\frac{25}{24}\delta_p^2\right)}{\left(1+\delta_p^2\right)}$
	$a_4 = -\frac{2}{147}\frac{\left(1-\frac{10}{11}\sqrt{3}\cos(\xi_2-\xi_4)\delta_p+\frac{27}{22}\delta_p^2\right)}{\left(1+\delta_p^2\right)}$

Table A.7: Initial State $J^\pi = 4^-$

$4^- \rightarrow 1^+$		$a_2 = \frac{275}{336}$
		$a_4 = \frac{39}{308}$
		$a_6 = \frac{-125}{528}$
$4^- \rightarrow 2^-$		$a_2 = \frac{275}{588}$
		$a_4 = -\frac{13}{49}$
$4^- \rightarrow 2^+$	$\delta_\gamma \equiv \frac{g_{E3}}{g_{M2}}$	$a_2 = -\frac{275}{588}\frac{\left(1-\frac{2}{5}\sqrt{35}\delta_\gamma+\frac{21}{20}\delta_\gamma^2\right)}{\left(1+\delta_\gamma^2\right)}$
		$a_4 = -\frac{13}{49}\frac{\left(1+\sqrt{35}\delta_\gamma+\frac{7}{44}\delta_\gamma^2\right)}{\left(1+\delta_\gamma^2\right)}$
		$a_6 = \frac{75}{176}\frac{\delta_\gamma^2}{\left(1+\delta_\gamma^2\right)}$
$4^- \rightarrow 3^-$	$\delta_\gamma \equiv \frac{g_{E2}}{g_{M1}}$	$a_2 = -\frac{55}{168}\frac{\left(1+6\delta_\gamma-\frac{1}{7}\delta_\gamma^2\right)}{\left(1+\delta_\gamma^2\right)}$
		$a_4 = \frac{26}{49}\frac{\delta_\gamma^2}{\left(1+\delta_\gamma^2\right)}$
$4^- \rightarrow 3^+$		$a_2 = -\frac{55}{168}$
$4^- \rightarrow 4^-$	$\delta_\gamma \equiv \frac{g_{E2}}{g_{M1}}$	$a_2 = \frac{11}{24}\frac{\left(1-\frac{42}{539}\sqrt{385}\delta_\gamma-\frac{325}{539}\delta_\gamma^2\right)}{\left(1+\delta_\gamma^2\right)}$
		$a_4 = -\frac{234}{539}\frac{\delta_\gamma^2}{\left(1+\delta_\gamma^2\right)}$
$4^- \rightarrow 4^+$		$a_2 = \frac{11}{24}$
$4^- \rightarrow 5^+$		$a_2 = -\frac{1}{6}$

Table A.8: Initial State $J^\pi = 4^+$, $\delta_p \equiv \frac{g_{14}}{g_{04}}$

$4^+ \to 1^-$		$a_2 = \frac{25}{28}\frac{\left(1+\frac{17}{20}\delta_p^2\right)}{\left(1+\delta_p^2\right)}$
		$a_4 = \frac{27}{154}\frac{\left(1+\frac{1}{2}\delta_p^2\right)}{\left(1+\delta_p^2\right)}$
		$a_6 = -\frac{25}{44}\frac{\left(1-\frac{1}{20}\delta_p^2\right)}{\left(1+\delta_p^2\right)}$
$4^+ \to 2^-$	$\delta_\gamma \equiv \frac{g_{E3}}{g_{M2}}$	$a_2 = \frac{25}{49}\frac{\left(1-\frac{2}{5}\sqrt{35}\delta_\gamma+\frac{21}{20}\delta_\gamma^2\right)\left(1+\frac{17}{20}\delta_p^2\right)}{\left(1+\delta_\gamma^2\right)\left(1+\delta_p^2\right)}$
		$a_4 = -\frac{18}{49}\frac{\left(1+\sqrt{35}\delta_\gamma+\frac{7}{44}\delta_\gamma^2\right)\left(1+\frac{1}{2}\delta_p^2\right)}{\left(1+\delta_\gamma^2\right)\left(1+\delta_p^2\right)}$
		$a_6 = \frac{45}{44}\frac{\delta_\gamma^2\left(1-\frac{1}{20}\delta_p^2\right)}{\left(1+\delta_\gamma^2\right)\left(1+\delta_p^2\right)}$
$4^+ \to 2^+$		$a_2 = \frac{25}{49}\frac{\left(1+\frac{17}{20}\delta_p^2\right)}{\left(1+\delta_p^2\right)}$
		$a_4 = -\frac{18}{49}\frac{\left(1+\frac{1}{2}\delta_p^2\right)}{\left(1+\delta_p^2\right)}$
$4^+ \to 3^-$		$a_2 = -\frac{5}{14}\frac{\left(1+\frac{17}{20}\delta_p^2\right)}{\left(1+\delta_p^2\right)}$
$4^+ \to 3^+$	$\delta_\gamma \equiv \frac{g_{E2}}{g_{M1}}$	$a_2 = -\frac{5}{14}\frac{\left(1+6\delta_\gamma-\frac{1}{7}\delta_\gamma^2\right)\left(1+\frac{17}{20}\delta_p^2\right)}{\left(1+\delta_\gamma^2\right)\left(1+\delta_p^2\right)}$
		$a_4 = \frac{36}{49}\frac{\delta_\gamma^2\left(1+\frac{1}{2}\delta_p^2\right)}{\left(1+\delta_\gamma^2\right)\left(1+\delta_p^2\right)}$
$4^+ \to 4^-$		$a_2 = \frac{1}{2}\frac{\left(1+\frac{17}{20}\delta_p^2\right)}{\left(1+\delta_p^2\right)}$
$4^+ \to 4^+$	$\delta_\gamma \equiv \frac{g_{E2}}{g_{M1}}$	$a_2 = \frac{1}{2}\frac{\left(1-\frac{6}{77}\sqrt{385}\delta_\gamma-\frac{325}{539}\delta_\gamma^2\right)\left(1+\frac{17}{20}\delta_p^2\right)}{\left(1+\delta_\gamma^2\right)\left(1+\delta_p^2\right)}$
		$a_4 = -\frac{324}{539}\frac{\delta_\gamma^2\left(1+\frac{1}{2}\delta_p^2\right)}{\left(1+\delta_\gamma^2\right)\left(1+\delta_p^2\right)}$
$4^+ \to 5^+$	$\delta_\gamma \equiv \frac{g_{E2}}{g_{M1}}$	$a_2 = -\frac{2}{11}\frac{\left(1-3\sqrt{10}\delta_\gamma+\frac{25}{24}\delta_\gamma^2\right)\left(1+\frac{17}{20}\delta_p^2\right)}{\left(1+\delta_\gamma^2\right)\left(1+\delta_p^2\right)}$
		$a_4 = \frac{9}{77}\frac{\delta_\gamma^2\left(1+\frac{1}{2}\delta_p^2\right)}{\left(1+\delta_\gamma^2\right)\left(1+\delta_p^2\right)}$

Table A.9: Initial State $J^{\pi} = 5^{+}$

$5^{+} \rightarrow 3^{+}$	$a_2 = \frac{104}{231}$
	$a_4 = -\frac{18}{77}$

Appendix B

Measured Angular Distribution Coefficients

Table B.1: Measured Angular Distribution Coefficients for Primary and Secondary γ-Rays.

	Primary Transition			Secondary Transition		
E_i (keV)	E_f (keV)	a_2	a_4	E_f (keV)	a_2	a_4
6520.8	0.0	-0.55 ± 0.10	0.19 ± 0.16			
	1454.67	0.61 ± 0.11	0.20 ± 0.15			
	2539.03	-0.64 ± 0.07	0.16 ± 0.11			
	2723.96	-0.01 ± 0.18	-0.27 ± 0.27			
	2839.9	-0.21 ± 0.06	0.09 ± 0.09	709.02	0.19 ± 0.09	0.34 ± 0.12
				1454.67	0.01 ± 0.09	0.00 ± 0.13
	2937.87	0.34 ± 0.08	0.15 ± 0.10			
	3835.9	-0.06 ± 0.21	0.07 ± 0.28			
	4182.65	0.34 ± 0.07	-0.07 ± 0.10	709.02	-0.55 ± 0.07	-0.02 ± 0.11
	4502.32	-0.39 ± 0.04	0.07 ± 0.06	0.0	0.20 ± 0.10	0.06 ± 0.15
				1454.67	-0.08 ± 0.07	0.12 ± 0.09
6597.7	1973.62	0.42 ± 0.06	-0.09 ± 0.08			
	2839.9	0.19 ± 0.17	-0.04 ± 0.24	709.02	0.69 ± 0.26	0.04 ± 0.33
	3928.9	0.24 ± 0.22	0.48 ± 0.28			
6667.8	2723.96	0.07 ± 0.18	0.65 ± 0.20			

Table B.1*(continued)*

	Primary Transition			Secondary Transition		
E_i (keV)	E_f (keV)	a_2	a_4	E_f (keV)	a_2	a_4
	2937.87	−0.28±0.03	0.07±0.05			
	3835.9	0.90±0.22	0.48±0.48			
	4143.67	−0.51±0.09	0.10±0.12	0.0	−0.23±0.17	0.07±0.20
	4182.65	−0.35±0.05	0.07±0.06	0.0	−0.48±0.23	−0.08±0.29
				709.02	−0.32±0.07	0.12±0.09
6853.9	0.0	−0.07±0.07	−0.05±0.10			
	677.29	−0.09±0.01	−0.04±0.02			
	2723.96	−0.15±0.06	−0.06±0.10	0.0	0.03±0.05	−0.12±0.08
	2937.87	−0.01±0.02	−0.04±0.03			
	4468.33	−0.07±0.03	−0.12±0.04	0.0	0.12±0.09	0.05±0.13
	4502.32	0.01±0.05	−0.11±0.07	0.0	0.00±0.16	0.05±0.23
				1454.67	0.14±0.09	0.04±0.13
6873.4	2723.96	−0.33±0.04	−0.15±0.06			
	2839.9	0.33±0.09	−0.10±0.13	1454.67	−0.02±0.11	−0.02±0.16
	2937.87	−0.43±0.02	−0.09±0.04			
	5508.55	0.38±0.08	−0.15±0.12	1454.67	−0.17±0.22	0.35±0.30
6978.3	5508.55	−0.25±0.11	0.25±0.17	1454.67	0.17±0.30	0.21±0.42
				1973.62	−0.03±0.28	0.14±0.39
7045.0	2539.03	−0.48±0.09	−0.14±0.12			
	4143.67	0.52±0.11	−0.26±0.15			
	6093.5	−0.47±0.07	−0.04±0.11			
7179	3019.39	0.12±0.17	0.00±0.22	677.29	0.12±0.09	−0.13±0.12
	709.02	0.13±0.14	0.03±0.20			
7203.0	2937.87	0.21±0.03	−0.03±0.05	0.0	−0.31±0.09	0.02±0.11
				677.29	0.24±0.04	−0.57±0.06
				709.02	−0.15±0.17	−0.05±0.24
				1454.67	0.06±0.03	−0.11±0.04
	5508.55	−0.20±0.11	−0.07±0.16			
7207.5	709.02	−0.16±0.16	0.37±0.24	0.0	0.09±0.04	0.04±0.06
	3019.39	−0.04±0.02	0.03±0.04	677.29	−0.04±0.02	0.00±0.03
	4937.9	0.18±0.12	0.14±0.17	677.29	−0.02±0.21	−0.22±0.32
	5506.1	−0.04±0.03	0.06±0.05	677.29	−0.06±0.06	0.08±0.10

Table B.1*(continued)*

	Primary Transition			Secondary Transition		
E_i (keV)	E_f (keV)	a_2	a_4	E_f (keV)	a_2	a_4
7223.3	0.0	−0.39±0.03	−0.05±0.04			
	709.02	−0.44±0.03	0.08±0.06			
	1454.67	0.23±0.06	−0.04±0.08			
	3019.39	−0.42±0.04	0.06±0.07			
	4143.67	0.32±0.02	0.01±0.03			
	4626.55	−0.11±0.03	0.02±0.04			
7282.0	1454.67	−0.38±0.03	0.13±0.04			
	2539.03	0.20±0.08	0.00±0.10			
	2723.96	−0.36±0.07	0.21±0.09			
	2839.9	0.43±0.10	−0.01±0.13	709.02	0.24±0.10	0.40±0.12
	4182.65	−0.42±0.03	0.10±0.04	709.02	−0.44±0.04	0.13±0.05
	5576.90	0.04±0.16	0.21±0.21			
7283.4	0.0	−0.21±0.02	0.06±0.02			
	677.29	0.37±0.07	0.68±0.09			
	709.02	−0.30±0.08	0.00±0.13			
	1454.67	0.27±0.05	0.13±0.07			
	2723.96	0.30±0.02	0.04±0.03			
	2937.87	−0.14±0.12	0.15±0.17			
	3835.9	0.22±0.04	−0.04±0.05	2937.87	0.09±0.03	0.04±0.04
				709.02	−0.21±0.09	0.27±0.14
	3928.9	0.00±0.14	0.12±0.20			
	4422.4	0.25±0.01	0.03±0.01	709.02	−0.10±0.07	0.36±0.10
				0.0	0.04±0.01	0.34±0.02
	4736.4	−0.14±0.03	−0.02±0.04	2937.87	0.71±0.16	−0.10±0.22
	4941.0	−0.33±0.01	0.01±0.02			
	5206.6	−0.13±0.03	0.09±0.04	709.02	0.06±0.12	0.10±0.17
				0.0	0.32±0.07	0.23±0.09
7322	0.0	−0.09±0.10	−0.06±0.14			
	2937.87	0.37±0.14	−0.40±0.20	1454.67	−0.31±0.11	0.15±0.18
	4502.32	0.16±0.12	−0.04±0.17	1454.67	−0.07±0.17	−0.03±0.25
7383.4	2937.87	−0.32±0.02	0.08±0.04			
	5508.55	0.38±0.13	0.11±0.19			

Table B.1*(continued)*

	Primary Transition			Secondary Transition		
E_i (keV)	E_f (keV)	a_2	a_4	E_f (keV)	a_2	a_4
7493	2937.87	−0.18±0.08	0.09±0.11	677.29	−0.16±0.11	−0.02±0.17
				1454.67	−0.16±0.07	−0.02±0.10
	4182.65	−0.06±0.10	0.24±0.14	709.02	−0.03±0.12	0.02±0.17
	4502.32	−0.14±0.20	0.40±0.30			
7560.5	2937.87	−0.22±0.07	0.02±0.12			
	3733.9	0.53±0.10	−0.59±0.15			
	4182.65	−0.50±0.03	−0.07±0.05			
	5508.55	0.26±0.05	−0.15±0.08			
	5576.90	−0.43±0.02	−0.16±0.04	709.02	−0.42±0.07	−0.03±0.12
	5934.0	−0.17±0.03	−0.07±0.05	1973.62	−0.43±0.17	0.26±0.26
	6006.04	0.35±0.04	−0.18±0.07			
7562.5	0.0	0.44±0.14	0.17±0.19			
	1454.67	0.35±0.04	0.06±0.06			
	2539.03	−0.01±0.10	0.03±0.14			
	2937.87	−0.08±0.12	0.29±0.16			
	3019.39	−0.34±0.13	0.19±0.19			
	3835.9	0.21±0.03	0.05±0.04	709.02	0.01±0.08	0.26±0.11
				2937.87	0.04±0.02	−0.02±0.03
	3928.9	−0.09±0.14	0.34±0.19			
	4422.4	0.44±0.14	01.17±0.19			
	4736.4	−0.10±0.03	0.00±0.04	2937.87	−0.19±0.03	−0.03±0.05
	4937.9	−0.28±0.03	0.06±0.05	677.29	−0.29±0.06	0.18±0.09
	5206.6	−0.18±0.04	0.09±0.06	0.0	0.04±0.18	0.28±0.25
	5506.1	−0.26±0.01	0.05±0.02	677.29	−0.27±0.02	0.02±0.03
	5701.7	−0.10±0.02	0.02±0.02	2937.87	−0.21±0.02	0.06±0.04
				4182.65	−0.28±0.06	0.14±0.09
7605.0	0.0	0.50±0.05	0.32±0.08			
	2937.87	0.34±0.01	−0.07±0.01			
	4182.65	0.39±0.04	−0.19±0.06			
	5508.55	−0.14±0.04	−0.11±0.07	1454.67	−0.29±0.18	0.26±0.29
				1973.62	0.31±0.15	0.22±0.21
7636.0	0.0	−0.10±0.15	−0.14±0.23			

Table B.1*(continued)*

	Primary Transition			Secondary Transition		
E_i (keV)	E_f (keV)	a_2	a_4	E_f (keV)	a_2	a_4
	3835.9	−0.39±0.05	0.06±0.08	2937.87	0.29±0.04	0.11±0.06
	4182.65	−0.56±0.08	0.17±0.14			
	4232.2	−0.03±0.12	−0.12±0.18			
	4298.1	0.00±0.21	−0.26±0.31			
	4422.4	−0.22±0.08	0.18±0.12			
	4736.4	0.25±0.05	0.11±0.07	2937.87	−0.32±0.05	0.01±0.07
7644.3	2723.96	−0.30±0.04	0.07±0.06			
	2839.9	0.28±0.06	0.17±0.09	1454.67	−0.27±0.06	0.02±0.09
	2937.87	−0.57±0.04	0.18±0.06			
	3835.9	−0.42±0.03	0.11±0.04	709.02	−0.16±0.08	0.26±0.11
				1454.67	−0.02±0.16	0.26±0.23
	4182.65	−0.15±0.05	0.27±0.07			
	4298.1	−0.30±0.19	0.48±0.26			
	4422.4	−0.46±0.04	0.16±0.06			
7688.2	5231.6	0.34±0.16	−0.14±0.20			
7749.3	2723.96	−0.31±0.19	−0.07±0.28			
	2937.87	−0.02±0.02	−0.03±0.04	0.0	0.06±0.04	−0.05±0.06
				677.29	0.02±0.03	0.01±0.04
				1454.67	0.02±0.02	−0.03±0.03
	3019.39	0.31±0.12	−0.33±0.18			
	4468.33	−0.03±0.10	0.00±0.15			
	4502.32	0.08±0.09	0.19±0.13			
7752.7	1973.62	0.28±0.07	0.09±0.11			
	5508.55	−0.43±0.07	−0.04±0.10	1454.67	−0.56±0.15	0.34±0.23
				1973.62	0.10±0.13	0.16±0.19
	5934.0	0.46±0.03	−0.02±0.05	1973.62	−0.43±0.06	0.06±0.10
				2839.9	0.09±0.11	−0.15±0.16
				2937.87	0.51±0.12	−0.14±0.17
7759.0	1454.67	−0.33±0.03	0.02±0.05			
	1973.62	0.18±0.06	0.16±0.08			
	2539.03	0.08±0.19	0.23±0.28			
	2723.96	−0.34±0.02	0.10±0.04	0.0	0.51±0.03	0.16±0.04

Table B.1*(continued)*

	Primary Transition			Secondary Transition		
E_i (keV)	E_f (keV)	a_2	a_4	E_f (keV)	a_2	a_4
	2839.9	0.45±0.07	0.02±0.10			
	3928.9	0.20±0.16	0.00±0.23			
	4422.4	−0.45±0.15	−0.18±0.25			
7786.4	3928.9	−0.14±0.19	−0.24±0.28			
	2539.03	−0.25±0.09	−0.18±0.13	0.0	0.33±0.05	−0.11±0.08
	1973.62	−0.23±0.12	0.09±0.18			
7883.8	4343.6	−0.24±0.03	−0.05±0.05	1973.62	0.37±0.04	−0.15±0.05
	4298.1	0.59±0.16	−0.19±0.21			
	2839.9	0.15±0.05	0.08±0.07	1454.67	0.21±0.04	0.46±0.06
	2539.03	−0.34±0.07	0.05±0.12			
7920.9	709.02	−0.40±0.08	0.06±0.12			
	1973.62	−0.60±0.09	−0.13±0.14			
	2539.03	−0.08±0.06	−0.01±0.09	0.0	0.22±0.04	0.18±0.06
	2937.87	−0.04±0.08	0.04±0.12			
	3835.9	0.06±0.13	−0.08±0.19			
	3928.9	−0.12±0.12	0.02±0.18			
	4626.55	0.06±0.11	0.10±0.17			
	4736.4	−0.09±0.09	0.08±0.13	2937.87	−0.02±0.12	0.31±0.17
	5206.6	−0.19±0.15	−0.10±0.22			
7922	2839.9	−0.49±0.08	−0.18±0.13	709.02	0.49±0.06	−0.08±0.09
7996.7	0.0	0.00±0.05	0.01±0.07			
	3019.39	0.11±0.07	0.01±0.10			
	3733.9	−0.18±0.07	−0.23±0.15			
	4937.9	−0.05±0.09	0.13±0.13			
8007.4	0.0	0.29±0.08	−0.24±0.12			
	2937.87	−0.27±0.04	0.01±0.06			
	3928.9	−0.42±0.13	−0.05±0.20			
	4182.65	−0.36±0.06	0.01±0.09			
	5576.90	−0.56±0.13	0.08±0.20			
	5934.0	−0.32±0.07	−0.23±0.11			
8014.3	0.0	0.16±0.12	0.11±0.18			
	709.02	−0.89±0.09	0.45±0.15			

Table B.1*(continued)*

	Primary Transition			Secondary Transition		
E_i (keV)	E_f (keV)	a_2	a_4	E_f (keV)	a_2	a_4
	4182.65	0.46±0.06	0.00±0.09			
	5508.55	−0.17±0.04	−0.12±0.07	1454.67	−0.34±0.09	−0.06±0.14
				1973.62	0.32±0.08	0.00±0.12

Appendix C

Measured Mixing Ratios

Table C.1: Measured Mixing Ratios for Primary γ-rays.

E_i (keV)	E_f (keV)	δ_γ
6520.8	0.0	0.046 ± 0.058
	1454.67	$-0.075^{+0.090}_{-0.091}$
	2539.03	$-5.2^{+1.4}_{-3.0}$
	2839.9	$8.5^{+5.2}_{-2.4}$
	2937.87	0.103 ± 0.054
	3835.9	$0.37^{+0.17}_{-0.16}$
	4182.65	0.081 ± 0.051
	4502.32	-0.033 ± 0.022
6667.8	2723.96	$33^{+\infty}_{-24}$
	2937.87	-0.035 ± 0.017
	3835.9	$-1.71^{+0.65}_{-1.48}$
	4182.65	-0.001 ± 0.023
	5576.90	0.010 ± 0.095
6853.9	2724.0	$-1.81^{+0.88}_{-3.40}$
	4502.32	0.04 ± 0.21
6873.4	2723.96	-0.006 ± 0.025
	2937.87	0.050 ± 0.021
	5508.55	$-1.41^{+0.27}_{-0.36}$
7045.0	6093.5	0.074 ± 0.036
7203.0	2937.87	0.061 ± 0.035
7223.3	4143.67	-0.003 ± 0.023

Table C.1*(continued)*

E_i (keV)	E_f (keV)	δ_γ
	4626.55	0.060 ± 0.18
7282.0	2539.03	$0.229^{+0.081}_{-0.078}$
	2723.96	$3.76^{+0.72}_{-0.52}$
	2839.9	$-1.40^{+0.29}_{-0.40}$
	4182.65	0.066 ± 0.018
7283.4	5206.6	-0.058 ± 0.031
	4941.0	0.038 ± 0.010
	4736.4	-0.058 ± 0.028
	4422.4	0.052 ± 0.011
	3835.9	0.074 ± 0.041
	2723.96	-0.008 ± 0.022
	1454.67	$-2.34^{+0.32}_{-0.42}$
	709.02	-0.011 ± 0.066
	0.0	-0.057 ± 0.012
7493	2937.87	$-12^{+10}_{-\infty}$
7560.5	2937.87	-0.062 ± 0.038
	4182.65	0.084 ± 0.018
	5508.55	$-1.97^{+0.24}_{-0.30}$
	5576.90	0.038 ± 0.014
	5934.0	$0.675^{+0.047}_{-0.045}$
	6006.04	$-1.58^{+0.16}_{-0.18}$
7562.5	0.0	-0.049 ± 0.021
	1454.67	-0.089 ± 0.063
	2937.87	$-360^{+350}_{-\infty}$
	3019.39	0.07 ± 0.11
	3835.9	0.091 ± 0.036
	3928.9	-0.06 ± 0.16
	4422.4	$-1.33^{+0.48}_{-0.89}$
	4736.4	-0.026 ± 0.030
	5206.6	$-0.122^{+0.049}_{-0.050}$
	5701.7	-0.13 ± 0.12
7605.0	0.0	$-7.5^{+1.6}_{-2.8}$
	2937.87	-2.45 ± 0.06

Table C.1*(continued)*

E_i (keV)	E_f (keV)	δ_γ
	4182.65	$-2.13^{+0.20}_{-0.24}$
	5508.55	-0.017 ± 0.036
7636.0	3835.9	0.044 ± 0.029
	4182.65	$2.42^{+0.43}_{-0.33}$
	4422.4	$5.17^{+1.58}_{-0.99}$
	4736.4	$0.170^{+0.051}_{-0.050}$
7644.2	2723.96	-0.001 ± 0.022
	2839.9	0.170 ± 0.065
	2937.87	$2.37^{+0.17}_{-0.15}$
	3835.9	0.069 ± 0.016
	4182.65	$6.6^{+1.5}_{-1.0}$
	4422.4	$2.97^{+0.26}_{-0.23}$
7749.3	2723.96	$-1.3^{+1.2}_{-\infty}$
	2937.87	0.01 ± 17
	3019.39	$-1.00^{+0.54}_{-1.17}$
7752.7	1973.62	$0.173^{+0.077}_{-0.075}$
	5508.55	$1.17^{+0.37}_{-0.27}$
	5934.0	-0.049 ± 0.071
7759.0	1454.67	0.000 ± 0.019
	1973.62	$0.256^{+0.061}_{-0.059}$
	2539.03	$0.36^{+0.23}_{-0.20}$
	2723.96	0.012 ± 0.014
	2839.9	-0.042 ± 0.088
	3928.9	$0.23^{+0.17}_{-0.16}$
	4422.4	$0.074^{+0.085}_{-0.084}$
7883.8	2539.03	0.006 ± 0.037
	2839.9	-0.243 ± 0.025
	4298.1	$-0.67^{+0.35}_{-0.51}$
	4343.6	-0.044 ± 0.022
7920.9	709.02	$0.133^{+0.082}_{-0.080}$
	1973.62	$-1.25^{+0.57}_{-1.27}$
	2539.03	0.000 ± 0.078
	2937.87	$0.39^{+0.12}_{-0.11}$

Table C.1*(continued)*

E_i (keV)	E_f (keV)	δ_γ
	3835.9	$0.23^{+0.16}_{-0.15}$
	4736.4	$7.6^{+59.5}_{-3.6}$
7922	2839.9	0.106 ± 0.046
7996.7	3733.9	$1.00^{+1.54}_{-0.61}$
8007.4	0.0	$-22^{+12}_{-\infty}$
	2937.87	$0.729^{+0.084}_{-0.078}$
	4182.65	$0.97^{+0.32}_{-0.24}$
	5576.9	$1.57^{+1.14}_{-0.56}$
8014.3	0.0	$-0.296^{+0.060}_{-0.062}$
	709.02	$1.35^{+0.24}_{-0.19}$
	4182.65	-0.020 ± 0.049
	5508.55	-0.014 ± 0.031

Table C.2: Measured Mixing Ratios for Secondary γ-rays.

E_i (keV)	J^π	E_f (keV)	J^π	δ_γ
709.02	1^+	0.0	1^+	$-1.00^{+0.77}_{-3.40}$
2723.96	2^+	0.0	1^+	$-4.81^{+0.39}_{-0.46}$
2839.9	3^+	1454.67	2^+	-12^{+3}_{-6}
2937.87	2^+	0.0	1^+	$0.32^{+0.20}_{-0.18}$
		709.02	1^+	0.02 ± 0.27
		1454.67	2^+	$-4.14^{+0.94}_{-1.66}$
3835.9	2^+	709.02	1^+	$3.61^{+0.77}_{-0.55}$
		2937.87	2^+	$0.12 \pm +0.03$
4182.65	2^+	0.0	1^+	0.06 ± 0.14
4422.4	2^+	709.02	1^+	$3.28^{+1.90}_{-0.92}$
		0.0	1^+	$10.2^{+2.2}_{-1.6}$
4502.32	1^+	0.0	1^+	$0.0^{+5.2}_{-3.7}$
		1454.67	2^+	$0.34^{+0.17}_{-0.15}$
4736.4	3^+	2937.87	2^+	$-0.02 \pm +0.03$
5508.6	3^+	1454.67	2^+	0.06 ± 0.05
5576.90	2^+	709.02	1^+	0.051 ± 0.049
5701.7	1^+	4182.65	2^+	$-1.34^{+0.82}_{-3.72}$
5934.0	3^+	1973.62	3^+	$1.98^{+0.89}_{-0.52}$

Appendix D

Comparison with Shell Model and Analog States

Table D.1: Comparison of Experimental Results with Shell Model Calculations and Analog States. The ^{30}Si energies have been increased by 677.29 keV to align the ground state of ^{30}Si with the first excited state of ^{30}P.

Experimental			Shell-Model			^{30}Si		
E_x (keV)	J^π	T	E_x (keV)	J^π	T	E_x (keV)	J^π	T
0.0	1^+	0	0	1^+	0	-		
677.29	0^+	1	693	0^+	1	677	0^+	1
709.02	1^+	0	644	1^+	0	-		
1454.67	2^+	0	1491	2^+	0	-		
1973.62	3^+	0	2061	3^+	0	-		
2539.03	3^+	0	2510	3^+	0	-		
2723.96	2^+	0	2461	2^+	0	-		
2839.9	3^+	0	2973	3^+	0	-		
2937.87	2^+	1	3003	2^+	1	2917	2^+	1
3019.39	1^+	0	3131	1^+	0	-		
3733.9	1^+	0	3737	1^+	0	-		
3835.9	2^+	0	4113	2^+	0	-		
3928.9	3^+	0	4285	3^+	0	-		
4143.67	2^-	0	-			-		
4182.65	2^+	1	4243	2^+	1	4177	2^+	1
4232.2	4^-	0	-			-		
4298.1	4^+	0	4593	4^+	0	-		

Table D.1*(continued)*

Experimental			Shell-Model			^{30}Si		
E_x (keV)	J^π	T	E_x (keV)	J^π	T	E_x (keV)	J^π	T
4343.6	5^+	0	4584	5^+	0	-		
4422.4	2^+	0	4358	2^+	0	-		
4468.33	0^+	1	4778	0^+	1	4467	0^+	1
4502.32	1^+	1	4903	1^+	1	4447	1^+	1
4626.55	3^-	0	-			-		
4736.4	3^+	0	4862	3^+	0	-		
4926.4	3^-	0	-			-		
4937.9	1^-	0	-			-		
4941.0	1^+	0	4931	1^+	0	-		
5028	$5^-, 5^+ (4^-, 6^-)$		-			-		
5206.6	3^+		5654	3^+	1	5507	3^+	1
5231.6	$2^-, 4^-$		-			-		
			5146	4^+	0	-		
5411.13	2^-		5471	2^+	0	-		
5506.1	1^-	0	-			-		
5508.55	3^+	0	5574	3^+	0	-		
5576.90	2^+	1	5741	2^+	1	5487	2^+	1
5595	4^+		5455	4^+	0	-		
5701.7	1^+	0	5896	1^+	0	-		
5714	$5^+, 7^+$		5104	5^+	0	-		
5808	$3^+, 5^+$		5571	5^+	0	-		
5890	$1^+, 2^+, 3^+$	(1)	5888	3^+	1	5907	3^+	1
5907.7	2^-		-			-		
5933.96	3^+	0	6166	3^+	0	-		
5993	$0^-, 1^-, 2^-$		-			-		
5997.1	1^+	0	6085	1^+	0	-		
6006.04	3^+	0	6310	3^+	0	-		
6050	$0^+, 1^+$	(1)	6218	0^+	1	6047	0^+	1
6051	$3^+, 4^+, 5^+$		6199	4^+	1	5957	4^+	1
			6221	4^+	0	-		
6094.6	3^-	1	-			6167	3^-	1
6181	$5^+, 6^+, 7^+$							
6228.95	$3^+, 5^+$		6377	5^+	0	-		

Table D.1*(continued)*

Experimental			Shell-Model			^{30}Si		
E_x (keV)	J^π	T	E_x (keV)	J^π	T	E_x (keV)	J^π	T
			6289	0^+	0	-		
6269.6	2^-	1		-				
6295	> 5							
6299.3	3^+	0				-		
6361	$4^-, 5^-, 6^-$			-				
6468	$5^+, 6^-$							
6481.4	1^+	0				-		
6520.8	2^+	0	6652	2^+	0	-		
6597.7	$3^-, 3^+, 4^+, 5^+$		6607	4^+	1	6627	4^+	1
			6643	4^+	0	-		
6607	$3^+, 5^+$		6574	5^+	0	-		
6656		(1)	6898	2^+	1	6287	2^+	1
6667.8	3^+		7066	3^+	0			
6791	> 5							
6853.9	1^+	0	7085	1^+	0	-		
6873.4	3^+	1						
6877	2^-			-				
6921	1^-	0		-				
6978.3	$3^+, 4^+$	0	7012	4^+	0	-		
6981	$5^+, 6^+, 7^+$		6945	5^+	0	-		
7014.9	2^-	0		-		-		
7045.0	4^-	0		-		-		
7049.4	4^-	1		-		7177	4^-	1
7119.1	$2^-, 2^+, 3^-, 3^+$		7068	2^+	0	-		
7179	1^-	1		-				
7199.1	$5^+, 6^+, 7^+$		7120	6^+	0			
7203.0	2^+							
7207.5	$0^+, 1^+$	1	7457	0^+	1	7319	0^+	1
			7145	0^+	0			
7223.3	2^-	1		-		7318	2^-	1
7282.0	3^+	0	7263	3^+	0	-		
7283.4	2^+	1	7213	2^+	1	7217	2^+	1
7304.9	2^-	0		-		-		

Table D.1*(continued)*

Experimental			Shell-Model			^{30}Si		
E_x (keV)	J^π	T	E_x (keV)	J^π	T	E_x (keV)	J^π	T
7306.3	2^-	0		-			-	
7322	1^-			-		7417	1^-	1
7347	$5^+, 6^+, 7^+$					7677	5^+	1
7370	?							
7383.4	$2^+, 3^-$	1						
7493	1^+	1						
7560.5	3^+	0	7444	3^+	0		-	
7562.5	2^+	1						
7579.9	2^-	0		-			-	
7605.0	2^+	1	7660	2^+	1	7597	2^+	1
7636.0	3^+							
7644.3	3^+	0					-	
7647	$4^-, 5^-, 6^-$	(1)		-		7717	5^-	1
7688.2	4^-	0		-			-	
7742	1^-			-				
7749.3	1^+	0	7732	1^+	0		-	
7752.7	3^+					7547	3^+	1
7759.0	3^+	1	7895	3^+	1	7757	3^+	1
7786.4	$2^-(4^-)$			-				
7803	$2^-, 3^-, 4^-$			-				
7826.3	2^-	0		-			-	
7873.7	4^-			-				
			7877	6^+	0			
7883.8	4^+		7691	4^+	1	7897	4^+	1
7892	2^-	1, (0)		-		8187	2^-	1
7920.9	2^+	0	7701	2^+	0		-	
7921.8	3^+	0	8027	3^+	0		-	
7922	$4^+(4^-)$		7765	4^+	0			
7932	0^+					8117	0^+	1
7996.7	1^+	1						
			7972	1^+	0			
			8009	1^+	0			
8001	1^-			-				

Table D.1*(continued)*

Experimental			Shell-Model			^{30}Si		
E_x (keV)	J^π	T	E_x (keV)	J^π	T	E_x (keV)	J^π	T
8007.4	2^+	1	8000	2^+	1	7937	2^+	1
8014.3	2^+	0	8083	2+	0	-		

Bibliography

[Alh92] Y. Alhassid and A. Novoselsky, "Chaos in the Low-Lying Collective States of Even-Even Nuclei: Quantal Fluctuations", Physical Review C **45**, 1677 (1992).

[Bie60] L. C. Biedenharn, "Angular Correlations in Nuclear Spectroscopy", in *Nuclear Spectroscopy, Part B*, edited by F. Ajzenberg-Selove, pages 732–810, Academic Press, New York, 1960.

[Bla52] J. M. Blatt and L. C. Biedenharn, "The Angular Distribution of Scattering and Reaction Cross Sections", Reviews of Modern Physics **24**, 258 (1952).

[Boh84] O. Bohigas, M. J. Giannoni, and C. Schmit, "Characterization of Chaotic Quantum Spectra and Universality of Level Fluctuation Laws", Physical Review Letters **52**, 1 (1984).

[Boh88] O. Bohigas and H. A. Weidenmüller, "Aspects of Chaos in Nuclear Physics", Annual Review of Nuclear and Particle Science **38**, 421 (1988).

[Bro81] T. A. Brody *et al.*, "Random-Matrix Fluctuations: Spectrum and Strength Fluctuations", Reviews of Modern Physics **53**, 385 (1981).

[Byb95] C. R. Bybee, *Fourier Transform as Signature of Chaos in Nuclei and Data Acquisition for Compton-Suppressed Spectrometer*, Ph.D. thesis, North Carolina State University, 1995.

[Dra94] J. M. Drake, *Resonance Tests of Detailed Balance and Design of Compton Suppression Spectrometer*, Ph.D. thesis, North Carolina State University, 1994.

[Dys62] F. J. Dyson, "A Brownian-Motion Model for the Eigenvalues of a Random Matrix", Journal of Mathematical Physics **3**, 1191 (1962).

[Dys63] F. J. Dyson and M. L. Mehta, "Statistical Theory of the Energy Levels of Complex Systems. IV", Journal of Mathematical Physics **4**, 701 (1963).

[End86] P. M. Endt, P. de Wit, and C. Alderliesten, "The ^{25}Mg(p, γ)^{26}Al and ^{25}Mg(p, p$'$) Resonances for $E_p = 0.31 - 1.84$ MeV", Nuclear Physics **A459**, 61 (1986).

[End88] P. M. Endt, P. de Wit, and C. Alderliesten, "The ^{25}Mg(p, γ)^{26}Al Reaction; Branchings, Energies, and Lifetimes", Nuclear Physics **A476**, 333 (1988).

[End90] P. M. Endt, "Energy Levels of $A = 21 - 44$ Nuclei (VII)", Nuclear Physics **A521**, 1 (1990).

[End93] P. M. Endt, "Strengths of Gamma-Ray Transitions in $A = 5 - 44$ Nuclei, IV", Atomic Data and Nuclear Data Tables **55**, 171 (1993).

[Fan53] U. Fano, "Geometrical Characterization of Nuclear States and the Theory of Angular Correlations", Physical Review **90**, 577 (1953).

[Fer65] A. J. Ferguson, *Angular Correlation Methods in Gamma-Ray Spectroscopy*, North-Holland, Amsterdam, 1965.

[Fir96] R. B. Firestone, *Table of Isotopes*, John Wiley & Sons, New York, eighth edition, 1996.

[Fra91] S. C. Frankle, *Nuclear Resonance Spectroscopy in* ^{30}P, Ph.D. thesis, North Carolina State University, 1991.

[Gol60] L. J. B. Goldfarb and R. C. Johnson, "Angular Distributions and Polarization in Stripping Processes and in Direct Reactions", Nuclear Physics **18**, 353 (1960).

[Guh98] T. Guhr, A. Müller-Groeling, and H. A. Weidenmüller, "Random Matrix Theories in Quantum Physics: Common Concepts", Physics Reports **299**, 190 (1998).

[Haq82] R. U. Haq, A. Pandey, and O. Bohigas, "Fluctuation Properties of Nuclear Energy Levels: Do Theory and Experiment Agree?", Physical Review Letters **48**, 1086 (1982).

[Hub54] R. Huby, "Phase of Matrix Elements in Nuclear Reactions and Radioactive Decay", Proceedings of the Physical Society **67A**, 1103 (1954).

[LaB95] M. A. LaBonte, "Angular Distribution Study of the ^{29}Si(p,γ) Reaction", M.S. thesis, North Carolina State University, 1995.

[Lom94] M. Lombardi, O. Bohigas, and T. H. Seligman, "New evidence of GOE statistics for compound nuclear resonances", Physics Letters B **324**, 263 (1994).

[Meh91] M. L. Mehta, *Random Matrices*, Academic Press, New York, second edition, 1991.

[Mer93] D. C. Meredith, "Statistics and Scarring of Eigenvectors of a Shell Model", Physical Review E **47**, 2405 (1993).

[Nel83] R. O. Nelson, *Proton Resonance Spectroscopy in* ^{28}Si *and* ^{30}P, Ph.D. thesis, Duke University, 1983.

[Nel85] W. R. Nelson, H. Hirayama, and D. W. O. Rogers, "The EGS4 Code System", SLAC265 (1985).

[Orm99] W. E. Ormand, 1999, private communication.

[Pan81] A. Pandey, "Statistical Properties of Many-Particle Spectra. IV. New Ensembles by Stieltjes Transform Methods", Annals of Physics **134**, 110 (1981).

[Por56] C. E. Porter and R. G. Thomas, "Fluctuations of Nuclear Reaction Widths", Physical Review **104**, 483 (1956).

[Rei85] J. P. L. Reinecke *et al.*, "The Energy Levels of ^{30}P", Nuclear Physics **A435**, 333 (1985).

[Ros67] H. J. Rose and D. M. Brink, "Angular Distributions of Gamma Rays in Terms of Phase-Defined Matrix Elements", Review of Modern Physics **39**, 306 (1967).

[Sel85] T. H. Seligman, J. J. M. Verbaarschot, and M. R. Zirnbauer, "Fluctuations of Quantum Spectra and Their Semiclassical Limit in the Transition between Order and Chaos", J. Phys. A **18**, 2227 (1985).

[Shr83] J. F. Shriner, Jr., *Nuclear Resonance Spectroscopy in ^{45}Sc and ^{40}Ca*, Ph.D. thesis, Duke University, 1983.

[Shr90] J. F. Shriner, Jr., E. G. Bilpuch, P. M. Endt, and G. E. Mitchell, "Fluctuation Properties of States in ^{26}Al", Zeitschrift für Physik A **335**, 393 (1990).

[Shr91] J. F. Shriner, Jr., G. E. Mitchell, and T. von Egidy, "Fluctuation Properties of Spacings of Low-Lying Nuclear Levels", Zeitschrift für Physik A **338**, 309 (1991).

[Vav96] G. A. Vavrina, *Resonance Spectroscopy of the $^{29}Si(p,\gamma)$ Reaction*, Ph.D. thesis, North Carolina State University, 1996.

[Wal96] P. M. Wallace, *A High-Resolution Study of the $^{29}Si(p,\gamma)$ Reaction*, Ph.D. thesis, Duke University, 1996.

[Wei51] V. F. Weisskopf, "Transition Probabilities in Nuclei", Physical Review **83**, 1073 (1951).

[Wes88] C. R. Westerfeldt, R. O. Nelson, E. G. Bilpuch, and G. E. Mitchell, "A Microcomputer-Based System for Measuring Excitation Functions with Good Energy Resolution", Nuclear Instruments and Methods in Physics Research **A270**, 467 (1988).

[Wes95] C. R. Westerfeldt, J. F. Shriner, Jr., and G. A. Vavrina, *The TUNL High Resolution Laboratory System and Operating Procedures*, Triangle Universities Nuclear Laboratory, Durham, NC, third edition, 1995.